

THE DE HAAS-VAN ALPHEN EFFECT

IN GALLIUM

THE DE HAAS-VAN ALPHEN EFFECT
IN GALLIUM

By
FORREST WAKEFIELD HOLROYD, M.S.

A Thesis
Submitted to the School of Graduate Studies
in Partial Fulfilment of the Requirements
for the Degree
Doctor of Philosophy

McMaster University

April, 1976

DOCTOR OF PHILOSOPHY (1976)

McMASTER UNIVERSITY

(Physics)

Hamilton, Ontario.

TITLE: The de Haas-van Alphen Effect in Gallium

AUTHOR: Forrest Wakefield Holroyd,

A.B. (University of Rochester)

B.S. (University of Rochester)

M.S. (University of Illinois)

SUPERVISOR: Dr. W. R. Datars

NUMBER OF PAGES: x, 166

SCOPE AND CONTENTS:

The Fermi surface of gallium is studied using the de Haas-van Alphen effect. A theoretical treatment of the de Haas-van Alphen effect is reviewed. Several models for the Fermi surface of gallium are presented, and the best reviewed in detail. This model is compared to the data experimentally observed. New interpretations of previous data are presented in the light of the additional information presented here. Several Fermi surface pieces not previously observed, or not previously identified, are confirmed. Reasonable agreement between experiment and theory is obtained.

ABSTRACT

The de Haas-van Alphen effect in gallium single crystals has been studied using the low frequency field-modulation technique with the magnetic field up to 56kG parallel to the three principle crystallographic planes. Frequencies due to small sixth-band hole and seventh-band electron surfaces previously observed by Goldstein and Foner over part of their expected range of magnetic field direction have been extended to show closed pieces of Fermi surface. Many new frequencies have also been observed, and most have been identified using Reed's pseudopotential model of the gallium Fermi surface. The large previously unseen eighth-band electron surface has been observed in its entirety, and a small seventh-band electron surface previously observed in part of one plane but not identified correctly has now been unequivocally identified. Frequencies due to the small fifth-band hole surface and many frequencies attributed to the large complex comprising seventh- and eighth-band electron surfaces have been observed. Strong indications of magnetic breakdown for many of the latter are also exhibited. The large multiply-connected sixth-band hole surface is expected to have comparatively few extremal orbits according to Reed's model, but most of these were observed. In addition, several new frequencies are attributed

to this surface, but were not explicitly predicted by Reed. A table of frequencies observed, and an approximate measure of their relative strengths, is also presented as a function of magnetic field orientation.

ACKNOWLEDGEMENTS

Expressions of thanks are due several people. First and foremost, of course, is my supervisor Dr. W. R. Datars for his continued patience, guidance, and contributions during the course of this study. Thanks are due also to Mr. Clarence Verge for his technical advice, and to the members of the Fermi surface group for several helpful discussions. Special thanks are also due to Miss Vera Koval, not only for the drawings of the Fermi surface in figures 4 and 21-23, but for alternating admonishments to get back to work and finish this thesis, or to not work so hard. I am indebted also to Dr. W. A. Reed for making available many of the unpublished details of his calculations, and to Miss Shaenaeus Silver for volunteering sight-unseen to attempt the monumental task of deciphering my handwriting in order to type this thesis.

This research was supported through a research grant from the National Research Council of Canada. Personal financial support from McMaster University and the National Research Council of Canada is gratefully acknowledged.

TABLE OF CONTENTS

	Page
CHAPTER I	INTRODUCTION 1
CHAPTER II	BACKGROUND INFORMATION 4
	A. de Haas-van Alphen Theory 4
	1) Basic de Haas-van Alphen Theory 4
	2) Lifshitz-Kosevich Theory 7
	3) Modifications of the L-K Theory 16
	B. Ga crystal Structure and Brillouin Zone 24
	C. Previous Gallium Work 29
	D. The Pseudopotential Model for Gallium 33
CHAPTER III	EXPERIMENTAL PROCEDURE AND APPARATUS 39
	A. Sample Preparation 39
	B. Apparatus and Analysis 42
	1) Apparatus 42
	2) Data Analysis 45
	3) dHvA Frequency-Radii Inversion 48
CHAPTER IV	EXPERIMENTAL RESULTS 54
CHAPTER V	DISCUSSION 67
	A. Introduction 67
	B. Continuous Low Frequencies I 68
	C. Continuous Low Frequencies II 81
	D. Discontinuous Low Frequencies 95

	E. High Frequencies: Predictions	104
	F. High Frequencies for $8e$ at L	108
	G. High Frequencies for $\bar{H}\parallel a$	114
	H. High Frequencies for $\bar{H}\parallel c$	115
	I. High Frequencies for $\bar{H}\parallel b$	121
	J. Additional Topics	130
CHAPTER VI	CONCLUSIONS	135
APPENDIX		143
	A. Field Modulation Effects	143
	B. Ellipsoidal Fermi Surfaces	145
	C. Frequency Table	150
BIBLIOGRAPHY		164

LIST OF FIGURES

Figure Number		Page
1.	Gallium crystal structure in the xz plane	27
2.	Gallium crystal structure in the yz plane	28
3.	Gallium Brillouin zone	30
4.	Gallium Fermi surface according to Reed's model	34
5.	Block diagram of the experimental apparatus	44
6.	Block diagram of the data analysis programme	46
7.	dHvA frequencies in Gallium-low frequencies	58
8.	dHvA frequencies in Gallium-high frequencies	59
9.	$1/f^2$ plot for A6-B6-C7 (6h at T)	70
10.	Spherical harmonic expansion of several frequency branches	74
11.	Radius and ellipsoidal deviation for 6h at T	76
12.	Cross-sectional areas of 6h at T	77
13.	$1/f^2$ plot for A5-B5-C8 (7e near Γ)	80
14.	$1/f^2$ plot for A4-A7-B4-C9-C9' (7e between arms)	83
15.	Radius and ellipsoidal deviation for 7e between arms	86
16.	Cross-sectional areas of 7e between arms	87
17.	$1/f^2$ plot for B1, B2, and B3	90
18.	$1/f^2$ plot for A1, A2, and A3	91
19.	Radius and ellipsoidal deviation for 5h at X	93
20.	Cross sectional areas of 5h at X	94
21.	View of the gallium Fermi surface from the b direction	96

LIST OF FIGURES (cont.)

Figure Number		Page
22.	View of the gallium Fermi surface from the a direction	97
23.	View of the gallium Fermi surface from the c direction	100
24.	$1/f^2$ plot for B8 and B9	102
25.	$1/f^2$ plot for C2-5	103
26.	$1/f^2$ plot for A8-B11-C10	109
27.	Spherical harmonic expansion for 8e at L	111
28.	Radius and ellipsoidal deviation for 8e at L	112
29.	Cross-sectional areas of 8e at L	113
30.	$1/f^2$ plot for B12-13 and B19-21	120
31.	$1/f^2$ plot for C12	122
32.	$1/f^2$ plot for A8, A14-17	127

LIST OF TABLES •

Table Number	Page
1. Gallium crystal parameters	25
2. Spherical harmonic expansion parameters	72
3. Frequency assignments of branches observed	133
4. Frequencies at symmetry directions	141
5. Frequency table (Appendix C)	150

CHAPTER I

INTRODUCTION

Since its discovery in 1930, the de Haas-van Alphen (dHvA) effect has become one of the most powerful tools available to Fermiologists for determining the size and shape of Fermi surfaces. In simplest terms, the phenomenon is a variation of the magnetic susceptibility which is periodic in reciprocal magnetic field. It was originally thought to be peculiar only to bismuth, in which it was first discovered, but now is known to be applicable to single crystals of nearly all metals of the periodic table. It has also been used successfully with dilute metal alloys, some metallic compounds and even some metallic oxides, (e.g. ReO_3), in which the lack of metallic purity would seem to preclude the possibility of the dHvA effect existing. Similar oscillations have also been observed in the Hall effect, magnetoresistance, thermoelectric power, inter-metallic contact potentials, and magnetothermal effects. These are all quite useful, and are not to be ignored, but such oscillations are usually much more difficult to detect than oscillations in the magnetic susceptibility.

The choice of gallium as the object of this study is due to the fact that it is one of the few easily prepared pure

metals which has not been thoroughly investigated. The Fermi surface of gallium is extremely complicated, which makes both the experiment and the analysis very difficult. There have been several theoretical models proposed for the Fermi surface of gallium, and many experiments attempted in an effort to verify the various theories, but most such experiments have merely shown the inadequacy of the theories, and in addition have presented more inexplicable data. The present study is an attempt to resolve this dilemma. Chapter II gives the theoretical background necessary for the understanding of the dHvA effect, both a "seat-of-the-pants" version, which is easily understood but too simplified, and a more demanding mathematical treatment of the problem which, although quite logical, is not as easily understood, but gives the exact mathematical relationships necessary for the analysis. This chapter also contains a short summary of the crystal structure, Brillouin zone, and previous work on gallium, as well as a detailed description of the gallium Fermi surface according to the latest model. Chapter III gives the details of sample preparation, experimental apparatus, and computer analysis of the data. Chapter IV gives a summary of the experimental results obtained, along with an analysis of the sources of experimental error in this study. Chapter V relates the experimentally observed data to the model. The Appendix presents the modification of the theory necessitated by the experimental method, an

analysis of observations expected due to ellipsoidal Fermi surfaces, and a table of the data observed during the course of this study.

CHAPTER II

BACKGROUND INFORMATION

A.1 Basic dHVA theory

The simplest theory for the dHVA effect may be described in the following way. Suppose one has a free electron gas at absolute zero temperature. This is approximately the state of valence electrons in a metal at low temperatures. The Fermi surface for this system is a sphere of extremely dense discrete occupied states in momentum space. All quantum states within the sphere are occupied with a degeneracy of two (spin up and spin down), and all states outside the sphere are unoccupied. Suppose one now turns on a strong magnetic field \bar{H} . The energy of an electron moving within this field is now a function of this field, and is no longer given by $\epsilon_k = \frac{\hbar^2 |\bar{k}|^2}{2m}$, which is valid for a plane wave electron of momentum $\hbar k$ and mass m . Instead, the motion of the electron is governed by the Lorentz force equation:

$$\hbar \dot{\bar{k}} = \frac{e}{c} \bar{v} \times \bar{H}$$

where \bar{k} is the wave vector and \bar{v} is the velocity of the electron. This requires that the electron spiral around the direction of the applied field:

$$(1) \quad \alpha \bar{r} \times \hat{H} = -(\bar{k} - \bar{k}_0)$$

$$\alpha = \frac{eH}{\hbar c}$$

where \hat{H} is a unit vector in the direction of \vec{H} and \vec{r} is the electron's position. This real-space spiral corresponds to a momentum-space closed orbit whose plane is normal to \hat{H} , since the magnetic field cannot affect the component of momentum parallel to the field. If one then projects this real-space spiral onto a plane normal to \hat{H} , the Bohr-Sommerfeld quantization rule requires that for this projected orbit,

$$\oint (\hbar \vec{k} - \frac{e}{c} \vec{A}) \cdot d\vec{r} = (n + \gamma) 2\pi\hbar$$

where $\vec{A} = \nabla \times \vec{H}$ is the vector potential of the magnetic field, γ is a phase factor ($\frac{1}{2}$ for free electrons), and $\vec{p} = \hbar \vec{k} - \frac{e}{c} \vec{A}$ is the canonical momentum vector conjugate to the position vector \vec{r} . But the left side of this, using (1), is simply $\frac{e}{c}$ times the total flux of the magnetic field passing through the orbit. Since the orbital area in k -space is α^2 times the orbital area in real space, from (1), the orbital area in k -space must therefore be given by the Onsager relation:

$$(2) \quad A_n = 2\pi\alpha(n + \gamma)$$

This implies that the electrons are no longer allowed to occupy all possible states within the zero-field Fermi sphere, but are now constrained to occupy only those states lying on a series of tubes whose cross-sectional areas normal to the field differ by integral multiples of $2\pi\alpha$,

which is directly proportional to the strength of the field. Each such tube is termed a Landau level. Each level must be highly degenerate to make up for all the energy states now no longer allowed. Clearly, the degeneracy of each level must be field-dependent, since one may increase the field sufficiently to cause an occupied level inside the Fermi sphere to move outside the surface, at which point it must be unoccupied, and the electrons formerly occupying that level must now jump down to levels of lower energy. Since the magnetization in this simple model is given by:

$$(3) \quad M = -\frac{dU}{dH},$$

every time a Landau level pierces the Fermi surface the magnetization will jump to a higher value. However, as the field is increased, every Landau level acquires a larger cross-sectional area, so that the electrons on each level acquire a higher energy, causing a continuous decrease in magnetization. The net effect therefore is for the magnetization to steadily decrease as the field is raised until a Landau level is tangent to the Fermi surface. At this point the magnetization jumps to a higher value and the magnetization decrease begins again. This saw-tooth oscillation is the dHVA effect, unadulterated by such things as non-zero temperatures, lattice potentials changing the degeneracy of the Landau levels, crystal defects, magnetic breakdown, collision broadening and Zeeman splitting of each

Landau level, and the difference between magnetic induction $\bar{B} = \bar{H} + 4\pi\bar{M}$ and the applied field \bar{H} requiring a self-consistent solution to the problem. It also does not account, of course, for experimental techniques of data acquisition, which now generally include modulation of the applied field \bar{H} and/or modulation of the crystal orientation.

Finally, it should be noted that this in no way contradicts the fact that a magnetic field cannot do work on a moving charged particle, and thus change its energy. What the magnetic field does do is to change the allowed Landau levels of the system, but each Landau level may have electrons of many different energies. Only when a Landau level is just tangent to the Fermi surface is the energy of an electron on that level (and therefore at the tangent point) uniquely defined.

A.2 Lifshitz-Kosevich theory

Having acquired this rough understanding of the dHVA effect, one may now turn to the details of the semi-classical theory proposed by Lifshitz and Kosevich (L-K) in 1955, as reviewed by Gold in 1968. This theory has built into it solutions to many of the problems just cited above. The magnetization corresponding to (3) now becomes

$$\bar{M} = - \nabla_{\bar{H}} \Omega |_{T}$$

where the free energy Ω per unit volume for an electron gas

in a metal is given by:

$$(4) \quad \Omega = N\epsilon_f + k_B T \sum_{\epsilon} \ln(1 - f_0(\epsilon))$$

and the gradient is evaluated at constant temperature. N is the total number of conduction electrons per unit volume, ϵ_f is the Fermi energy, $f_0(\epsilon)$ is the Fermi-Dirac distribution function, and the summation is over all possible energy states available to the system. To perform this sum one follows the usual procedure of first making it more complicated. The volume enclosed by the Fermi surface is sliced into many slabs of thickness dk_H normal to \hat{H} , and then each slab is cut into rings of thickness $d\epsilon$ in energy. A density of states ϕ_0 is then defined such that the number of energy states in this ring is given by

$$(5) \quad dn(\epsilon, k_H, \hat{H}) = \phi_0(\epsilon, k_H, \bar{H}) d\epsilon dk_H$$

The sum in (4) then becomes an integral

$$\Omega = N\epsilon_f + k_B T \int dk_H \int_{-\infty}^{\infty} \phi_0(\epsilon, k_H, \bar{H}) \ln(1 - f_0(\epsilon)) d\epsilon$$

which one integrates twice by parts (the constant term being zero in each case) to get

$$(6a) \quad \Omega = N\epsilon_f + \int dk_H \int_{-\infty}^{\infty} \phi_2(\epsilon, k_H, \bar{H}) \frac{\partial f}{\partial \epsilon} d\epsilon$$

$$(6b) \quad \phi_2(\epsilon, k_H, \bar{H}) = \int_{-\infty}^{\epsilon} d\epsilon' \int_{-\infty}^{\epsilon'} \phi_0(\epsilon'', k_H, \bar{H}) d\epsilon''$$

Up to this point the calculations have been exact, since we haven't really done anything. But now one must find an expression for the density of states ϕ_0 before one can integrate it four times. This requires a series of assumptions and approximations. The first is that one is

interested only in those Landau levels near the Fermi surface, since it is the changes in the populations of these levels which cause the oscillatory magnetization sought. This is not a very serious assumption, but if one ignores Zeeman splitting of the energy levels it does allow one to expand the energy of each ring in the slab in terms of the area of each level and the area at the Fermi energy:

$$(7) \quad \epsilon_n = \epsilon_f + \frac{d\epsilon}{dA} (A_n - A_f) + \dots$$

The energy difference $d\epsilon$ between two adjacent levels is $\hbar\omega_c$, where

$$\omega_c = \frac{eH}{m^*c} = \alpha \frac{\hbar}{m^*}$$

is the cyclotron frequency and m^* is the effective mass. The area difference dA between two adjacent levels is given by (2) as $2\pi\alpha$. Therefore, to first order,

$$(8) \quad \epsilon_n = \epsilon_f + \frac{\hbar\omega_c}{2\pi\alpha} (2\pi\alpha(n + \gamma) - A_f)$$

There are an average of two states (spin up and spin down) per unit volume $(2\pi)^3$ in k -space, and the ring on which one defines ϕ_0 in (5) has an area dA . Therefore, if $D(\epsilon, k_H, \bar{H})$ is an energy density function, which is not yet known, one has:

$$\phi_0(\epsilon, k_H, \bar{H}) = \frac{2}{(2\pi)^3} \frac{dA}{d\epsilon} D(\epsilon, k_H, \bar{H})$$

To define D requires another assumption. If the Landau levels were perfectly sharp, then D would be a series of delta functions at energies determined by (8) :

$$\phi_0(\epsilon, k_H, \bar{H}) = \frac{m^*}{2\pi^2 \hbar^2} \sum_n \delta(\mathcal{Y}(\epsilon, k_H, \bar{H}) - n)$$

$$(9) \quad \mathcal{Y}(\epsilon, k_H, \bar{H}) = \frac{\epsilon - \epsilon_f}{\hbar\omega_c} + \frac{A_f}{2\pi\alpha} - \gamma$$

However, this cannot be the case in real metals for several reasons. First, there is a finite possibility that an electron in a given state will be scattered out of that state by a collision. Each level thus has a non-infinite lifetime and therefore a non-zero width, by the uncertainty principle. Second, crystal defects also contribute to scattering mechanisms, thus decreasing the lifetime of the state still further. Third, the lattice potential destroys the magnetic degeneracy of each level, which broadens the level directly. However, the levels should still be centred at the energies given by (8). Therefore, one assumes phenomenologically that each sharp delta function level may be replaced by a single-peaked distribution whose half-width Γ is independent of energy and magnetic field. The distribution normally chosen is a normalized Lorentzian wave:

$$\phi_0(\epsilon, k_H, \bar{H}) = \frac{m^*}{2\pi^2 \hbar^2} \sum_{n=-\infty}^{\infty} \frac{1}{\pi} \frac{a}{(\mathcal{Y}(\epsilon, k_H, \bar{H}) - n)^2 + a^2}$$

where $a = \frac{\Gamma}{\hbar\omega_c}$. The sum has been extended to all integers here because when this is eventually inserted into (6a), only those levels near the Fermi surface will contribute due to the derivative of the Fermi function.

The physics of the problem is now essentially done, and one has only some complicated mathematics to perform. Using the Poisson sum formula

$$\sum_{n=-\infty}^{\infty} f(n) = \int_{-\infty}^{\infty} f(x) dx + 2 \sum_{r=1}^{\infty} \int_{-\infty}^{\infty} f(x) \cos 2\pi r x dx$$

the density of states becomes:

$$(10) \quad \phi_0(\epsilon, k_H, \bar{H}) = \frac{m^*}{2\pi^2 \hbar^2} \left(1 + 2 \sum_{r=1}^{\infty} e^{-2\pi r a} \right) \times \cos[2\pi r \gamma(\epsilon, k_H, \bar{H})]$$

Inserting this in (6b) and retaining only the oscillatory terms, one has:

$$\phi_2(\epsilon, k_H, \bar{H}) = -\frac{m^*}{\pi^2 \hbar^2} \sum_{r=1}^{\infty} \left(\frac{\hbar \omega_c}{2\pi r} \right)^2 K_r \times \cos 2\pi r \left[\frac{\epsilon - \epsilon_f}{\hbar \omega_c} + \frac{A_f}{2\pi a} - \gamma \right]$$

$$(11) \quad K_r = e^{-2\pi r a} = \exp\left(-\frac{\pi \Gamma}{\mu_B} \frac{m^*}{m} \frac{r}{\bar{H}}\right)$$

where $\mu_B = \frac{e\hbar}{2mc}$ is the Bohr magneton. Continuing in (6a),

the oscillatory part of the free energy becomes:

$$(12) \quad \Omega = \frac{\alpha^2 \hbar^2}{4\pi^4 m^*} \sum_{r=1}^{\infty} \frac{I_r K_r}{r^2} \int \cos 2\pi r \left(\frac{A_f}{2\pi a} - \gamma \right) dk_H$$

$$I_r = - \int_{-\infty}^{\infty} \cos 2\pi r \left(\frac{\epsilon - \epsilon_f}{\hbar \omega_c} \right) \frac{df_0(\epsilon)}{d\epsilon} d\epsilon$$

$$(13) \quad = \int_{-\infty}^{\infty} (e^{\eta} + 1)^{-2} \exp\{(1 + iX_r/\pi)\eta\}$$

$$X_r = 2\pi^2 \frac{k_B T}{\hbar \omega_c} r = \frac{\pi^2 k_B}{\mu_B} \left(\frac{m^*}{m} \right) \frac{T}{\bar{H}} r$$

$$\eta = \frac{\epsilon - \epsilon_f}{k_B T}$$

Note that in (13) one really wants only the real part of the integral. However, the imaginary part of the integrand is an odd function of η so it contributes nothing. The integral may now be done using contour integration, choosing a contour encompassing the upper half of the complex plane, the integral at infinity contributing nothing. The poles of the integrand occur whenever $e^\eta = -1$, or whenever

$$\eta_m = (2m + 1)i\pi \quad m = 0, \pm 1, \pm 2, \dots$$

Since the poles are each of second order, the residue of the m^{th} pole η_m is given by:

$$\begin{aligned} \text{Res}_m &= \frac{d}{d\eta} \left((\eta - \eta_m)^2 (e^\eta + 1)^{-2} e^{(1 + ix_r/\pi)\eta} \right) \Big|_{\eta_m} \\ &= -\frac{i}{\pi} x_r e^{-(2m+1)x_r} \end{aligned}$$

It should be noted that this simple result comes only after three successive applications of l'Hôpital's Rule for evaluating indefinite quantities. Summing over all the poles, one obtains:

$$(14) \quad I_r = \frac{x_r}{\sinh x_r}$$

The remaining integration over k_H in (12) requires a return to the physics of the problem. The Fermi surface cross-sectional area A_f in the argument of the cosine

depends upon k_H . However, from (2), this argument is approximately $2\pi r n$, where n is the number of occupied Landau levels. How big is n ? Suppose one has a free-electron gas in a field of 100kG. This is approximately the highest steady magnetic field easily obtainable in superconducting solenoids, and a smaller value would only decrease the Landau level spacing and thus increase n .

The Fermi surface will be a sphere of energy $\epsilon_f = \frac{\hbar^2}{2m} (3\pi^2 N_0)^{2/3}$ where N_0 is the electron density in real space. The Fermi radius is therefore $(3\pi^2 N_0)^{1/3}$, and ignoring the phase γ one has

$$n \approx \frac{A}{2\pi\alpha} = \frac{\hbar c}{2eH} (3\pi^2 N_0)^{2/3}$$

Choosing $N_0 \approx 6 \times 10^{22}/\text{cm}^3$, which is approximately the value for silver or gold, one finds $n \approx 4800$. Reducing N_0 to about $10^{22}/\text{cm}^3$, the approximate value for cesium, reduces n to about 1500. In other words, the argument of the cosine in (12) is expected to be quite large, and small changes in A_f from one slice to the next in k_H will cause large changes in the integrand. The contributions from neighbouring slices will therefore add with destructive interference except at extremal values of the cross-sectional area. It is therefore justifiable to expand A_f about these extremal values A :

$$(15) \quad A_f = A \pm \frac{1}{2} \left| \frac{\partial^2 A_f}{\partial k_H^2} \right|_A k_H^2 + \dots$$

The upper sign is for maximal areas, the lower sign for minimal areas, and k_H is measured from the position of the extremal area. If one now defines

$$(16) \quad F = \frac{A}{2\pi\alpha} H = \frac{c\hbar A}{2\pi e}$$

$$u_r^2 = \frac{r}{\pi\alpha} \left| \frac{\partial^2 A_f}{\partial k_H^2} \right|_A k_H^2 \equiv \xi_r^2 k_H^2$$

then (12) becomes:

$$\Omega = \frac{\alpha^2 \hbar^2}{4\pi^4 m^*} \sum_{r=1}^{\infty} \frac{I_r K_r}{r^2 \xi_r} \int_{-\infty}^{\infty} \cos(2\pi r F/H - 2\pi r \gamma) \mp \frac{\pi}{2} u^2) du$$

Using the Fresnel integrals

$$\int_{-\infty}^{\infty} \sin \frac{\pi}{2} x^2 dx = \int_{-\infty}^{\infty} \cos \frac{\pi}{2} x^2 dx = 1$$

and rearranging coefficients, one has:

$$(17a) \quad \Omega = -\left(\frac{H^2}{2\pi F}\right) D(H) \sum_{r=1}^{\infty} \frac{I_r K_r}{r^{5/2}} \cos[2\pi r(F/H - \gamma) \mp \frac{\pi}{4}]$$

$$(17b) \quad D(H) = -\frac{e\hbar A}{4\pi^4 m^* c} \left(\frac{2\pi e H}{\hbar c}\right)^{1/2} \left| \frac{\partial^2 A_f}{\partial k_H^2} \right|_A^{-1/2} \\ = -\frac{r_0 F}{2\pi^3} \left(\frac{m}{m^*}\right) \left(\frac{2\pi e H}{\hbar c}\right)^{1/2} \left| \frac{\partial^2 A_f}{\partial k_H^2} \right|_A^{-1/2}$$

where $r_0 = e^2/mc^2$ is the classical electron radius. Therefore, the oscillatory part of the magnetization is given by

$$(18) \quad \bar{M}(\bar{H}) = D(H) \left(\hat{H} - \frac{1}{F} \frac{\partial F}{\partial \theta} \hat{\theta} - \frac{1}{F \sin \theta} \frac{\partial F}{\partial \phi} \hat{\phi} \right) \\ \times \sum_{r=1}^{\infty} \frac{I_r K_r}{r^{3/2}} \sin\left\{2\pi r \left(\frac{F}{H} - \gamma\right) \mp \frac{\pi}{4}\right\}$$

where $(\hat{H}, \hat{\theta}, \hat{\phi})$ is a set of orthogonal unit vectors in spherical co-ordinates. Only the cosine term was differentiated in achieving this since by comparison the leading terms are only slowly varying.

This shows that the magnetization as a function of \bar{H} is an amplitude, which varies only slowly with H , times a direction, which is nearly that of \bar{H} , times a sum of an oscillatory function and all its harmonics, each harmonic having a different damping factor, and the fundamental frequency being directly proportional to the extremal cross-sectional area of the Fermi surface. It should be noted that the independent variable is $1/H$ rather than H .

Various features of (18) are now worth mentioning. First, \bar{M} and \bar{H} are not parallel except when $\frac{\partial A}{\partial \theta}$ and $\frac{\partial A}{\partial \phi}$ are both zero, which normally occurs only when \bar{H} is along a principle symmetry direction of the crystal. Second, the temperature enters only in I_r , which is an attenuation factor for each harmonic. Inserting the numbers, one finds

$$x_r = 1.47 \times 10^5 \left(\frac{m^*}{m}\right) \frac{T}{H} r$$

where H is in gauss and T in $^{\circ}K$. For free electrons

($m^* = m$) at 50kG and 1K, this is approximately $3r$. The attenuation factor for the fundamental is thus 30%, for the second harmonic it is 3%, and the third harmonic 0.2%.

The other harmonic attenuation factor K_r is due solely to the finite lifetime and non-zero width Γ of the Landau levels, and this is the only term in which Γ enters. By analogy with x_r one may define an effective temperature known as the Dingle temperature T_D by (Dingle 1952):

$$T_D = \frac{\Gamma}{\pi k_B}$$

For a Dingle temperature of 1K, $\Gamma \sim 0.27\text{meV}$, which is approximately 15% of the free electron level separation at 50kG. For free electrons at 50kG, one has $K_r \sim e^{-3r}$, which is approximately 5.3% for the fundamental, 0.28% for the second harmonic, and 0.015% for the third harmonic.

Obviously, with both I_r and K_r reducing the higher harmonics, one need consider only a few terms in (18) unless m^* is small. Also, with only a few harmonics to work with, one cannot expect to see anything like a saw-tooth signal, which would require quite high harmonics in its Fourier spectrum.

A.3 Modifications of the L-K Theory

We return now to a discussion of the various assumptions and approximations used in deriving (18), and

the consequences of lifting some of the restrictions. The first and most obvious problem is that of Zeeman splitting of the Landau levels due to the interaction of the electron spin with the field. Each state at zero field contains two electrons of opposite spin, and is split into two single electron states for non-zero field separated by an amount $g\mu_B H = g\hbar H/2mc$, where g is the spin-splitting g -factor. g is approximately 2.0023 for free electrons, but may not necessarily be that value in a real metal due to spin-orbit coupling changing the direction of the spin moment. Since every state is split, every Landau level will also be split, and by the same amount $g\mu_B H$. The set of levels forming the higher energy half of each pair of spin-split levels will still have a separation between levels of $\hbar\omega_c = \hbar eH/m^*c$, as will the lower set of levels, and the discussion of the previous section will otherwise be unaffected. By examining (9) one sees that changing the energy of a level by an amount

$$\Delta\varepsilon = \pm \frac{1}{2}g\mu_B H = \pm \hbar\omega_c \frac{gm^*}{4m}$$

is equivalent to changing the phase by an amount

$$\Delta\gamma = \mp \frac{gm^*}{4m}$$

In computing the total magnetization in (18), therefore, half the signal will come from the upper set of levels with a

phase decrease, and half will come from the lower with a phase increase. Therefore, one has:

$$\bar{M}(\bar{H}) = \frac{1}{2} \bar{M}(\bar{H}, \gamma + \frac{gm^*}{4m}) + \frac{1}{2} \bar{M}(\bar{H}, \gamma - \frac{gm^*}{4m})$$

$$\begin{aligned} \text{i.e. (19)} \quad \bar{M}(\bar{H}) &= D(H) \left[\hat{H} - \frac{1}{F} \frac{\partial F}{\partial \theta} \hat{\theta} - \frac{1}{F \sin \theta} \frac{\partial F}{\partial \phi} \hat{\phi} \right] \\ &\times \sum_{r=1}^{\infty} \frac{I_r K_r}{r^{3/2}} \sin[2\pi r(F/H - \gamma) \mp \frac{\pi}{4}] \cos\left(\frac{\pi gm^* r}{2m}\right) \end{aligned}$$

The only consequence of including Zeeman splitting, therefore, is to add a factor $\cos(r\pi gm^*/2m)$ to the amplitude of the r^{th} harmonic. This immediately leads to the conclusion that if $gm^* = m$, then the fundamental frequency F and all its odd harmonics will be non-observable; only the even harmonics will appear in the sum. Since m^* may, and usually will, change as a function of \hat{H} , it is possible for the frequency due to a particular piece of Fermi surface to disappear at certain crystal orientations.

The next problem is that of multi-band and multi-connected Fermi surfaces. Nothing in the foregoing discussion (except for order-of-magnitude calculations) assumed that the Fermi surface was a single piece or that the Fermi surface in one zone was not connected to the Fermi surface in the next zone in the extended zone scheme. Nor was anything assumed about the shape of the surface. Therefore one need only sum (19) over all possible extremal areas regardless of how they were formed. However, a problem

could occur for very small pieces of Fermi surface in that the number of filled Landau levels within the surface may not be large enough for the expansion (15) of the cross-sectional area to be valid. From (16) and (2) one has $F \approx H(n + \gamma)$. If one is operating at 50kG, then this question becomes relevant for frequencies below approximately 5MG; for operations at 5kG, one must be careful below frequencies of about 0.5MG. This will be dealt with again in Chapter IV.

The expansion (15) could also be invalid for another reason. The factor $\left| \frac{\partial^2 A_F}{\partial k_H^2} \right|_A$ corresponds to the curvature of the Fermi surface as a function of k_H . If the field is in the \hat{z} direction, then the cross-section of an oddly shaped piece of Fermi surface may be passing through a minimum in the \hat{x} direction and a maximum in the \hat{y} direction as a function of z , and still form an extremal cross-section. A doughnut with symmetry axis along the \hat{x} direction and whose hole has been replaced by a thin sheet of surface (so that the cross-section in any plane containing the x axis looks like a set of barbells) could be an example of such. For this example, the cross-sections at the planes $z =$ constant will pass through a very shallow maximum as a function of z at the $z=0$ plane. The curvature will therefore be very small, and the fourth derivative in the expansion (15) will be the most important correction term,

rather than the second, all odd order derivatives being zero at the extremum by symmetry. If the p^{th} derivative in (15) is dominant (p must be even), then the calculations are nearly identical to the previous results. The frequency is invariant, but the phase and amplitude are changed:

$$(20) \quad \bar{M}(\bar{H}) = \sum_i D_i(H) \left[\hat{H} - \frac{1}{F_i} \frac{\partial F_i}{\partial \theta} \hat{\theta} - \frac{1}{F_i \sin \theta} \frac{\partial F_i}{\partial \phi} \hat{\phi} \right] \\ \times \sum_{r=1}^{\infty} \frac{I_{ri} K_{ri}}{r r^{1/p_i}} \sin \left[2\pi r \left(\frac{F_i}{H} - \gamma \right) \mp \frac{\pi}{2p_i} \right]$$

$$D_i(H) = - \Gamma \left(1 + \frac{1}{p_i} \right) \left(\frac{eH}{\hbar c} p_i \right)^{1/p_i} \left| \frac{\partial P_i A_f}{\partial k_H p_i} \right|^{-1/p_i} \frac{r_0 F_i}{\pi^3} \frac{m}{m^*}$$

$$I_{ri} = \frac{x_{ri}}{\sinh x_{ri}}$$

$$x_{ri} = \pi^2 \frac{k_B}{\mu_B} \left(\frac{m_i^*}{m} \right) \frac{T}{H} r$$

$$K_{ri} = \exp \left(- \frac{\pi \Gamma}{\mu_B} \frac{m_i^*}{m} \frac{r}{H} \right)$$

The sum on i is over each piece of the fermi surface, and $\Gamma(x)$ is the gamma function (not to be confused with the level width Γ). The primary difference between this and (18) is that $D_i(H)$ has less dependence on H than does $D(H)$, and it contains the higher order derivative of the extremal area. Since this derivative is numerically greater than the second derivative and appears in the denominator, it reduces the amplitude from what one would expect from the second derivative.

Another problem with (18), which will not be treated

here, is the fact that one should use $\bar{B} = \bar{H} + 4\pi\bar{M}$ as the applied field within the crystal rather than the field \bar{H} applied outside the crystal. It can be shown (Gold, 1968) that the dHvA frequencies do not change under these conditions, but the amplitudes do. Also, the crystal becomes capable of mixing frequencies from several different pieces of Fermi surfaces so that the harmonics, sums, and differences of the fundamental frequencies are enhanced.

Finally, there is the problem of magnetic breakdown. If two pieces of Fermi surface are close together but separated by a very small gap, then there is a finite probability that an electron in traversing one piece of the surface will jump the gap, i.e. tunnel through the energy barrier, and traverse the other piece of surface. It can be shown (Chambers, 1966a) that the probability of such occurring is approximately $e^{-H_0/H}$ for some critical field H_0 , which depends upon the geometry of the gap. Therefore, if an orbit 1 exists at low field without magnetic breakdown, but is transformed into an orbit 2 at high field through magnetic breakdown, then the amplitude of the dHvA frequency due to orbit 1 will decrease markedly as H is raised above H_0 , while the amplitude of the frequency for orbit 2 will increase at the same time. The field H_0 will be different for different gap geometries, and thus a given material may have a whole range of breakdown fields,

depending on the crystal orientation relative to the field, and the particular pieces of the Fermi surface under consideration. At fields sufficiently low to cause no breakdown, (19) or (20) is certainly valid, as it would be with a different set of orbits if the field were sufficiently high to cause total magnetic breakdown. Between these two limits in the region of partial magnetic breakdown, the enumeration of the energy density can be an appalling project even for a crystal with only a single type of gap, because this gap is repeated throughout the crystal at every symmetry related point, at each of which one must consider the probability of the gap being crossed.

A simple analysis proceeds as follows. Ordinary collisions without magnetic breakdown reduce the amplitude of each harmonic by the factor K_r given in (11) or (20). These collisions remove an electron from a given orbit and put it in another unrelated orbit. Magnetic breakdown also removes an electron from a given orbit, so by analogy one can assume it will merely add another reduction factor. If an orbit has n identical junctions at which magnetic breakdown may occur, and at m of these junctions it actually does occur, and the probability of such occurring at a given junction is $p = 1 - q = e^{-H_0/H}$, then the reduction factor for the r^{th} harmonic should be

$$R_r = [p^m q^{n-m}]^r$$

This is then multiplied by K_r for each harmonic in the expression (10) for the oscillatory portion of the density of states, which must then be summed over all possible orbits one could generate by magnetic breakdown, weighing each term in the sum by the number of such orbits in the crystal. Clearly even this simplest case is a monumental task in combinatorial analysis which cannot be attempted here. However, the result, even if attainable would only give an expression for the amplitudes of dHvA frequencies which are nearly the sums and/or differences of appropriate combinations of low-field fundamental frequencies.

A more fundamental question concerning magnetic breakdown is also raised, and that is exactly which orbits should one count? The theory requires only extremal orbits, but what constitutes an extremal orbit? The derivation of the dHvA effect assumed that each orbit, whether extremal or non-extremal, was contained entirely on one piece of the Fermi surface. Because of the very nature of magnetic breakdown, orbits caused by magnetic breakdown are not contained on a single piece of surface, thus failing to satisfy this basic condition. Therefore, such orbits need not satisfy in their entirety the condition of being extremal, since that condition is a secondary condition. However, one must still insist that most of the orbit be piecewise extremal. In other words, a given orbit may be a minimal

orbit on one piece of Fermi surface, but a maximal orbit on another piece of surface connected to the first by magnetic breakdown, or it may not even be an extremal orbit at all on certain parts of its path, provided these parts constitute only a small part of the total orbit. The very existence of magnetic breakdown forces one to consider non-extremal sections of small parts of the surface if they could be connected by magnetic breakdown to extremal sections of larger parts of the surface.

B. Ga Crystal Structure and Brillouin Zone

The crystal structure of gallium was of interest for quite some time. Bradley (1935) determined it to be orthorhombic with 8 atoms to an orthorhombic cell of dimensions given in Table 1, column 1. These were later refined (Barret, 1961) at low temperature to those given in columns 2 and 3. Since a and b are nearly equal, the structure can also be termed pseudotetragonal, but it is perhaps more significant that c/b is only 1.8% smaller at 2.35K than the ideal $c/a = \sqrt{3}$ ratio for hexagonal structures, as will be seen.

The positions of the Ga atoms in an orthorhombic cell are also shown in Table 1. Figures 1 and 2 (Slater, Koster, and Wood, 1962) show the positions of the atoms in the $y=0$, $y=\frac{1}{2}b$, $x=0$, and $x=-\frac{1}{2}a$ planes. Deformed hexagonal rings of atoms are visible in the first two planes, and the

TABLE 1Lattice Constants of Ga (\AA)

Parameter	Bradley (1935) 18 C	Barrett (1961) 4.2 K	Barrett (1961) 2.35 K
a	4.5167	4.5156 \pm 0.0001	4.5151 \pm 0.00005
b	4.5107	4.4904 \pm 0.0001	4.4881 \pm 0.00007
c	7.6648	7.6328 \pm 0.0001	7.6318 \pm 0.00008

Ga Atomic Sites

$(m, 0, p)$	$(m + \frac{1}{2}, \frac{1}{2}, -p)$
$(-m, 0, -p)$	$(-m + \frac{1}{2}, \frac{1}{2}, p)$
$(m + \frac{1}{2}, 0, -p + \frac{1}{2})$	$(m, \frac{1}{2}, p + \frac{1}{2})$
$(-m + \frac{1}{2}, 0, p + \frac{1}{2})$	$(-m, \frac{1}{2}, -p + \frac{1}{2})$

$$m = 0.0785 \pm 0.0005$$

$$p = 0.1525 \pm 0.0005$$

TABLE 1 (cont.)

Ga Nearest Neighbours

# of neighbours	distance (Å)
1	2.4332
2	2.7039
2	2.7266
2	2.7844
2	3.7196
4	3.9434

Figure 1. Crystal structure of gallium in the planes $y = 0$ and $y = \frac{1}{2}b$. Atoms are drawn to scale as spheres using the covalent radius given in the text. Numbers indicate nearest neighbours of the atom marked "0".

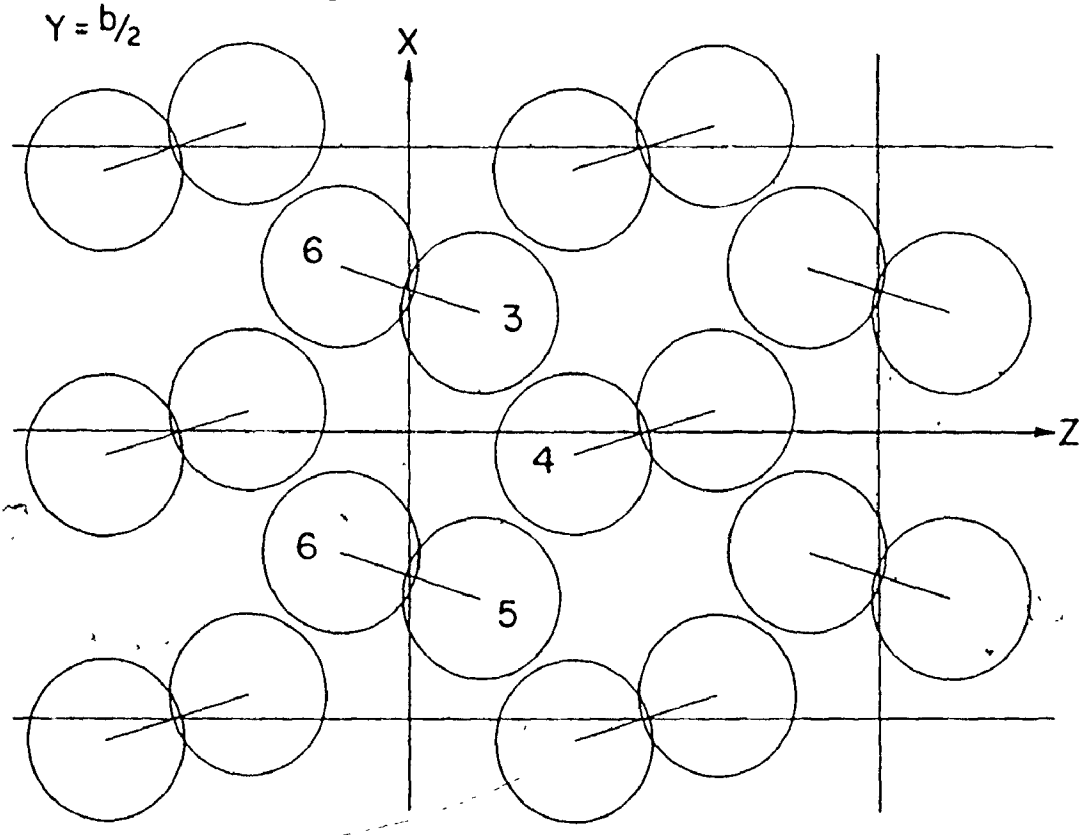
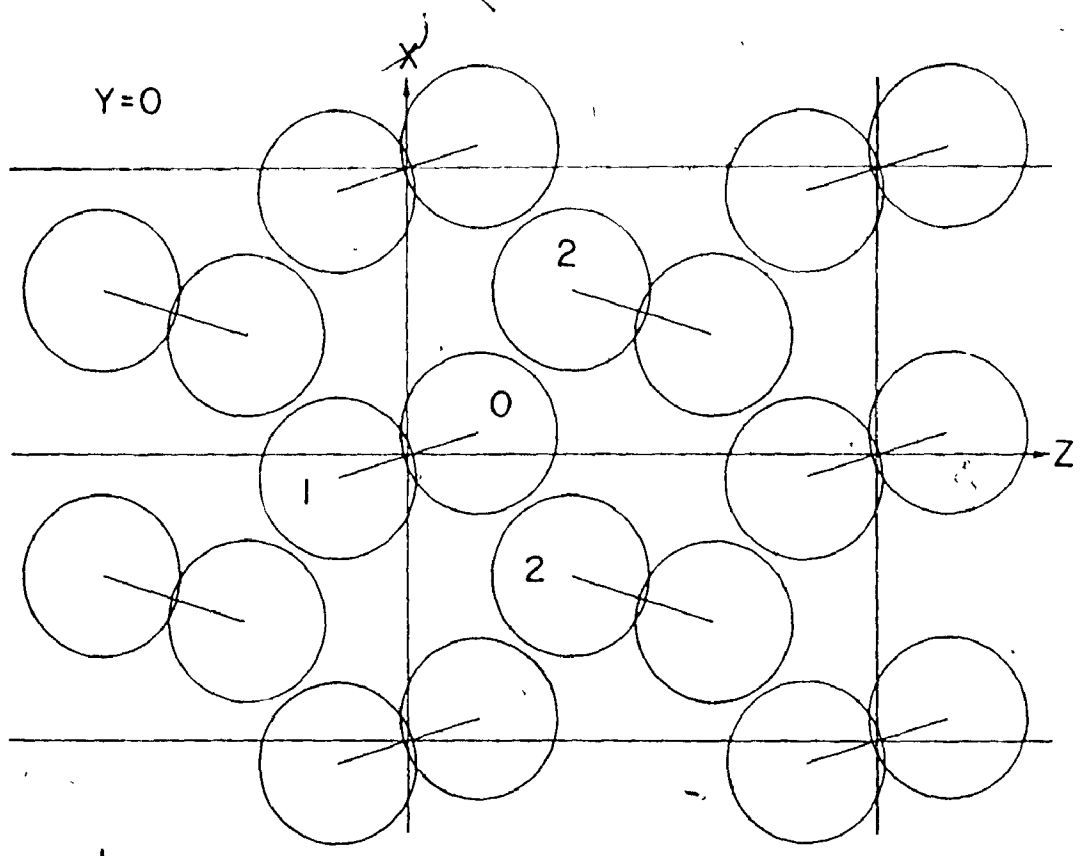
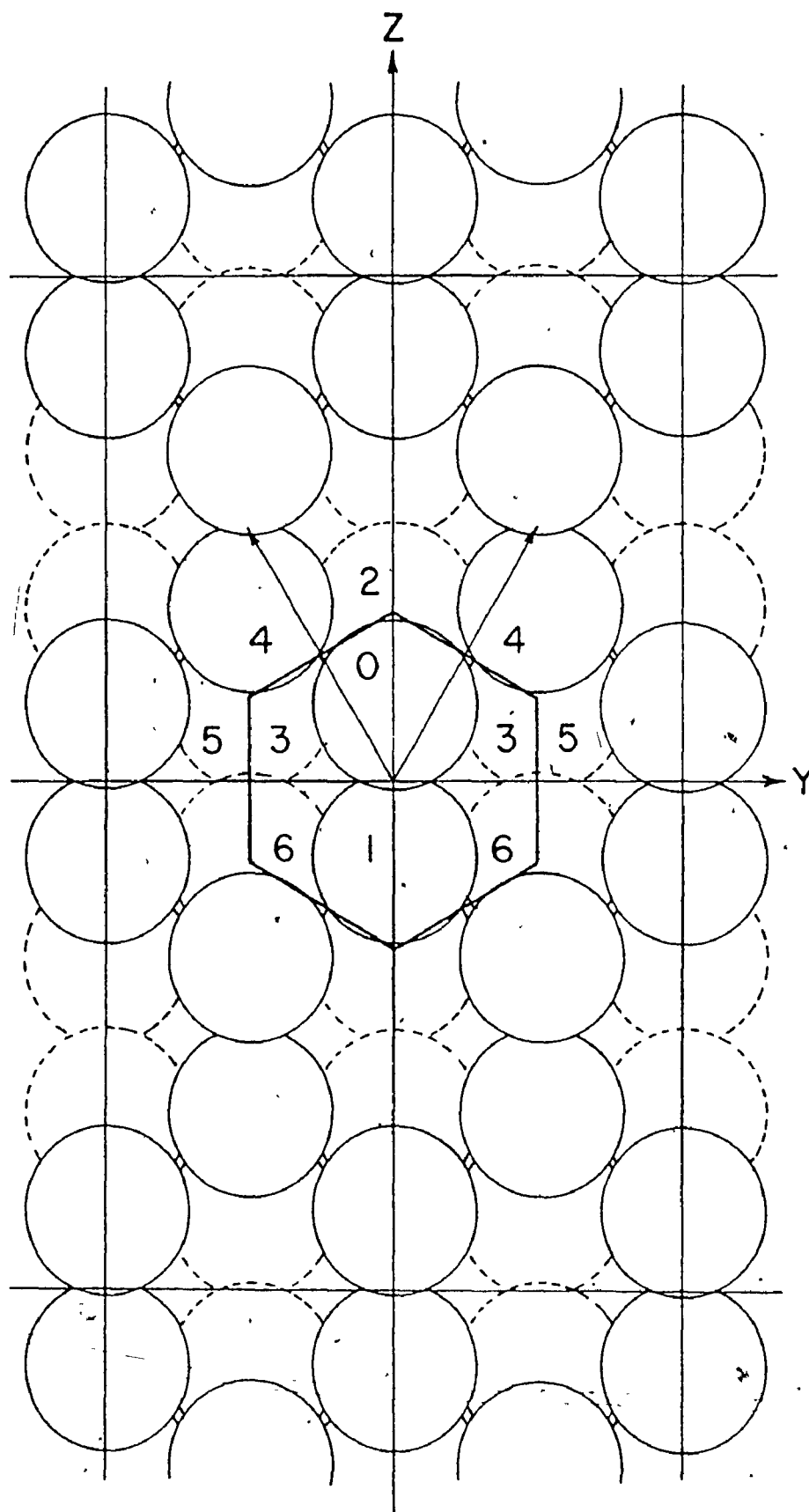


Figure 2. Crystal structure of gallium in the planes $x = 0$ and $x = -\frac{1}{2}a$. Atoms are drawn to scale as spheres using the covalent radius given in the text. Numbers indicate nearest neighbours of the atom marked "0". The third nearest neighbour has the y and z co-ordinate indicated, but is part of a pair of atoms centred on the plane $x = +\frac{1}{2}a$.



— $X=0$

- - - $X=-a/2$

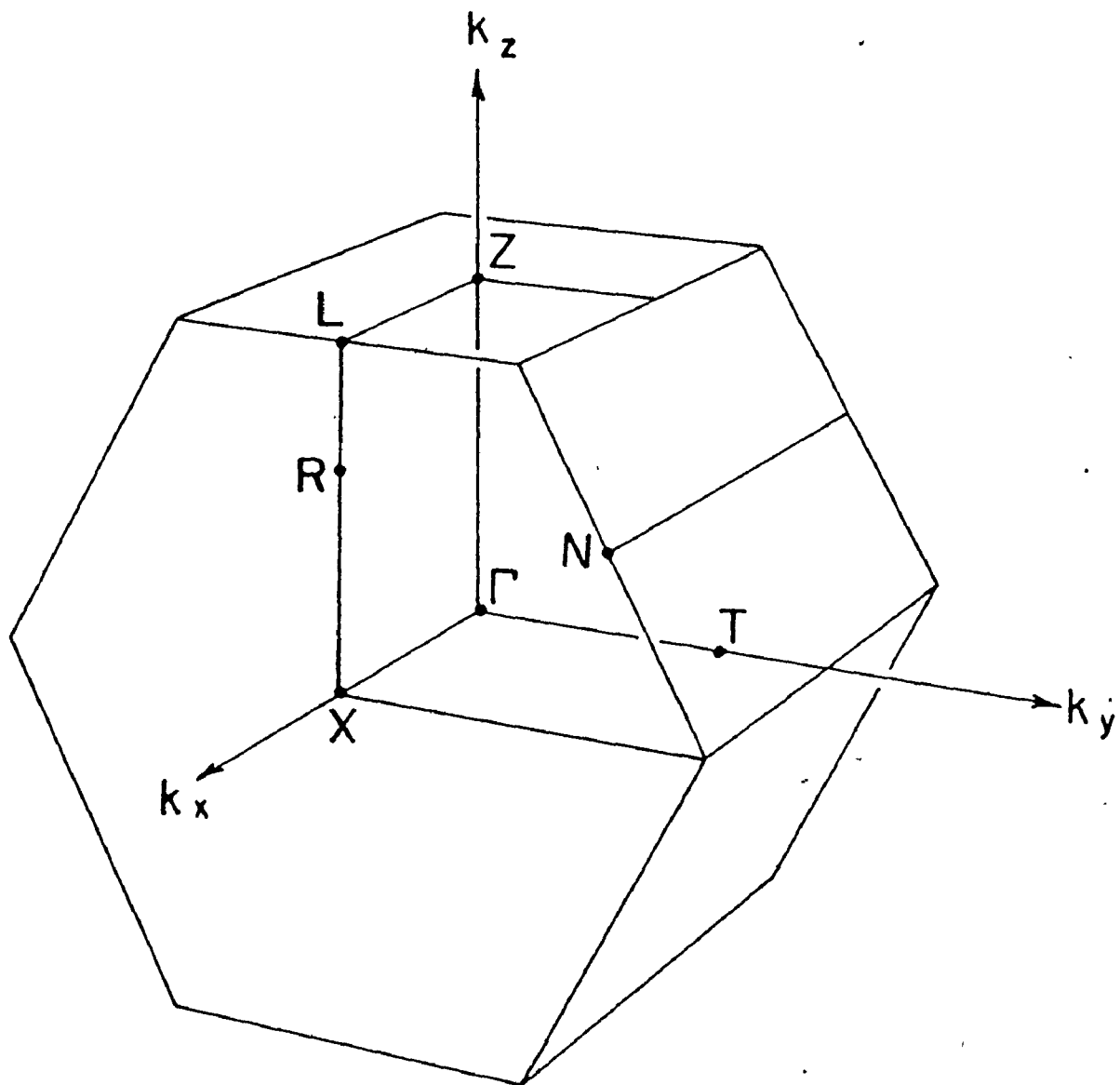
second two exhibit 6-membered rings of atoms with alternate members lying slightly above or below (by the distance ma , see Table 1) the plane of the ring. Each atom has nearest neighbours as given in Table 1 for a temperature of 2.35K. These are also indicated in Figures 1 and 2. For comparison, the atomic radius of gallium is approximately 1.41\AA , the covalent radius is 1.26\AA , and the bond length of a Ga-Ga bond is 2.442\AA at 20°C . The crystal therefore appears to be a structure of Ga_2 molecules rather than Ga atoms.

Since the plane of atoms at $y = 0$ is the same as that at $y = b/2$ except for a shift of $c/2$ in the \hat{z} direction, one may choose a unit cell with only 4 atoms rather than the 8 in the orthorhombic cell. Figure 2 shows two of the three vectors needed to form the cell in real space, the third vector being one lattice spacing in the \hat{x} direction. This leads to the hexagonal Wigner-Seitz cell shown in Figure 2, and a hexagonal Brillouin zone shown in figure 3 which appears to be the same as the Wigner-Seitz cell except for the rotation of $\pi/2$ in the yz plane. The zone boundary k_c in the k_z direction is $2\pi/c = 0.8233\text{\AA}^{-1}$ from the zone centre Γ , while the zone boundary in the direction of the other 4 sides of the hexagon is $[(\frac{\pi}{b})^2 + (\frac{\pi}{c})^2]^{1/2} = 0.8121\text{\AA}^{-1}$ from Γ . The boundary in the k_x direction is $k_a = \pi/a = 0.6958\text{\AA}^{-1}$ from Γ .

C. Previous Ga Work

The electronic properties of gallium have been

Figure 3. The Brillouin zone of gallium showing
some of the crystallographic points
of interest in this study.



studied using almost every method available. All in their own ways have contributed information, but few until recently have yielded information significant enough or comprehensive enough to solve the problem. Among the earliest techniques was the dHvA effect itself (Shoenberg, 1949, 1952, 1957), using magnetic fields up to about 16kG. Due to this limit, however, only the lowest dominant frequencies and occasionally a beat frequency were observed. The data were interpreted in terms of several ellipsoidal pockets, although it was recognized that much of the data could not be explained in that manner. Alekseevskii and Gaidukov's (1959, 1960) electrical resistivity and magnetoresistivity work suggested that gallium had an open Fermi surface, possibly in the shape of corrugated planes. Reed and Marcus (1962) used a slightly modified single-OPW or nearly free electron (NFE) model (Harrison, 1960) to explain much of their magneto-resistivity and Hall effect data with quite reasonable success. One serious failure of this model, however, was that it predicted pseudo-hexagonal symmetry for a number of features, and this was not observed. Nevertheless, due to a lack of a better model, this NFE model was used as the basis for many experiments soon thereafter using a multitude of techniques. All tended to show that the NFE model was hopelessly inadequate. Among these experiments were the dHvA effect (Condon, 1964-see Reed, 1969; Goldstein and

Foner, 1966), magnetoresistivity (Reed and Marcus, 1963; Munarin, et al, 1968), ultrasonic cyclotron resonance (Roberts, 1961; Lewiner, 1967), acoustic cyclotron resonance (Munarin, 1968), magnetoacoustics (Bezugli, et al, 1965), ultrasonic attenuation (Gurevich, et al, 1961; Shapira, 1964; Shapira and Lax, 1965), cyclotron resonance (Moore, 1966, 1967, 1968), magnetothermal oscillations (Goy, et al, 1967), and dc size effect (Yaqub and Cockran, 1965) to name but a few.

A slightly better model was calculated by Wood (1966) using an APW method. This involved an ad-hoc potential which did not greatly change the energy band structure from that of the modified NFE model, but produced a Fermi surface considerably different from that of the modified NFE model. In particular, it predicted only a single open k_a trajectory rather than the multitude of k_c open trajectories for the modified NFE model. Because of this fact, that a minor change produced great differences, it was recognised that this APW model could not be made accurate enough. Ensuing work on the rf size effect (Fukumoto and Strandberg, 1967; Haberland, et al, 1969), acoustic geometric and acoustic cyclotron resonances (Alquié and Lewiner, 1972), and induced torque (Cook and Datars, 1970a) confirmed this finding.

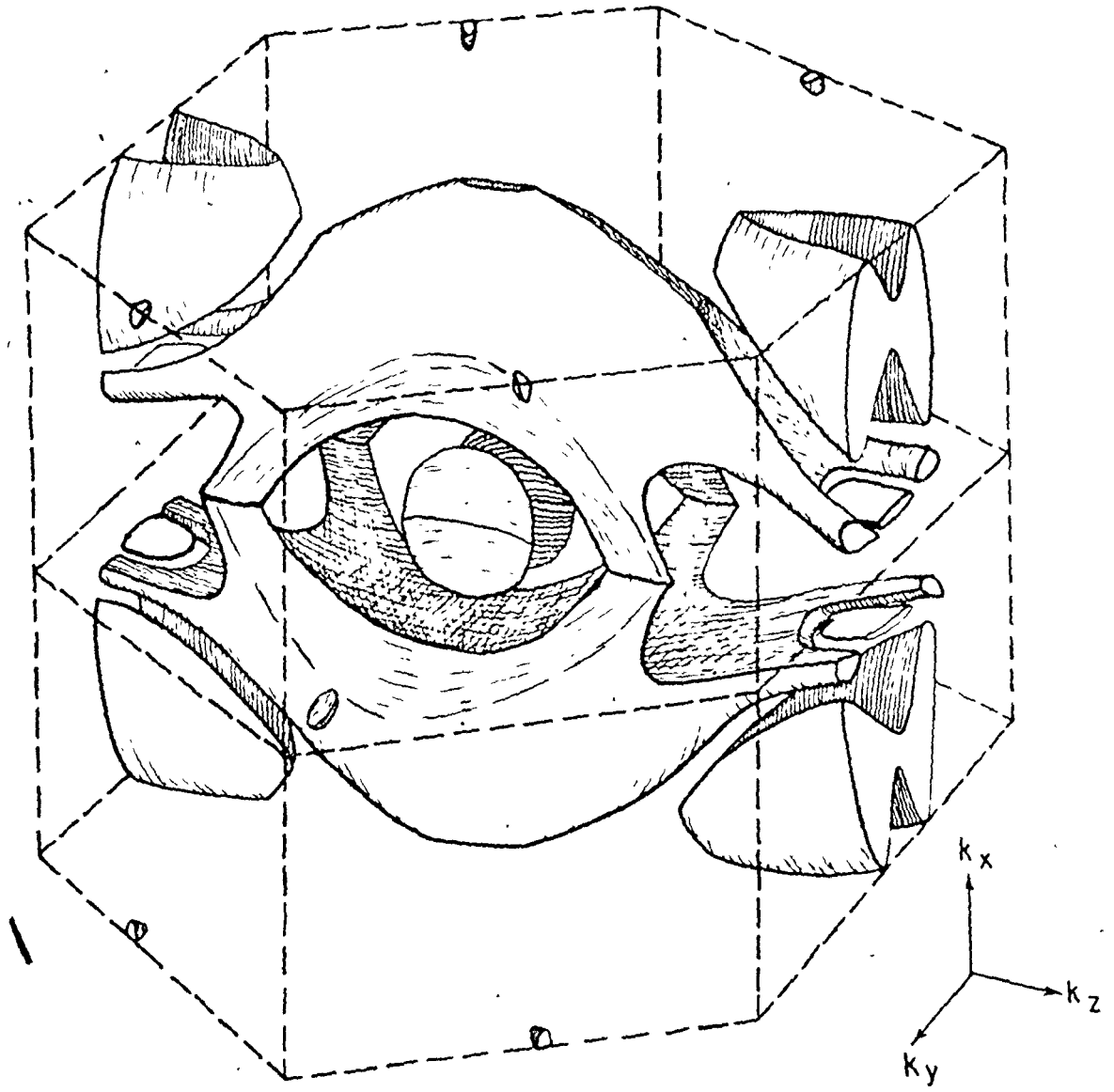
In 1969 Reed published a pseudopotential calculation of the Fermi surface of gallium which employed a local semi-empirical pseudopotential without spin-orbit coupling. The

model Fermi surface resulting from this calculation is described in detail in the next section of this chapter. More recent induced torque experiments (Cook and Datars, 1970a and 1970b) have shown that this model gives the correct open orbit structure, which is a combination of the NFE and APW structures, plus additional orbits, all of which are seen. These findings were confirmed by magnetoresistance measurements (Kimball and Stark, 1970). Measurements of the Gantmakher-Kaner effect in gallium (Gabel and Cochran, 1972) can also be explained by two small parts of Reed's gallium Fermi surface not present in previous models (6h at T and 7e between Arms, in the notation of the next section). Acoustic geometric resonance results (Alquié and Lewiner, 1972) have also been explained by Reed's 6h at T, 5h at X, butterfly and ellipsoid at L, and monster surfaces. The first two of these are not present in earlier models, and the shape of the monster surfaces of the several models are radically different. The fact that Reed's model can be used to explain these several experiments, and previous models fail to explain the data, leads one to believe that the basic features of Reed's model are correct.

D. The Pseudopotential Model for Gallium

The method of calculation used by Reed will not be discussed here, but it lead to the Fermi surface pictured in Figure 4. (This model was constructed by R. J. Douglas, and

Figure 4. A drawing of the Fermi surface of gallium, from a model made by R. J. Douglas based on the calculations of W. A. Reed. All pieces of the model are shown (see text for description) except the seventh-band electron pieces at N. The butterfly pieces should be nearly touching the monster arms, but have been shifted slightly to show the monster.



some minor pieces have been shifted slightly for clarity). The largest piece is the 6th band hole surface, which has a monster in each half zone with four legs touching the $k_x = 0$ plane, two arms touching each of the $k_z = \pm k_c/2$ planes, and a very high concave back touching the $k_x = k_a/2$ plane at X. This piece supports an open orbit along the monster arms in the k_c direction for all magnetic field directions in the ab plane except within 0.1° of the \hat{a} direction (Cook and Datars, 1970a). This exclusion is due to the monster waists at the $k_z = 0$ plane being arched just higher than the highest point on the monster arms in the $k_z = k_c/2$ plane. The monster will also support open orbits in the \hat{a} direction along the monster legs for magnetic fields $31^\circ \pm 3^\circ$ from the \hat{b} direction in the bc plane, thus taking features of both the NFE and APW models. The monster surface is the only part of the gallium Fermi surface capable of supporting open orbits.

The other pieces of the model Fermi surface in approximate order of decreasing size are 1) the 7th-band electron butterfly surface centred at L and oriented with the indentation between the wings parallel to the ac plane; 2) the 8th-band electron ellipsoidal surface (8e at L) inside the butterfly, oriented with its longest axis parallel to the \hat{c} direction; 3) a pair of 7th-band electron saucer surfaces (7e near Γ) displaced slightly from Γ in the \hat{b}

direction, oriented with their major dimensions parallel to the ac plane; 4) a pair of 7th-band electron pancake surfaces between the monster arms (7e between arms) centred at the $k_z = k_c/2$ plane and oriented with major dimensions parallel to the bc plane; 5) a pair of 6th-band hole ellipsoidal surfaces (6h at T) located at $k_y \approx (17/32)k_b$ along the ΓT line oriented with major axis in the b direction; 6) a small 5th-band hole ellipsoidal surface at X (5h at X); 7) small 7th-band electron surfaces in the shape of crossed discs (or a butterfly) at each N point (7e at N, not shown); 8), and small 8th-band electron ellipsoidal surfaces inside the butterfly at N (8e at N). All of these pieces, being closed, will give at least one dHVA frequency at any magnetic field orientation. The same cannot be said of the 6th-band monster hole surface, for although it is the largest piece, it has exceedingly few extremal cross-sections, and even these do not extend over all magnetic field orientations.

It should be noted here that in constructing this model, 6h at T, 7e at N, and 8e at N were essentially "cooked up" in an effort to fit the available data, since these pieces did not appear in the original pseudopotential calculation. The hole surface at T was manufactured by decreasing the Fermi energy 2.5%, and the pieces at N were created by increasing the Fermi energy 4.3%. This sounds rather arbitrary, but the Fermi energy was fixed in the first

instance by matching only the k_z dimension of the surface to the available data, and in the second instance by matching the area for $\bar{H}|\hat{a}$ to the available data. Frequency anisotropies were not pre-determined, and the fact that these "cooked up" pieces have the anisotropy required by the data serves to justify the process. This is roughly equivalent to converting the pseudopotential to a non-local potential for certain regions of the Brillouin zone, and is an admission that this model, also, has its limitations, however good it may be.

There are a number of regions in this model in which the relative proximity of the various pieces gives rise to speculation concerning possible magnetic breakdown (MB). The most obvious region, of course, is within the ellipsoid-butterfly combination at L. These two pieces are degenerate on the $k_x = a/2$ plane. It can be shown (Koster, 1962) that spin-orbit coupling will remove this degeneracy at all points on the face except those points on the line XRL. This creates a small energy gap easily bridged by MB. Similarly, the ellipsoid at X is degenerate with the monster in the same plane, and this degeneracy can also be lifted by spin-orbit coupling, with similar consequences.

Other possibilities for MB are predicted by the model only by proximity arguments. First, the butterfly wings nearly touch the monster arms throughout most of their length, but particularly at the $k_z = c/2$ planes. In this

plane, the pancake surface between the arms also nearly touches the arms, giving rise to the possibility of complicated MB orbits involving the ellipsoid, butterfly, monster, and pancake surfaces for magnetic fields near the \hat{c} direction. There may also be an MB orbit encompassing the monster, the saucer near Γ , and possibly the ellipsoid at X, caused by MB between the monster and the saucer, and the monster and the ellipsoid if necessary.

It should be noted that for magnetic fields near those orientations required for open orbits to occur, one may encounter extended orbits, which are closed orbits requiring more than one Brillouin zone in the extended zone scheme in which to close. These may also give rise to dHvA frequencies under the proper conditions, although the probability of such occurring is small since extremal orbits are required. However, extended orbits formed by MB are much more likely to yield dHvA frequencies.

CHAPTER III

EXPERIMENTAL PROCEDURE and APPARATUS

A. Sample Preparation

A usual procedure for preparing samples, which is not adequate for this study, is to first cut off a small sample of appropriate size from a larger single crystal, and then etch the surface if necessary to remove gross cutting damage. The orientation of the sample is determined using standard back-reflection Laue x-ray techniques, and the crystal is then glued in a $1/8$ " diameter Kel-f plastic rod with the desired axis of the crystal parallel to the rod axis. The rod is then mounted horizontally in a set of modulation and pickup coils (see the next section) having vertical symmetry axis, which are then placed in the vertical bore of a superconducting magnet. The Kel-f rod can then be turned on its axis using a gear reduction arrangement.

This procedure can in principle yield extremely accurately aligned samples, $1/4^\circ$ accuracy being quite common. However, there are two basic drawbacks to this. The first is the fact that the crystal must be cut. Regardless of the method used, some surface damage must occur. Since the dHVA effect is based primarily upon the bulk properties of materials, it is therefore desirable to make

the sample as large as possible, especially if one expects an appreciable amount of surface damage. The size is limited, of course, by the size of the plastic rod, but also by the fact that one must allow sufficient room for glue. This leads to the second basic drawback, namely strain caused by differential contraction between the rod, the glue, and the sample upon cooling from room temperature to 1.2K. Both these effects can severely attenuate the amplitude of high frequency signals from large pieces of the Fermi surface through increased defect scattering. In most common metals, these are usually not severe problems, but they must be considered for gallium since gallium melts at 29.87°C and has a Debye temperature of 325K or about 52°C. At room temperature, therefore, gallium is relatively soft and very susceptible to surface damage. The low melting point and relatively high Debye temperature also indicates that gallium could be susceptible to severe strains due to differential contraction upon cooling if held rigidly at all points, as would be the case if it were glued in place.

For these reasons, the following procedure was adopted, taking advantage of the facts that gallium has a strong tendency to supercool, remaining liquid even at room temperature, and expands approximately 0.3% upon solidifying. First, a seed crystal was obtained by inserting a small wire, previously cooled with liquid nitrogen, into

supercooled liquid gallium. This effectively forced crystallization, but resulted usually in many small crystals adhering to the wire. In approximately one-third of the attempts, a crystal suitably large for the next step was produced. A crystal having a good face was then mounted with its wire on a goniometer and oriented using standard back-reflection Laue X-ray techniques. Symmetry axes were identified 'as defined' by Yaqub and Cochran (1965).

A $\frac{1}{8}$ " Kel-f rod to be used as the sample holder was prepared by first boring a hole as large as possible normal to the rod axis. After careful cleaning, it was mounted rigidly, accurately, horizontal, and normal to, and the proper distance above, a horizontal track onto which the goniometer could be mounted. The rod holder which accomplished this also had a small horizontal channel parallel to the track which intersected the hole in the rod. The rod and the channel were then filled with high purity gallium melt obtained from Johnson, Matthey, & Co, Ltd, and the melt allowed to supercool to room temperature. Upon touching the oriented seed to the supercooled melt, crystallization usually took place in a few minutes and was observable under a microscope. After crystallization the seed was removed with no damage to either the seed or the crystal, and the crystal x-rayed for proper growth both before and after cutting and melting off the channel with a warm razor.

This procedure minimized both the above expected problems by 1) yielding large single crystals, 2) minimizing the surface damage due to cutting, and 3) minimizing strain due to differential contraction by eliminating glue. However, this gain was at the cost of some accuracy in alignment. Although the seed could easily be aligned to $1/4^\circ$ accuracy or better, and the Kel-f rod could be aligned to a few minutes of arc, there was no guarantee that the crystal would propagate and grow in a straight line. Also, the X-raying after crystallization could only be accurate to a few degrees at best, and, of course, it was not possible to re-align a slightly mis-aligned crystal even if it was detectable. The only check possible on accurate alignment, therefore, except for gross errors, was self-consistency of the data.

B.1 Apparatus

The low-frequency field modulation technique was used to detect the dHVA signal. In this system, the crystal is placed inside two concentric coils aligned with axis along the field direction. The outer coil is driven with an ac signal of frequency ω to create a small ac component \bar{h} of magnetic field, which is added to the large dc magnetic field \bar{H} . The emf induced in the inner pickup coil is then determined by the time rate of change of the magnetization vector in the crystal. If one rewrites (19) as

$$\bar{M}(\bar{H}) = \sum_r \bar{A}_r(\bar{H}) \sin \left[2\pi \left(\frac{F_r}{H} - \gamma_r \right) \mp \frac{\pi}{4} \right]$$

where $\bar{A}_r(\bar{H})$ is a vector amplitude of the r^{th} frequency, and the sum on r is over all fundamentals, harmonics, and combinations, then one need only substitute the total field

$$\bar{H}_t = \bar{H} + \bar{h} \sin \omega t$$

for the dc field \bar{H} , and then expand this in terms of h/H for $h \ll H$. It is shown in Appendix A that the result for this configuration is

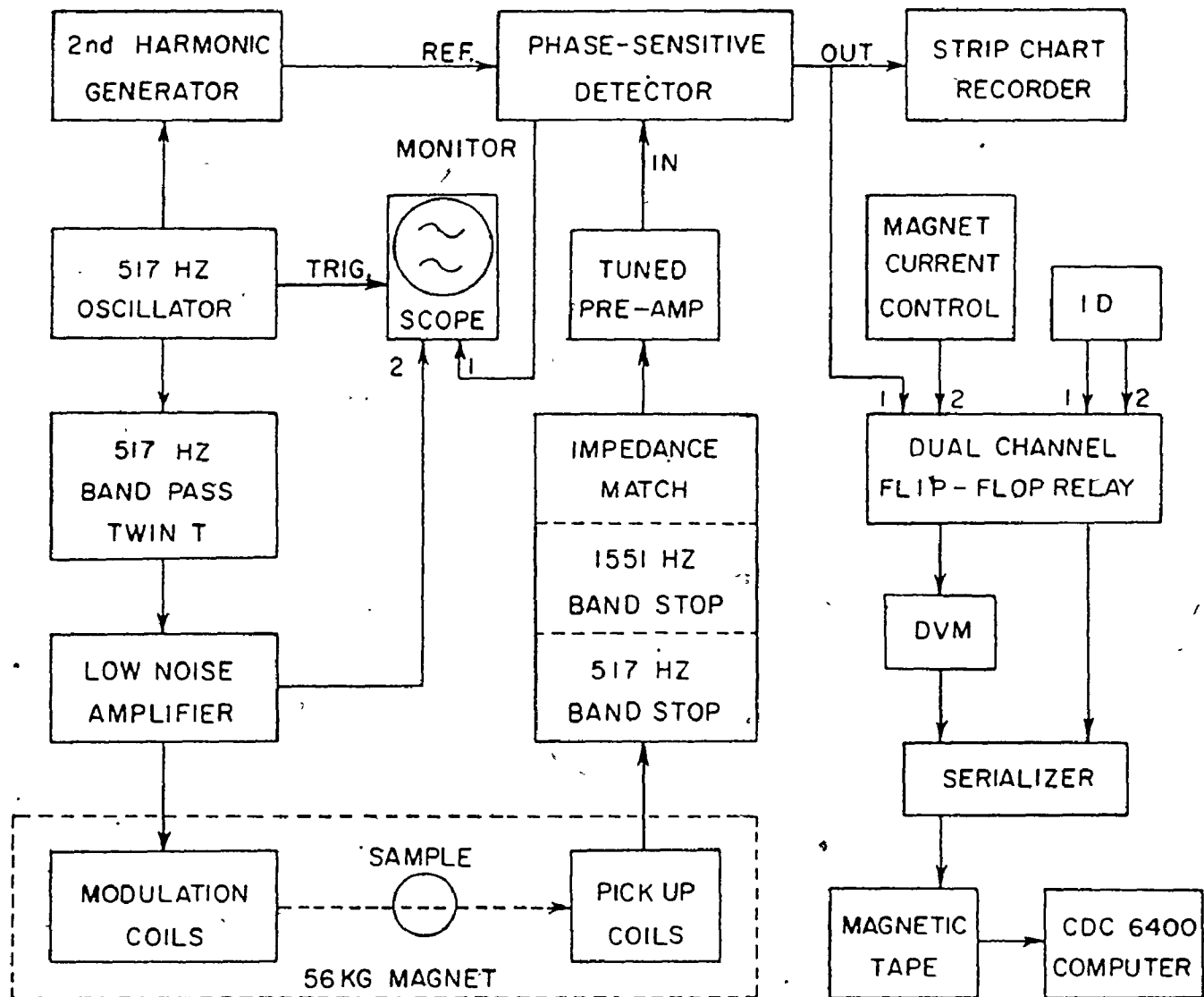
$$(21) \quad \frac{d}{dt} \bar{M} = \sum_r \bar{A}_r(\bar{H}) \sum_{n=1}^{\infty} 2n\omega J_n \left(2\pi F_r \frac{h}{H^2} \right) \sin \left(n\omega t + n\frac{\pi}{2} \right) \\ \times \sin \left[2\pi \left(\frac{F_r}{H} - \gamma_r \right) \mp \frac{\pi}{4} + \frac{n\pi}{2} \right]$$

where $J_n(x)$ is the n^{th} order Bessel function of the first kind. Thus, the signal in the pickup coils has a high content of harmonics of the applied modulation frequency ω . One need only adjust a phase-sensitive detection system to detect the fundamental modulation frequency ω or one of its harmonics to recover the expression (19), modified by the Bessel function.

Figure 5 shows a block diagram of the electronics used. The 517Hz sine wave generated by the oscillator was filtered, amplified, and applied to the modulation coils. The signal detected by the pickup coils was then passed through two filters to eliminate the modulation frequency

Figure 5. Block diagram of the experimental system.



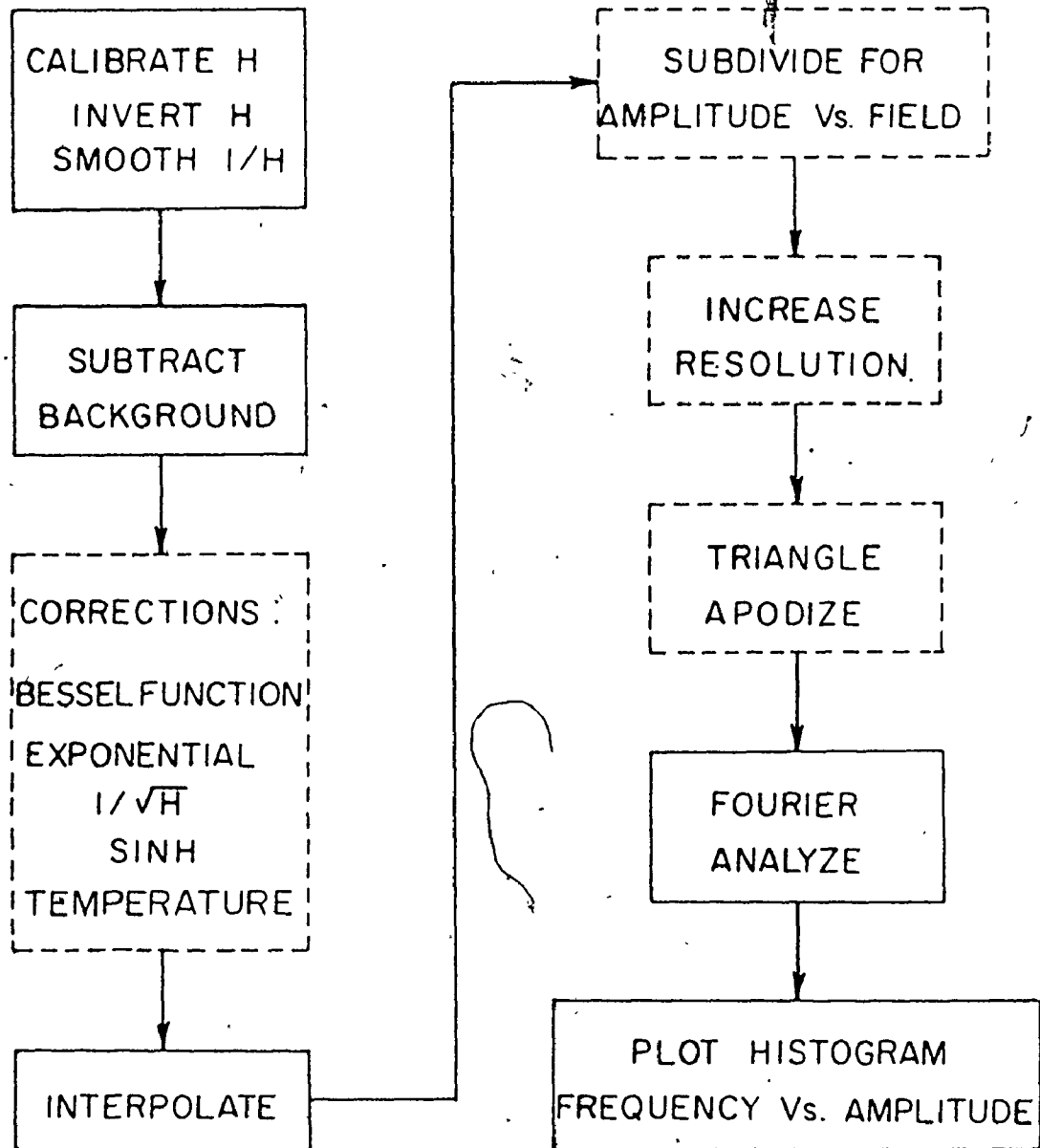


and its third harmonic, impedance matched, fed through a tuned preamp, and applied to the input of a Princeton Applied Research phase sensitive detector (PSD) driven at the second harmonic of the modulation frequency. The modulation current and filtered pickup signal could be monitored on an oscilloscope. The output of the PSD was recorded in parallel on both a strip chart recorder and magnetic tape, the recording on the latter being alternated with a signal proportional to the magnetic field strength. The dc field scanning rate was adjusted so that $|\frac{dH}{dt}| \ll |\frac{dh}{dt}|$ and inverse field usually increased linearly with time.

B.2 Data Analysis

Figure 6 shows a block diagram of the program logic for processing the data tapes. Solid lines are mandatory, while dotted blocks are optional. First, the field signal was calibrated, inverted for a signal reading directly in inverse Tesla (100T = 1MG), and smoothed slightly to correct for analog-digital conversion errors and slight timing errors in data acquisition. The data was then corrected by subtracting any background signal from the dHvA signal, using a parabolic fitting procedure. Optional corrections could then be applied to the data, if desired, to allow for the Bessel function (provided only a single dHvA frequency was present, which was rare), the exponential term, the $1/\sqrt{H}$ factor (which appears in the denominator due

Figure 6. Block diagram of the data analysis program. Solid blocks are mandatory, while dotted blocks are optional.



to the $1/H$ factor in X_r), the hyperbolic sine term, and the temperature variation of the amplitude in (21). (These corrections were built into the program at the user's option because the later Fourier analysis assumed only a linear combination of sinusoidal variations in $1/H$ were present, and any other variations with H would only give a false broadening of the frequency response.) The data were then interpolated to achieve 2^N evenly spaced data points required for the Fourier transform algorithm, and the original data points discarded. Typical data runs were approximately 12 or 22 minutes long, yielding 2000 or 3500 data points, so that $N = 11$ or $N = 12$ was normal. Three more options were now possible. First, the data could be divided into 2^k ($k \leq 3$ usually) equal size blocks for purposes of analysing the frequency amplitude vs. field. This could be expected to show marked changes if magnetic breakdown were present. Second, for signals having a very limited range in field, one could pad the end of the data with an equal number of zeros. This increased the resolution, since it appeared to the program as if signals existed over a wider range of field, but the cost was decreased amplitude of each Fourier component, and a slight broadening of each peak of the spectrum, as well as a slight relative increase in noise content. Last one could apodize what remains of the data with a triangular window envelope function (as

opposed to the implicit rectangular window employed without invoking this correction) to decrease the amplitude of side bands. Side bands are created in the Fourier transform by the mere fact that one samples the dHvA signal between two finite limits, rather than between infinite limits. When this truncated signal is Fourier transformed, therefore, one obtains not the pure Fourier transform of the signal, but the Fourier transform of the signal convoluted with the Fourier transform of a square wave pulse whose width in $1/H$ is just the difference in inverse field used in acquiring the data. These side bands are reduced if the signal is made to go to zero smoothly at both ends of the sampling range. This last option was rarely used, however, as it usually had little effect, it did not help in distinguishing between fundamental and non-fundamental frequencies, and it was very difficult to decide whether a peak known not to be a fundamental was in fact a side band or a combination frequency involving two frequencies of different orders of magnitude. (The choice was immaterial in this last instance since all such were eventually discarded anyway after being identified as non-fundamental.) Finally, the remaining data were Fourier analyzed, and a histogram plotted of frequency vs. amplitude.

B.3 dHvA Frequency-Radii Inversion

Having obtained the dHvA frequencies as a function

of angle, it was possible for some of the frequency branches to convert the frequencies to cross-sectional areas (0.00955\AA^{-2} corresponding to IMG) and invert these areas to obtain the radii of the various Fermi surface pieces. The scheme used here, following the method of Mueller (1961), was to first expand the areas in terms of spherical harmonics

$$A(\bar{\xi}) = \sum_{\ell m} a_{\ell m} Y_{\ell}^m(\bar{\xi})$$

and simultaneously expand the square of the radius similarly

$$\rho^2(\bar{\epsilon}) = \sum_{\ell' m'} b_{\ell' m'} Y_{\ell'}^{m'}(\bar{\epsilon})$$

where $\bar{\xi}$ and $\bar{\epsilon}$ are directions in three dimensions. The coefficients $a_{\ell m}$ are fit from the data by a least square technique, and the problem is to find the coefficients $b_{\ell m}$. The two expansions are related by

$$A(\bar{\xi}) = \frac{1}{2} \int \rho^2(\bar{\epsilon}) \delta(\bar{\epsilon} \cdot \bar{\xi}) d\Omega(\epsilon),$$

the delta function ensuring that $\bar{\epsilon}$ and $\bar{\xi}$ are perpendicular.

If ϕ_L is a complete set of orthonormal functions, then

$$\delta(\rho) = \sum_L \phi_L(0) \phi_L(\rho) \quad \dots$$

Choosing ϕ_L as the normalized Legendre polynomial $\sqrt{L+1/2} P_L$, and expanding the Legendre polynomial in terms of spherical harmonics, one obtains

$$P_L(\bar{\epsilon} \cdot \bar{\xi}) = \frac{4\pi}{2L+1} \sum_{m=-L}^L Y_L^m(\bar{\epsilon})^* Y_L^m(\bar{\xi}) \quad .$$

Therefore:

$$\delta(\bar{\epsilon} \cdot \bar{\xi}) = 2\pi \sum_{Lm} P_L(0) Y_L^m(\bar{\epsilon})^* Y_L^m(\bar{\xi})$$

Integrating,

$$\sum_{\ell m} a_{\ell m} Y_{\ell}^m(\bar{\xi}) = \pi \sum_{\ell m} b_{\ell m} P_{\ell}(0) Y_{\ell}^m(\bar{\xi})$$

Equating coefficients,

$$(22) \quad b_{\ell m} = a_{\ell m} / \pi P_{\ell}(0)$$

The restrictions on this scheme are that the surface must be closed with a centre of inversion symmetry (since $P_L(0) = 0$ for L odd), and the radius vector of the surface from the point of inversion symmetry must be single valued in all directions. This implies that the extremal area measured in the dHvA experiment must also be a central cross-section. Therefore this inversion method will not be successful if a piece of Fermi surface has a non-central extremal cross-section.

There is one further problem with this inversion scheme, which is, to put it bluntly, it will not work for a surface as simple as an ellipsoid. However, it can be made to work, and the method for doing so can be seen in the reason for its failure. Suppose one has an ellipsoid given by

$$\left(\frac{x}{a}\right)^2 + \left(\frac{y}{b}\right)^2 + \left(\frac{z}{c}\right)^2 = 1 \quad (a \neq b \neq c)$$

Then the square of the radius is:

$$r^2 = \beta^2 x^2 + \eta^2 z^2 + b^2$$

where,

$$\beta^2 = 1 - \left(\frac{b}{a}\right)^2$$

$$\eta^2 = 1 - \left(\frac{b}{c}\right)^2$$

Converting to spherical co-ordinates and inverting, one has:

$$r^{-2} = \frac{1}{b^2} [1 - \beta^2 \sin^2 \theta \cos^2 \phi - \eta^2 \cos^2 \theta]$$

This is exact. If it is now inverted to obtain r^2 , one obtains an infinite series, which cannot be terminated by substituting appropriate spherical harmonics for the trigonometric functions. The only case for which this series terminates is that in which $\beta = \eta = 0$; i.e. a perfect sphere. Therefore, before applying the above inversion scheme to the data, one applies a spherical transform by scaling two axes appropriately. This, of course, changes all angles, radii, and cross-sectional areas. A perfect ellipsoidal Fermi surface would then have one term in its spherical harmonic expansion. Additional terms in the expansion would thus indicate departure from an ellipsoidal surface.

Following the method of Ketterson and Windmiller

(1970), one transforms the ellipsoid into a sphere by applying the transform T defined by:

$$\begin{aligned} x' &= \alpha x & \alpha &= \frac{b}{a} \\ y' &= y \\ z' &= \gamma z & \gamma &= \frac{b}{c} \end{aligned}$$

In compact notation, one may write $T(x, y, z) = (x', y', z')$.

One may also formally write its inverse $T^{-1}(x', y', z') =$

(x, y, z) , which is achieved practically by inverting α and γ in the following development. In spherical polar co-

ordinates one would have $T(r, \theta, \phi) = (r', \theta', \phi')$ and

$T^{-1}(r', \theta', \phi') = (r, \theta, \phi)$. It is easily shown that the

relations between transformed and untransformed angles and radii are given by:

$$\begin{aligned} \tan \phi' &= \frac{1}{\alpha} \tan \phi \\ (23) \quad \tan \theta' &= \frac{1}{\gamma} [\sin^2 \phi + \alpha^2 \cos^2 \phi]^{1/2} \tan \theta \\ r'^2(\theta', \phi') &= [\sin^2 \theta (\sin^2 \phi + \alpha^2 \cos^2 \phi) + \gamma^2 \cos^2 \theta] \\ &\quad \times r^2(\theta, \phi) \end{aligned}$$

It is considerably more difficult (Lifsnitz and Pogorelov, 1954) to show that the transformed and untransformed areas are related by:

$$(24) \quad A'(T^{-1}\theta, T^{-1}\phi) = \alpha\gamma [\sin^2 \theta (\sin^2 \phi + \frac{1}{\alpha^2} \cos^2 \phi) + \frac{1}{\gamma^2} \cos^2 \theta]^{1/2} A(\theta, \phi)$$

Note that one uses here an inverse transform for the angles, rather than a transform. This is due to the fact that the direction associated with a plane (the plane of the cross-sectional area) is normal to that plane, so that when one transforms co-ordinates to, say, shrink the x dimensions, a vector pointing in the direction of the normal would be transformed into a vector which is farther from the x axis, whereas the direction of the normal itself would be transformed to a vector closer to the x axis.

The procedure one follows, therefore, in inverting the dHVA frequency data to obtain Fermi surface radii is to

- 1) apply a transform to the data areas using (24), and an inverse transform to the corresponding data angles using (23);
- 2) use these values in a least-square fitting procedure to find the coefficients $a_{\ell m}$, and convert these area expansion coefficients to radius-squared expansion coefficients using (22);
- 3) apply a transform to the original data angles, and using these values in the spherical harmonics, along with the coefficients $b_{\ell m}$, compute $r^{-2}(\theta', \phi')$ in the transformed system;
- 4) finally, apply an inverse transform to r^{-2} , using (23), to obtain r^2 .

CHAPTER IV
EXPERIMENTAL RESULTS

Data were collected for magnetic fields in the three principle planes of gallium. The angular mesh was approximately 2.8° for each of the three planes except where a mesh of 1.1° was required for certain frequency branches near symmetry axes. For each orientation selected, data were taken for several dc field sweep ranges and speeds to enhance various frequency branches. The lowest frequencies encountered were generally obtained with a sweep range of approximately 2kG to 0.35kG, although the upper limit in some cases was reduced to approximately 1.4kG, or raised to as much as 3.0kG, and the lower limit ranged between 0.25kG and 0.46kG. The sweep speed for this range was usually set at the maximum available for a $1/H$ sweep (i.e. inverse field being linear in time), and the PSD time constant raised sufficiently (typically 300ms) to ignore the residual high frequency response. A typical run lasted approximately 12 minutes. For some regions of the ab plane, it was necessary to both lower the upper field limit and raise the lower field limit, and in this case the sweep speed had to be reduced simply to acquire enough data on the tape. Unfortunately this allowed more of the higher frequencies

to pass through the PSD time constant filter as noise, necessitating a compromise.

The highest frequencies observed were obtained with the magnetic field in the range 56kG (the upper limit of our Westinghouse superconducting magnet) to approximately 2.0kG or 3.0kG, depending upon crystal orientation, magnetic field sweep speed, modulation field strength, and the sensitivity of the PSD. Intermediate frequencies were generally observed at the high field end of the lower range or the low field end of the high range. The usual procedure therefore was to begin at the highest available field with a slow $1/H$ field sweep, with the field sweep speed adjusted so that the data acquisition system could be expected to detect the highest frequency evident on the strip chart recorder. The PSD time constant was usually 100mS, but occasionally was raised to 300mS for exceptionally noisy signals. The field then decreased for approximately 22 minutes until the data storage limit of the acquisition system and the dHVA program was reached. This usually resulted in the field reaching $3 \pm .5$ kG, except for the field near the b axis where exceptionally high frequencies were observed. Here the field reached only 4-4.5kG, and a second scan was initiated as above at approximately 4.5kG. Upon completing these one or two scans, the field sweep speed and the modulation field strength were adjusted to enhance

the intermediate frequencies, and the sweep resumed for another 12 or 22 minutes. Adjusting the modulation field strength also necessitated adjusting the dc field strength to minimize the attenuation from the Bessel function. The modulation field strength was usually set at approximately 16G, but was generally doubled to enhance the intermediate frequencies. For the high and low frequencies, the argument of the Bessel function ranged between near zero and some value less than (for high frequencies) or slightly greater than (for low frequencies) 5.136 , at which point the Bessel function has its first zero. The intermediate frequencies were generally detected for the argument of the Bessel function between the first zero and the second (8.417) or third (11.620). Observation of these zeros enabled us to calibrate the modulation coil. However, unambiguous observation of these zeros was not as common as this might lead one to believe since it required that only a single frequency be the dominant signal, all other frequencies being minimal. Usually, but not always, in passing through a Bessel zero of one frequency, a secondary frequency was quite visible; and the exact position of the zero was not obvious. This zero would then appear to the Fourier analysis algorithm as a beat frequency, which would generate a false frequency in the frequency spectrum histogram.

The data obtained is shown in Figures 7 and 8, and is also tabulated in Appendix C. Figure 7 shows the low frequencies and Figure 8 shows the high frequencies. For comparison, the highest frequency of 1.5MG on Figure 7 is also shown on Figure 8. Frequency branches are labeled A_n , B_n , or C_n where n is a number from 1 to 20, 22 or 21 respectively. In general, high values of n correlate with higher frequencies. With one exception on Figure 7 (to be discussed later) only fundamental frequencies are shown here, the harmonics and combinations, as well as those false frequencies generated by Bessel zeros, being suppressed. In some cases (e.g. C_7 and A_6 for the magnetic field near the b axis) harmonics as high as the ninth harmonic were clearly visible in the Fourier spectrum.

It can be seen that some branches can be traced through all three planes, while others were not observed for some orientations. These figures (7 and 8) cannot show whether these discontinuous branches ended abruptly as a function of angle, or merely faded. Similarly, these figures cannot show the relative strengths of the various frequencies for each orientation. It is also not possible to read these figures to more than two figure accuracy. The table in Appendix C is designed to correct these problems. Every observation has been listed in these tables, along with an approximate indication of the frequency amplitude. (Some




Figure 7. dHvA frequencies up to 1.5MG for the
three principle planes of gallium.

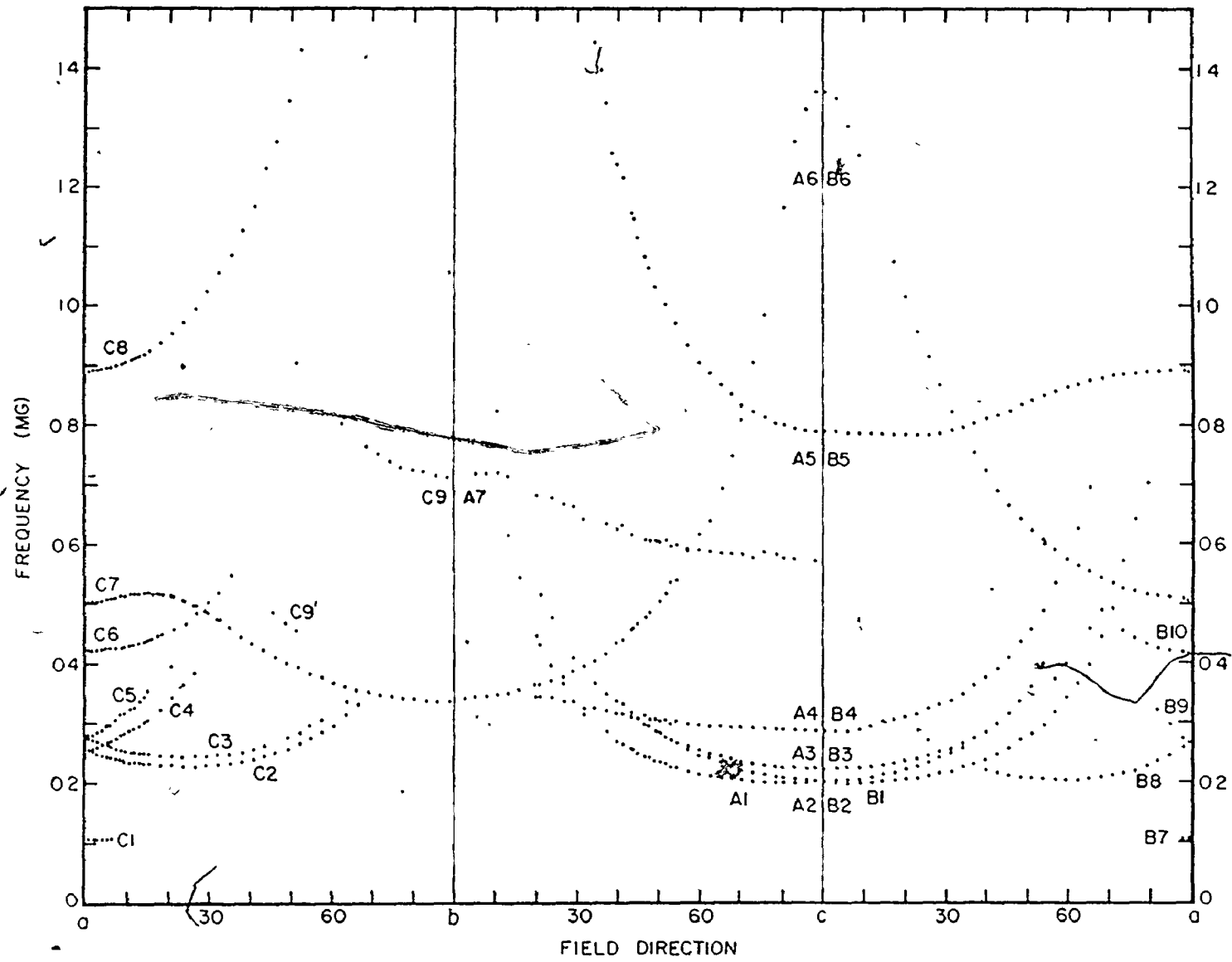
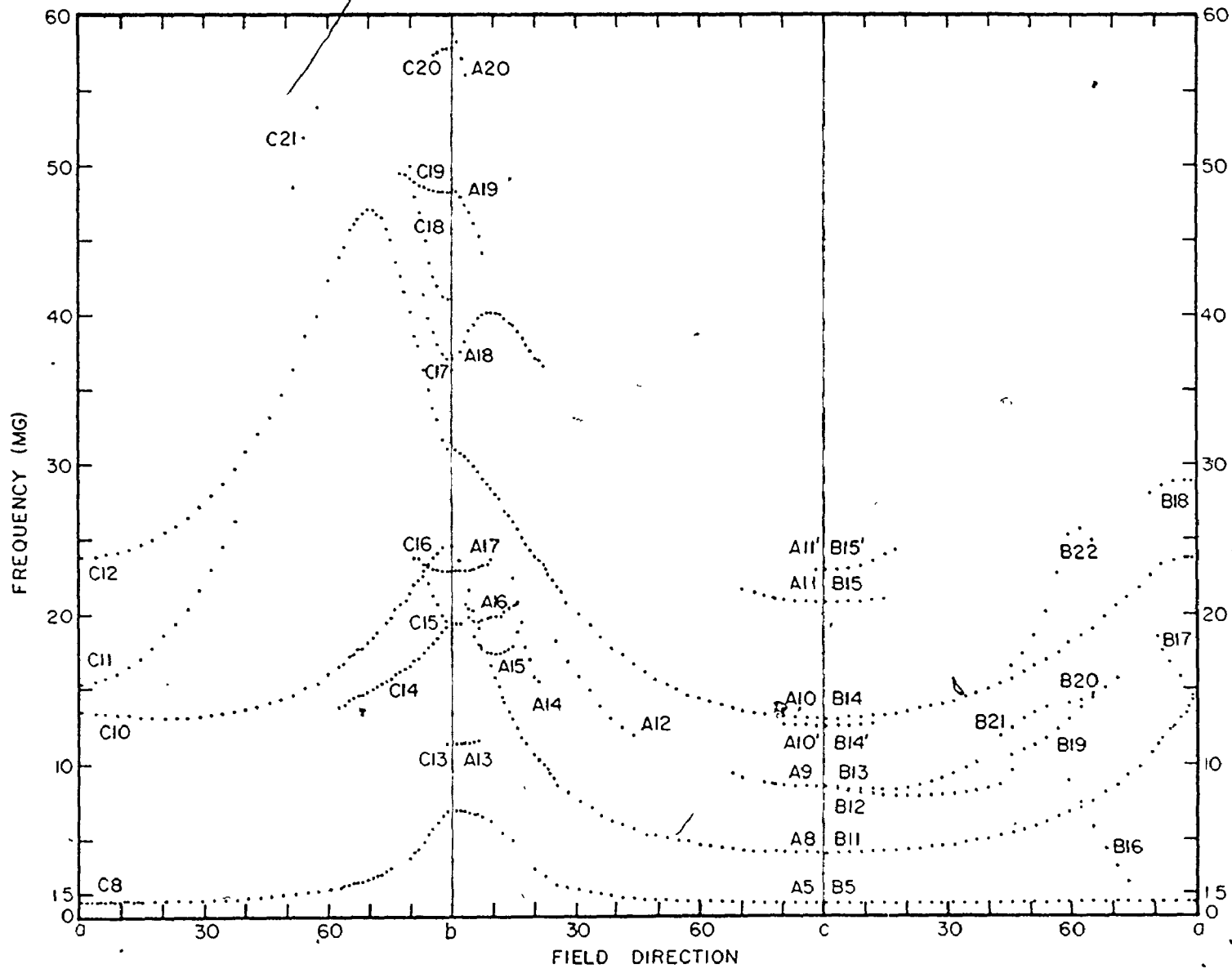


Figure 8. dHvA frequencies between 1.5MG and
60MG for the three principle planes
of gallium.



observations were, of necessity, left off Figures 7 and 8 and ensuing figures.) All amplitudes were normalized to the amplitude of the strongest frequency at each orientation for each condition of field sweep range and speed and modulation field strength. D indicates a frequency was dominant or had an amplitude at least 90% of that of the dominant frequency, S indicates a strong frequency (25%-90%), M indicates a medium strength (3%-25%), and W indicates a weak signal (less than 3%). The noise level varied between 0.2% and 1% of the dominant signal, depending on a variety of conditions. These figures are not as unrealistically low as they might sound since the histogram output of the analysis plotted frequency vs. the square root of the relative signal strength, thus enhancing the weaker signals. On a maximum scale of 50, the demarcation lines thus occurred at 48, 25, and 9, with the noise level being 2 to 5. The error limits shown at the top of each column will be discussed later.

An entry of the table being blank does not necessarily mean that the frequency branch in question was not observable at that orientation, although that is usually the case. It could also mean that the frequency was not looked for, or that the frequency was observed but not with sufficient accuracy to warrant inclusion, as might occur for weak signals buried in noise. In most cases, the correct reason should be obvious from the context.

During the course of the experiment it was necessary many times to remove the sample with its sample holder rod (see Chapter III A) from the dHvA apparatus and remount it at a later time, thus necessitating an overlap of data for purposes of calibrating the angle of rotation with previous data. This calibration was done by matching the most rapidly varying frequencies in the region of overlap. This did not always result in a perfect match if two frequencies were both varying rapidly as a function of angle (e.g. A5 and A6 in the vicinity of 50° from b toward c).

As noted in Chapter III A, the only check on accurate alignment was self-consistency of the data. It can be seen from Figures 7 and 8 and Appendix C that alignments were reasonable but slightly off in some cases, since for most cases the data in the three planes match reasonably well at the symmetry axes. It will be shown that for an accurately aligned crystal, C10 and C11 should meet at the frequency at which B11 and B17 cross for the magnetic field in the \hat{a} direction. By matching the measured frequencies of C10 and C11 for the magnetic field in the nominal \hat{a} direction to B11 and B17, it can be calculated that for the ab plane crystal, the orientation in the nominal \hat{a} direction was actually 2.2° toward \hat{c} from \hat{a} . Similarly, by comparing A10 and C12, it was calculated that for the bc plane, the orientation at \hat{b} was actually 0.6° toward \hat{a} . No other

inconsistencies in orientation were found. By comparison, the most recent set of gallium data (Griessen, et al, 1974) quotes errors in orientation of up to 3.5° .

The above orientation error was the only error occurring which was of a correctable nature. Other errors occurring pertained to limits of resolution or were otherwise non-correctable. The simplest error source, of course, was the Fourier transform resolution, which was a function of the inverse field spanned in collecting data on the tape. For the low frequencies, this resolution was approximately $\pm 0.0008\text{MG}$, and for the intermediate and high frequencies it was $\pm 0.02\text{MG}$.

Another easily recognizable error source was the angular resolution of the sample turning mechanism. This employed a 32:1 gear reduction ratio, and the estimated accuracy in turning that part of the mechanism outside the magnet was approximately $\pm 5^\circ$, primarily due to an occasional slight stickiness in turning. Angular resolution at the sample was therefore $\pm 0.16^\circ$.

One might suppose that another source of error could be due to the method of sample preparation without glue. Haberland, et al (1969), calculated that the linear thermal contraction of gallium between room temperature and 4K is approximately 0.5% in all directions. This is approximately the same as the thermal contraction of the Kel-f holder. But, if they are not identical and the Kel-f holder contracts

less than gallium, there may be some "rattle" or rotation in the sample position, or if the holder contracts more, there could be some slight pressure between the holder and the sample, serving to hold the crystal more rigidly. The latter situation is desirable, but since thermal contraction data for Kel-f accurate at 4K was not available, this situation could not be guaranteed. In actual fact, the relative contraction was immaterial since a design feature of the holder prevented rattling and rotation if the gallium contracted slightly more than the Kel-f. During the process of cleaning the holder preparatory to filling it, the sharp edges of the hole in the holder were trimmed slightly. This trimming was not regular. Upon filling the holder with gallium melt and allowing it to crystallize, the gallium also filled this trimmed volume, resulting in a slightly larger radius at both ends of the cylindrical sample. Then, if gallium contracts slightly more than Kel-f, these irregular bulges would secure the sample rigidly to the holder, preventing both rattle and rotation.

There are several additional possible sources of error when considering the field applied to the sample. An independent NMR calibration of our magnet showed that the field in tesla at the centre of the magnet was 1.0056 ± 0.0002 times the applied voltage. But it also showed that the field was not completely uniform throughout the magnet bore. It is estimated that this could contribute a field calibration error

of up to 0.02%, depending on the exact sample position. For the low frequencies encountered, this error is negligible compared to the Fourier transform resolution. However, for the high frequencies, it could be as much as half the Fourier transform resolution. This field calibration is also applicable only to an essentially empty magnet bore. The sample itself will disturb this field. If there are ac components added to the field one must also consider the sample skin depth, since the ac field will not penetrate completely. For the 517Hz ac component used here, this is not a serious problem, but there will still not be 100% penetration. The field will therefore not be uniform throughout the sample. This non-uniformity leads to a slight broadening of each peak of the Fourier transform, but it does not otherwise alter the Fourier transform. In particular, the positions of the peaks are not changed. There is, however, another source of error which does shift these peaks, and that is the fact that inside the metal the field one should use is $\bar{B} = \bar{H} + 4\pi\bar{M}$, rather than \bar{H} . As stated previously, this does not change the dHVA frequencies, since those are a property of the metal, but it does change the field calibration. This calibration change must then shift the positions of the Fourier spectrum peaks. Since this problem is expected to be more serious at higher fields, the field calibration must become field dependent. If the problem is occurring, the proof one observes is an enhance-

ment of the harmonic and combination frequencies. Although such frequencies were observed in the low field, low frequency scans, they were not significant, but they were significant when investigating the high and intermediate frequencies.

It is therefore estimated that one must take this feature into account for frequencies above approximately 1 - 1.5MG, where it could result in an error of a significant fraction of 1%. This being the largest error, error limits of the high and intermediate frequencies are therefore estimated at approximately $\pm 0.1\text{MG}$ and $\pm 0.06\text{MG}$ respectively, and the error limits of the low frequencies are set at the Fourier transform resolution of $\pm 0.0008\text{MG}$.

The lowest frequencies also have another problem peculiar to them, and that is the fact that there are very few Landau levels contained in the pieces causing these frequencies. As an example, C7 and A6 at 0.335MG for $\hat{H}|\hat{b}$ were observed for fields below 20kG, which gives $n \approx F/H \gtrsim 17$. Further, the A1-3 and B1-3 complex near \hat{c} was observed for fields below approximately 15kG, which gives $n \gtrsim 13$. Clearly, this is far too low to make the single-term expansion in equation (15) valid, and one must therefore include higher terms. However, it has been shown that including such terms does not change the frequencies involved, but merely changes the amplitude of that frequency. This problem of few Landau levels will therefore not contribute to the quoted errors in determining the frequencies, since

one need not use \bar{B} (which includes the amplitude of \bar{M}) in place of \bar{H} for these low frequencies.

CHAPTER V

DISCUSSION

A. Introduction

In discussing and interpreting the results of the previous section, several avenues of approach must be taken. First, it is shown in Appendix B that for ellipsoidal Fermi surfaces, inverse frequency squared is linear in $\cos^2 \theta$. Since Reed's model predicts several ellipsoidal surfaces, this type of analysis (henceforth termed a $1/f^2$ plot) must be done for most frequencies to determine which might be generated by ellipsoidal surfaces. Also, since the $1/f^2$ plots severely distort the positions of the data points shown in Figures 7 and 8, they can also serve to identify which data points belong to which branch in frequency regions such as 20MG for the magnetic field near \hat{b} or 0.2MG for the field near \hat{c} .

Second, one can compare the predicted frequencies of the model with those found in this study. Since the predicted frequencies are only given for the field along symmetry directions, one must then consider how they should change for the field in a non-symmetry direction. If this behaviour is found experimentally, then these frequency branches can be considered to be identified. Included in such considerations, of course, would be the fact that

frequencies generated by such pieces as the monster arms and legs will not exist for all orientations of the magnetic field. For those frequencies generated by Fermi surface pieces having inversion symmetry and only central extremal orbits, one can invert the frequency data to obtain Fermi surface radii as explained in section IV B.3.

Using the above procedure, most frequency branches would be identified if Reed's model is correct. Frequency branches remaining to be identified might then be explained by unexpected extremal areas on the monster and/or the ellipsoid-butterfly combination, or by magnetic breakdown. Frequency assignments made by any of the above means are listed in Table 3 at the end of this chapter, and each will be discussed in detail in later sections of this chapter.

All of the above analysis can be based primarily upon the values of the frequencies vs. magnetic field orientation, with a small consideration given to frequency amplitudes in those cases where a frequency branch fades or otherwise disappears as a function of angle. Independent of these considerations one may also obtain a slight amount of information concerning effective masses if one finds a frequency branch disappearing at isolated angles due to spin zeroing.

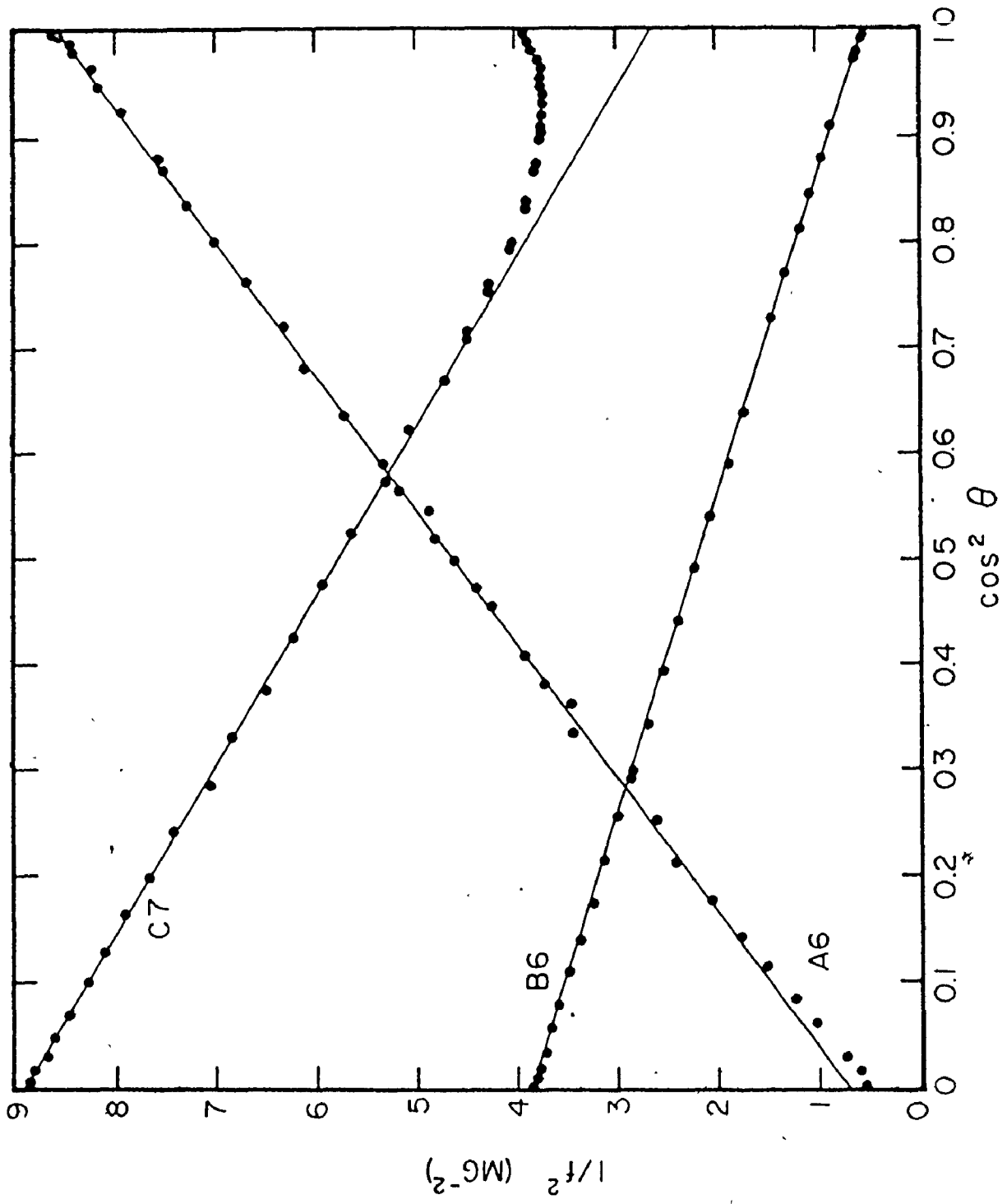
B. Continuous Low Frequencies I

We begin therefore with a consideration of the low

frequency branches shown in Figure 7. The data presented here is more extensive and more precise than that of Griessen, et al (1974), and both sets of data are certainly far more extensive than that of Goy, et al (1967), Goldstein and Foner (1966), or Condon (1964). In those regions that the data can be compared, there is good qualitative agreement, although quantitative agreement is difficult without tabulated values. The interpretation of several frequency branches in these previous works is, however, unfounded, although the cause in most cases can be traced to a lack of sufficient data. It should be noted that the experimental techniques employed by the several researchers were different. The present study uses the dHvA effect aided by digital acquisition and computer processing of the data using standard Fourier analysis methods. Condon employed torsion methods. Goldstein and Foner used the dHvA effect, but did not have access to the present sophisticated techniques; in view of the present data, this hand analysis was remarkably good. Goy, et al, observed magnetothermal oscillations, and Greissen, et al, investigated uniaxial stress dependence.

Figure 9 shows a $1/f^2$ plot for A6, B6, and C7. This shows that the small closed pieces of surface generating these branches is very nearly an ellipsoid but does have marked deviations. Reed's model predicts that 6h at T should generate frequencies of 0.52MG, 0.346MG, and 1.26MG for the

Figure 9. $1/f^2$ plot for A6-B6-C7, attributed
to the sixth-band hole surface at Γ .



magnetic field along \hat{a} , \hat{b} , and \hat{c} respectively. This study shows that the correct frequencies are 0.507MG, 0.335MG, and 1.363MG respectively, the later two being slightly lower than Griessen's values of 0.352MG and 1.38MG. The deviations from ellipticity noted in Figure 9 then correspond to a significant compression near the bc plane, and a smaller bulge near the ab plane. These qualitative estimates are borne out by the results of the expansion and inversion scheme. Table 2 gives the expansion coefficients of a 21 term spherical harmonic least squares approximation to the data of A6-B6-C7. The spherical harmonics chosen were those $Y_{\ell m}$ of even ℓ and even m up to $\ell = 10$. One should not be misled by the small order of magnitude of some of these coefficients since $Y_{\ell m}$ may be compensatingly large for large ℓ and m . Neither should one discount the validity of the expansion merely on the basis that 21 terms were required, since this is not an unreasonably high number of terms; 37 term and 91 term expansions are not unknown (Aurbach, et al, 1970). Figure 10 shows the spherical harmonic expansion for A6-B6-C7 superimposed on the data, showing quite a good fit. The algorithm employed did not allow for calculating the error limits of the coefficients. However, several of the worst fit data points, both for this set of data and for those following, were discarded for purposes of estimating the error. The resulting change in the coefficients occurred in the third to the eighth decimal, depending upon the co-

TABLE 2

Spherical Harmonic Expansion Parameters

Branches	A6-B6-C7	A4-A7-B4-C9-C9'	A3-B3	C10-A8-B11	
Identi- fication	6h at T	7e between arms	5h at X	8e at L	
α	1.5185	4.8037	0.9481	0.5419	
γ	3.8619	0.8115	0.2517	0.1783	
ℓ	m				
0	0	1.95086×10^{-2}	1.73453×10^{-2}	2.01054×10^{-3}	2.02254×10^{-2}
2	0	1.68205×10^{-5}	-4.98339×10^{-3}	1.68100×10^{-6}	1.97853×10^{-4}
	2	-3.17690×10^{-5}	2.87132×10^{-3}	2.49815×10^{-6}	-5.86381×10^{-6}
4	0	4.18062×10^{-4}	8.43011×10^{-4}	8.88164×10^{-7}	9.76349×10^{-4}
	2	-1.55832×10^{-5}	-9.19952×10^{-5}	-4.76767×10^{-7}	-2.56315×10^{-5}
	4	-7.32247×10^{-6}	2.41478×10^{-5}	1.74823×10^{-7}	2.00930×10^{-5}
6	0	-3.16259×10^{-5}	1.29941×10^{-5}		-3.22921×10^{-5}
	2	-3.43013×10^{-6}	2.04641×10^{-6}		-8.35384×10^{-6}
	4	4.25667×10^{-8}	2.97567×10^{-8}		3.15219×10^{-7}
	6	-4.70548×10^{-9}	-2.63319×10^{-9}		-5.10622×10^{-9}
8	0	-1.71998×10^{-4}			-1.30097×10^{-4}
	2	-8.31384×10^{-6}			3.34423×10^{-6}
	4	4.16217×10^{-8}			4.04257×10^{-8}
	6	1.53035×10^{-9}			-1.60905×10^{-9}
	8	-1.03005×10^{-13}			1.15328×10^{-10}

TABLE 2 (cont.)

	6h at T	8e at L
$\frac{\ell}{10} \frac{m}{0}$	1.02415×10^{-4}	1.82065×10^{-4}
2	2.14588×10^{-6}	1.96883×10^{-6}
4	1.39865×10^{-8}	-1.14427×10^{-8}
6	-8.36895×10^{-10}	7.32545×10^{-10}
8	-2.31375×10^{-12}	-2.12752×10^{-11}
10	-5.31151×10^{-15}	2.30105×10^{-13}

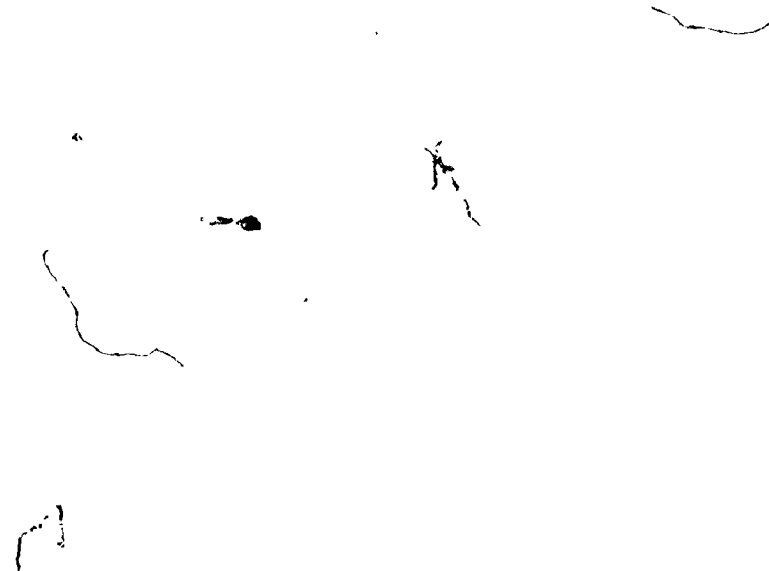
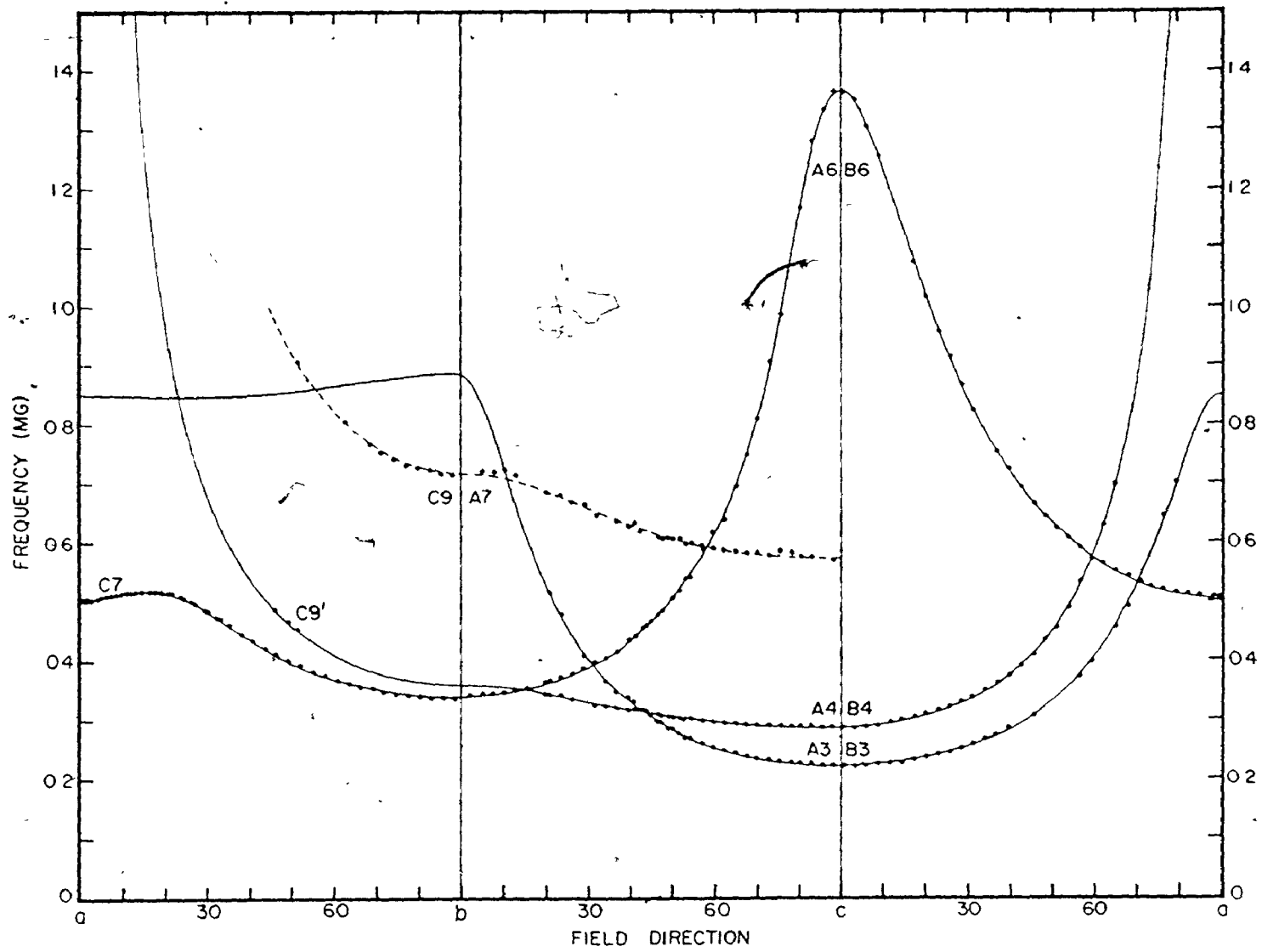


Figure 10. Spherical harmonic expansion of several frequency branches. Points shown are the data of Figure 7 and Appendix C. The solid lines shown are a least-square spherical harmonic expansion fit to these data points using the parameters shown in Table 2. The dotted line shown is the second harmonic of one of these lines.



efficient, but in no case was Figure 10 (or Figures 11 or 12) visibly altered. Also, in an effort to find out if all of the coefficients listed in Table 2 were necessary, some of the smallest were arbitrarily zeroed and the rms error recomputed, using the remaining coefficients. In every case, zeroing only two or three terms made a significant change in the rms error.

Figure 11 shows the results of the inversion scheme for 6h at T. The dotted line shows the radius in the three principle planes of the transformed system (see Chapter IV B.3), the solid line shows the radius in the untransformed system, and the dashed line shows the percentage deviation of the radius from that of the closest fitting ellipsoid. (The latter is on a highly expanded scale.) The closest fitting ellipsoid was defined as the surface obtained using only the first term of the expansion. Figure 12 shows cross-sectional plots of the radius in the three principle planes. Both Figure 11 and Figure 12 show a compression in the \hat{b} direction and a bulge in the \hat{a} direction. The latter could be interpreted as a compression near the \hat{a} direction in the ac plane, but in view of Figure 9 this is not considered a reasonable interpretation. Also, all data was collected in the three principle planes. Inversion schemes of this type work best for a set of data at random, but accurately known, directions encompassing one entire irreducible zone of the surface. Clearly the present data does not satisfy this

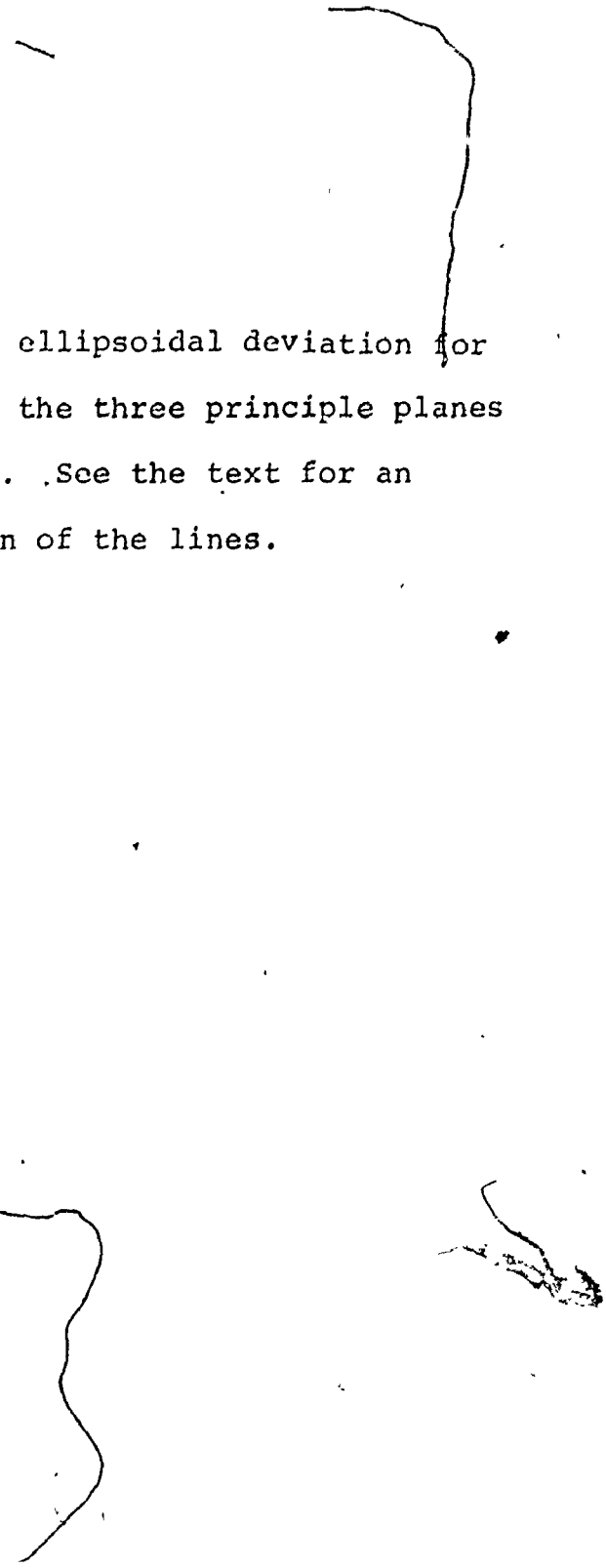


Figure 11. Radius and ellipsoidal deviation for
6h at T in the three principle planes
of gallium. See the text for an
explanation of the lines.

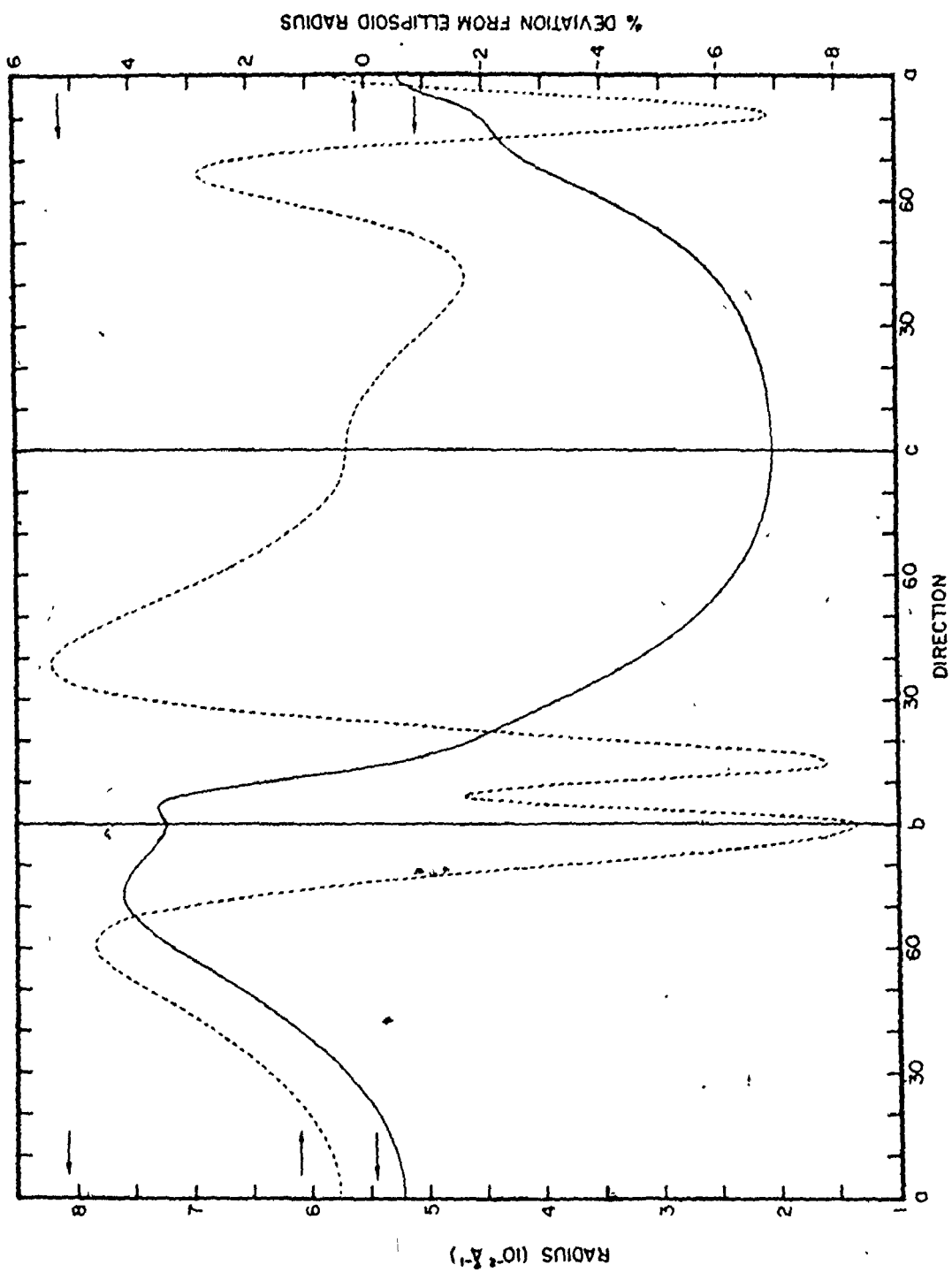
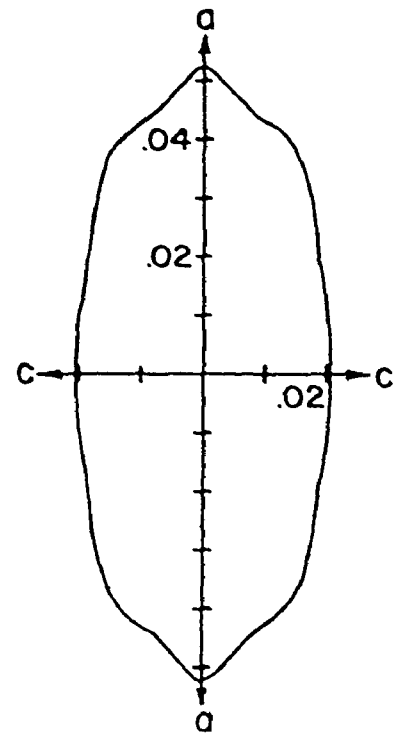
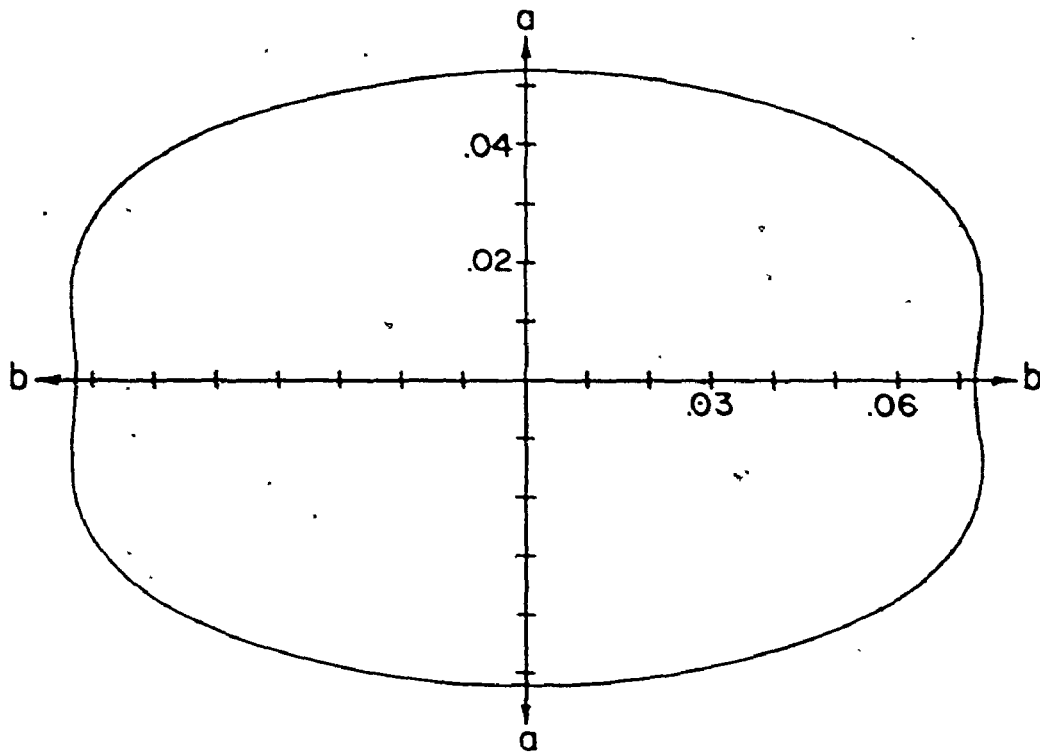
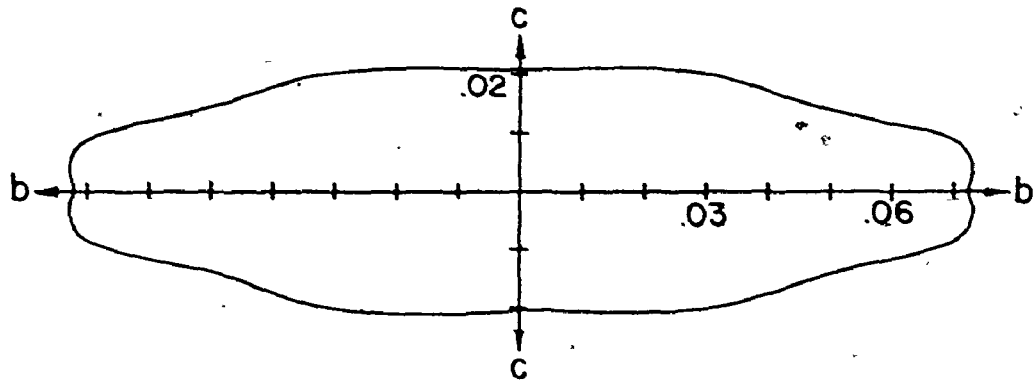


Figure 12. Cross-sectional areas of 6h at T in
the three principle planes of
gallium, as calculated for Figure
11. The scale is in \AA^{-1} .

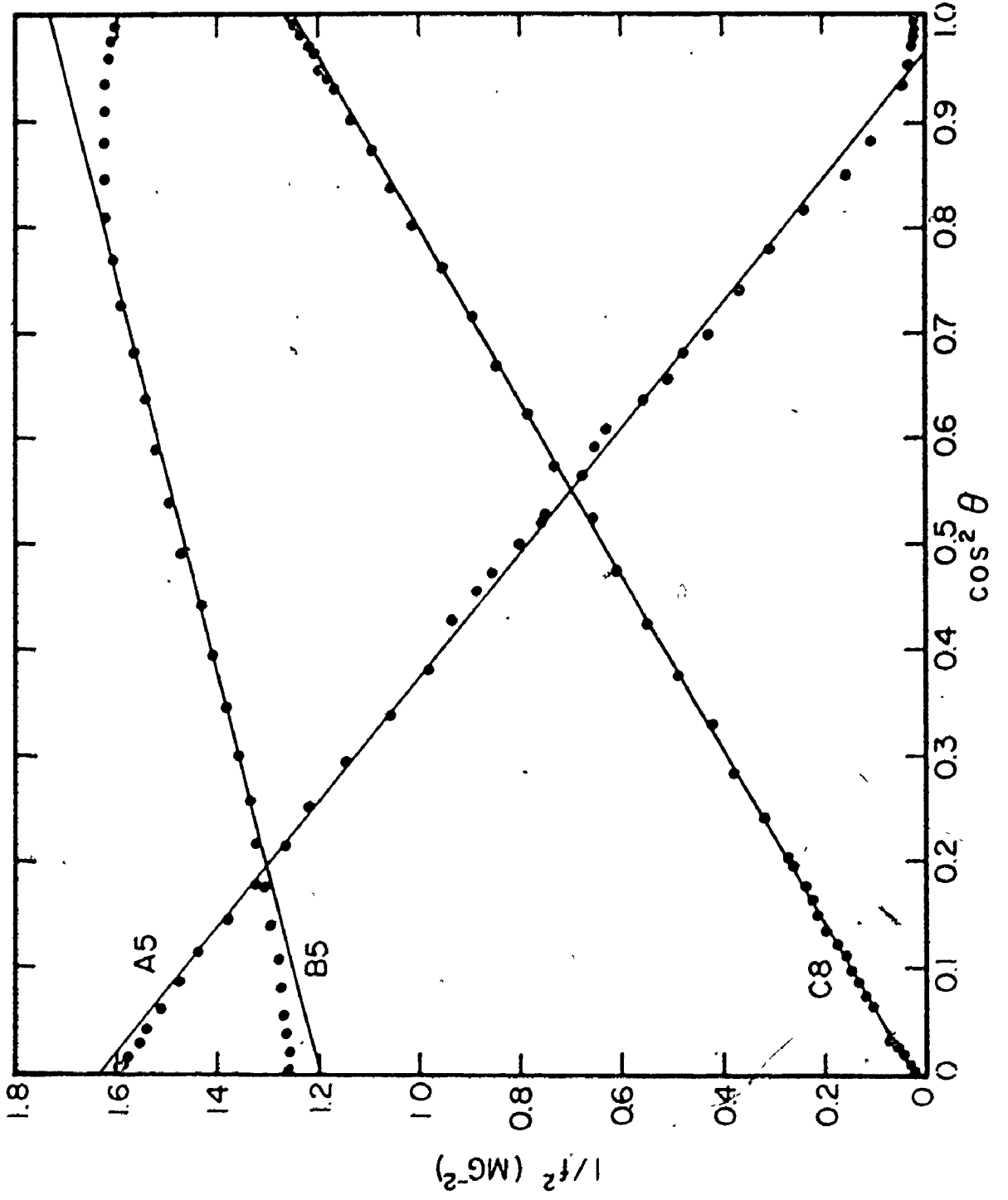


condition, and this leads to inherent instabilities in calculating the spherical harmonic expansion coefficients. It was found that for this surface, it was not possible to fit more than the first 6 terms (all terms up to and including $\ell = 4$) of the expansion without encountering negative square radii and/or unreasonably large expansion coefficients. Therefore, it was decided to fit the data to the first 6 spherical harmonics, and use the remaining 15 terms to reduce the rms error given by the first 6 terms. Here again, an instability was encountered, as it was not possible to include the $\ell = 12$ terms for similar reasons. Therefore, because of the above problems, exact details of Fermi surface shape at non-symmetry directions arising from this study cannot be believed in their entirety. In this particular case there is also the fact that 6h at T does not have inversion symmetry, even though it does have two mirror planes, and the model shows this piece to be nearly symmetric in the third plane. It is valid, however, to believe general trends in the inversion, and it is also possible to be reasonably certain of Fermi surface radii near symmetry directions. As evidence of this, the rf size effect data of Haberland, et al, yield extremal dimensions of approximately 0.022\AA^{-1} and 0.072\AA^{-1} for the \hat{c} and \hat{b} directions, whereas Reed's model yields extremal dimensions of 0.021\AA^{-1} , 0.078\AA^{-1} , and 0.049\AA^{-1} for the \hat{c} , \hat{b} , and \hat{a} directions. The present study gives 0.0205\AA^{-1} , 0.0722\AA^{-1} ,

and 0.0522 \AA^{-1} respectively.

Figure 13 shows a $1/f^2$ plot for C8, A5, and B5. The small closed surface generating these branches is again basically ellipsoidal, but there are much more significant deviations than for 6h at T. A5 shows that an ellipsoidal approximation to this surface would have its maximal cross-sectional area for \hat{H} approximately 10° toward \hat{c} from \hat{b} , since that is the approximate intercept of A5 at $1/f^2 = 0$. C8 does not show a similar deviation from symmetry in the ab plane, whereas B5 shows that the piece has a reasonably uniform cross-sectional area for any plane containing the b axis. This would require a shape which could be described as a nearly circular pancake whose diameter in the \hat{a} direction is pinned to a plane normal to \hat{b} , but whose edges in the \hat{c} direction have been curved off this plane in the same direction approximately 10° toward \hat{b} . This is approximately the shape required for the 7e near Γ saucer of Reed's model, for which dHVA frequencies of 0.704 MG, 6.65 MG, and 0.843 MG would be predicted for the field in the \hat{a} , \hat{b} , and \hat{c} directions respectively. This study gives 0.890 MG, 6.94 MG, and 0.791 MG respectively. This piece is thus considerably wider in the \hat{c} direction and slightly narrower in the \hat{a} direction than the model predicts, with the radius in the \hat{c} direction being greater than that in the \hat{a} direction rather than vice-versa. Since this piece is not expected to have, and in fact does not have, inversion symmetry, the data inversion scheme used here is not applicable. It

Figure 13. $1/f^2$ plot for A5-B5-C8, attributed
to the seventh-band electron surface
near Γ .



should be noted here that this study is the first in which the C8 and A5 branches have been reported in their entirety. Golstein and Foner (1966) and also Goy, et al, (1967), traced these branches up to approximately 2.3MG, whereas Griessen, et al (1974) reported frequencies up to 1.4MG. In all fairness, however, signals above approximately 2.5MG were quite weak in comparison to lower frequencies.

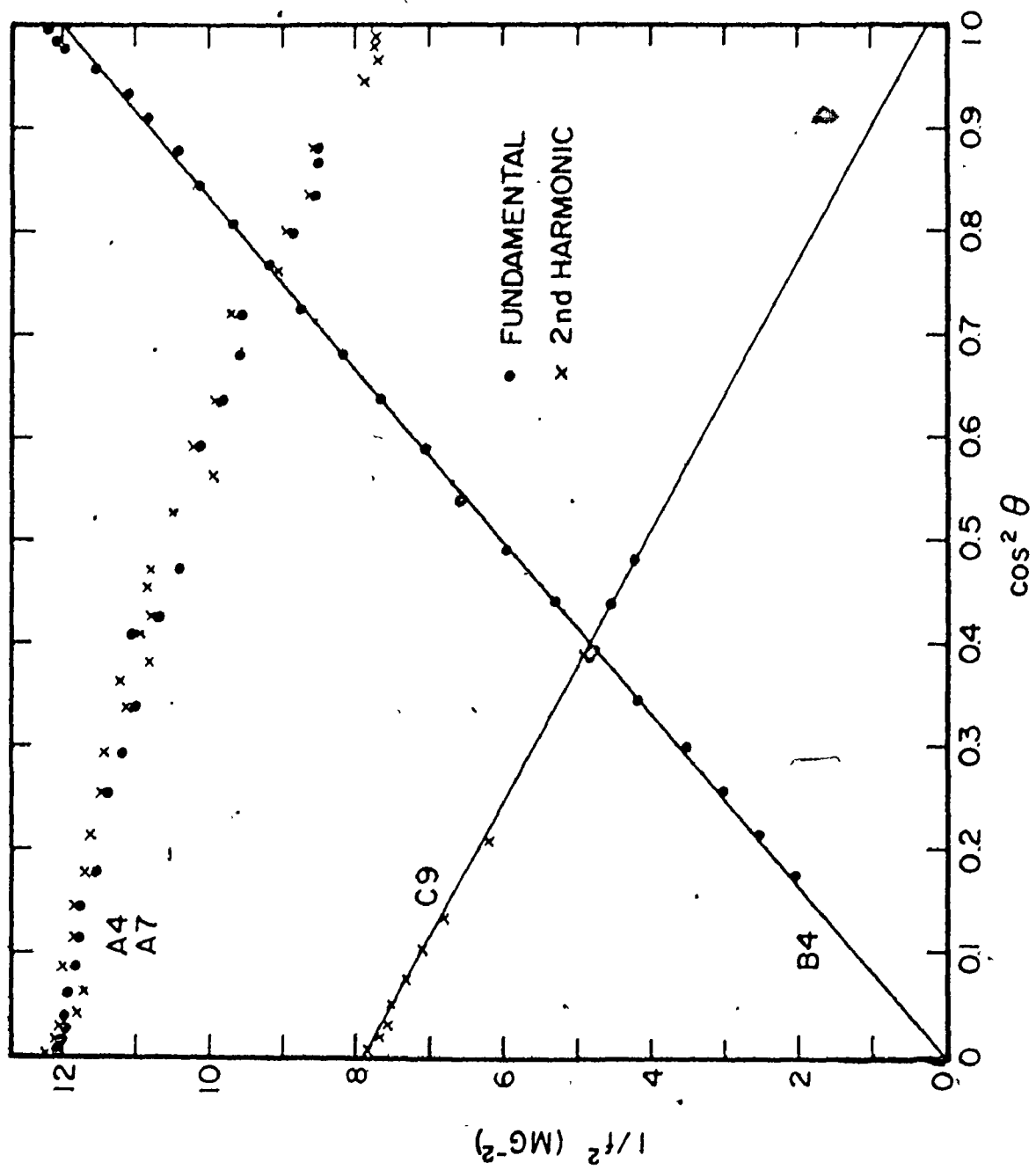
C. Continuous Low Frequencies II

The above two surfaces are the only two closed surfaces obviously evident from the data in Figure 7. However, there are two more which have not previously been identified. The first arises from the branches C9', C9, A7, A4, and B4. B4 and a small part of A4 have been observed only once previously (by Griessen, et al), but were attributed incorrectly to the monster arms. C9 and A7 near the b axis have also been observed previously by Goldstein and Foner and also by Goy, et al. Neither made any claim as to their origin, but Griessen, et al, claimed they were actually harmonics of C7 and A6. This interpretation is also incorrect for two reasons. First, the second harmonics of C7 and A6 intersect at \hat{b} at a frequency of 0.670MG, which is considerably lower than C9 and A7 at approximately 0.713MG, and well outside experimental error even if one tries to read the numbers off of Goldstein and Foner's figures 1 and 2 or Goy's figure 1. Second, if one carefully examines the

data shown by these previous researchers, one notes that the frequencies in question decrease as one rotates the field from \hat{b} toward \hat{c} , whereas the second harmonic of A6 must increase. In fact, for the field 30° from \hat{b} toward \hat{c} , which is the approximate limit of the previous data, A7 has decreased to approximately 0.65MG, while the second harmonic of A6 has increased to approximately 0.78MG.

The following interpretation is therefore presented. For the A and C branches we are dealing primarily with weak signals, but signals definitely above the noise level. However, the fact of weakness is evident in the $1/f^2$ plot of Figure 14. A7 is the second harmonic of A4 and has been halved before plotting. Since C9 and A7 intersect the b axis at approximately the same frequency, C9 is also identified as a second harmonic. The fundamental frequencies of C9 and of A7 near the b axis were not observed. This will be of significance later. The important point to note now is that C9', C9, and B4 indicate ellipsoidal tendencies, whereas A4 and A7 show that this ellipsoid must be reasonably flat and thin in the bc plane, although it deviates from ellipsoidal shape here. The extrapolation of C9 and B4 to the a axis also indicate approximately the same value for $1/f^2$, although one cannot predict a value for the frequency with any high degree of accuracy due to the errors involved. This piece is therefore matched to the seventh-band electron surface between the monster arms in Reed's model.

Figure 14. $1/f^2$ plot for A4-A7-B4-C9-C9',
attributed to the seventh-band
electron surface between the
monster arms.



The predictions of the model for this piece are not good, primarily due to the fact that this piece is extremely sensitive to the exact Fermi level. Reed's calculations used a Fermi level of $0.713Ry$; reducing this to $0.710Ry$ caused this piece to disappear. Therefore, local potential variations such as were used to generate 6h at T could easily be used to modify this piece slightly without appreciably affecting other parts of the model. Frequencies of 5MG, 0.705MG, and 0.468MG are predicted for this piece for the field in the \hat{a} , \hat{b} , and \hat{c} directions respectively. This study indicates frequencies of 0.356MG and 0.287MG for the \hat{b} and \hat{c} directions, and no data is available for the \hat{a} direction. In an attempt to extrapolate the data to the a axis, the inversion process was applied to this data, ignoring the fact that this piece does not have the proper symmetry. Instabilities in the spherical harmonic expansion were again encountered, only 6 terms being possible, with an additional 4 (up to order $\ell = 6$) to reduce the rms error. The coefficients of the expansion are shown in Table 2, and the fitting is shown in Figure 10. The dashed line for C9 and A7 is the calculated second harmonic of the frequencies calculated for C9' and A4. These calculations indicate a frequency for $\Pi \parallel \hat{a}$ of approximately 4MG, although since no data exists for this piece for fields within 25° of \hat{a} , one would have to assign an error limit of at least $\pm 1MG$ to this figure. The radii resulting from this inversion are shown

in Figures 15 and 16. The meanings of the various curves for Figure 15 are the same as those for Figure 11. Here again, it is not valid to believe every small detail, but one can say that this is an extremely flat piece, possibly with some surface wiggles. Also, it is to be expected that this piece should parallel the shape of the monster arms, since it lies between them, so that the drawing in the ac plane, and possibly in the ab plane as well, should show a slight saucer shape similar to $7e$ near Γ , rather than the flat shape shown here. Such a saucer shape would also decrease the expected frequency at \hat{a} in the same manner as $A5$ behaves near b (see Figure 8). The radii predicted from this inversion are approximately 0.008\AA^{-1} , 0.106\AA^{-1} , and 0.120\AA^{-1} in the \hat{a} , \hat{b} , and \hat{c} directions respectively. These can be compared to the model radii of 0.033\AA^{-1} , 0.123\AA^{-1} , and 0.151\AA^{-1} in the \hat{a} , \hat{b} , and \hat{c} directions respectively, and the calculated space available between the monster arms, which has radii in the \hat{b} and \hat{c} directions of 0.128\AA^{-1} and 0.184\AA^{-1} respectively.

The final piece of Fermi surface which can be termed closed with any reasonable certitude based on the data of Figure 7, arises from $A3$ and $B3$. These two branches, in conjunction with $A1$, $A2$, $B1$, and $B2$, have also been observed before, but not with sufficient accuracy, and have not yet been interpreted correctly. Goldstein and Foner observed all six branches, although it was over a

Figure 15. Radius and ellipsoidal deviation for
7e between ar. in the three
principle planes of gallium.

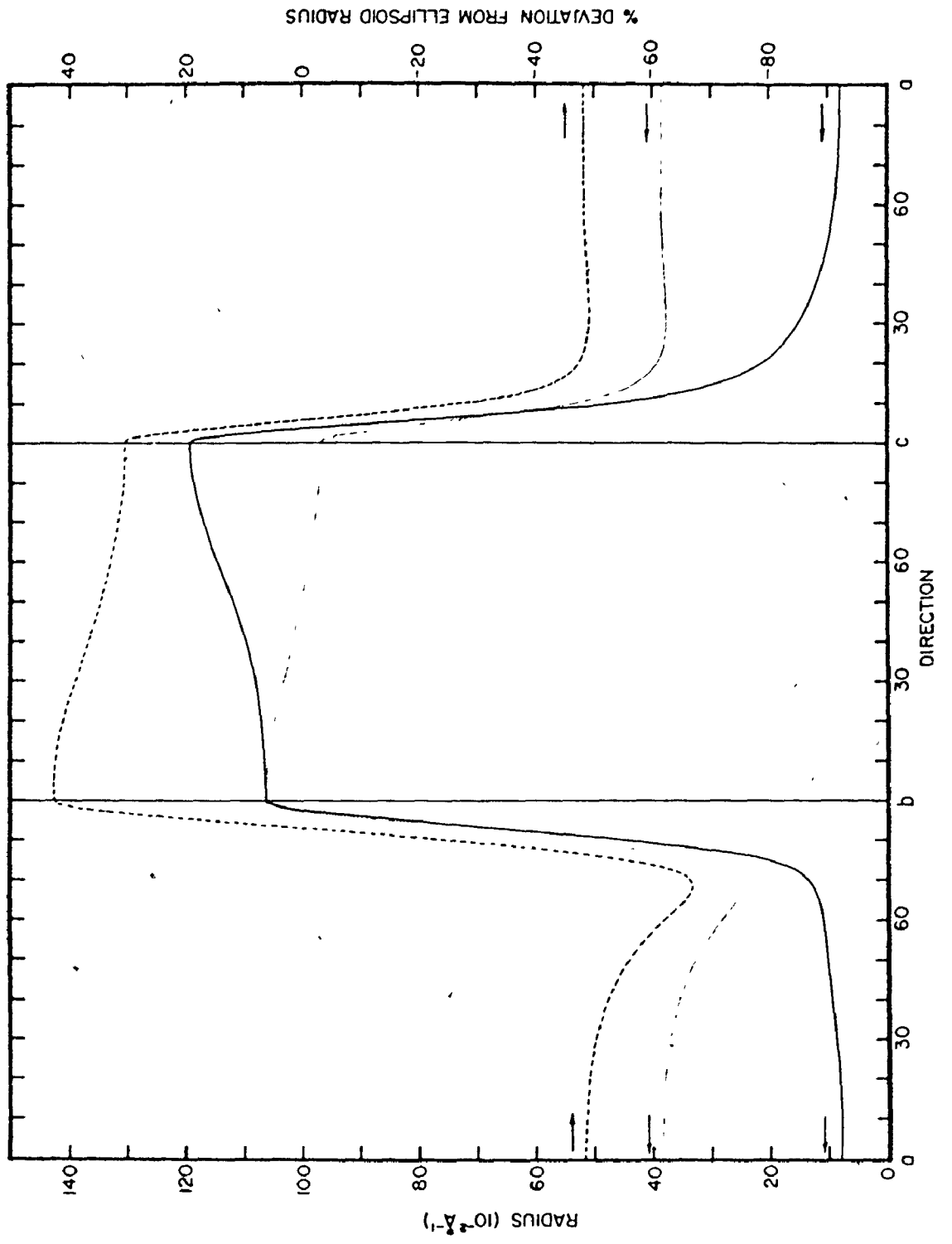
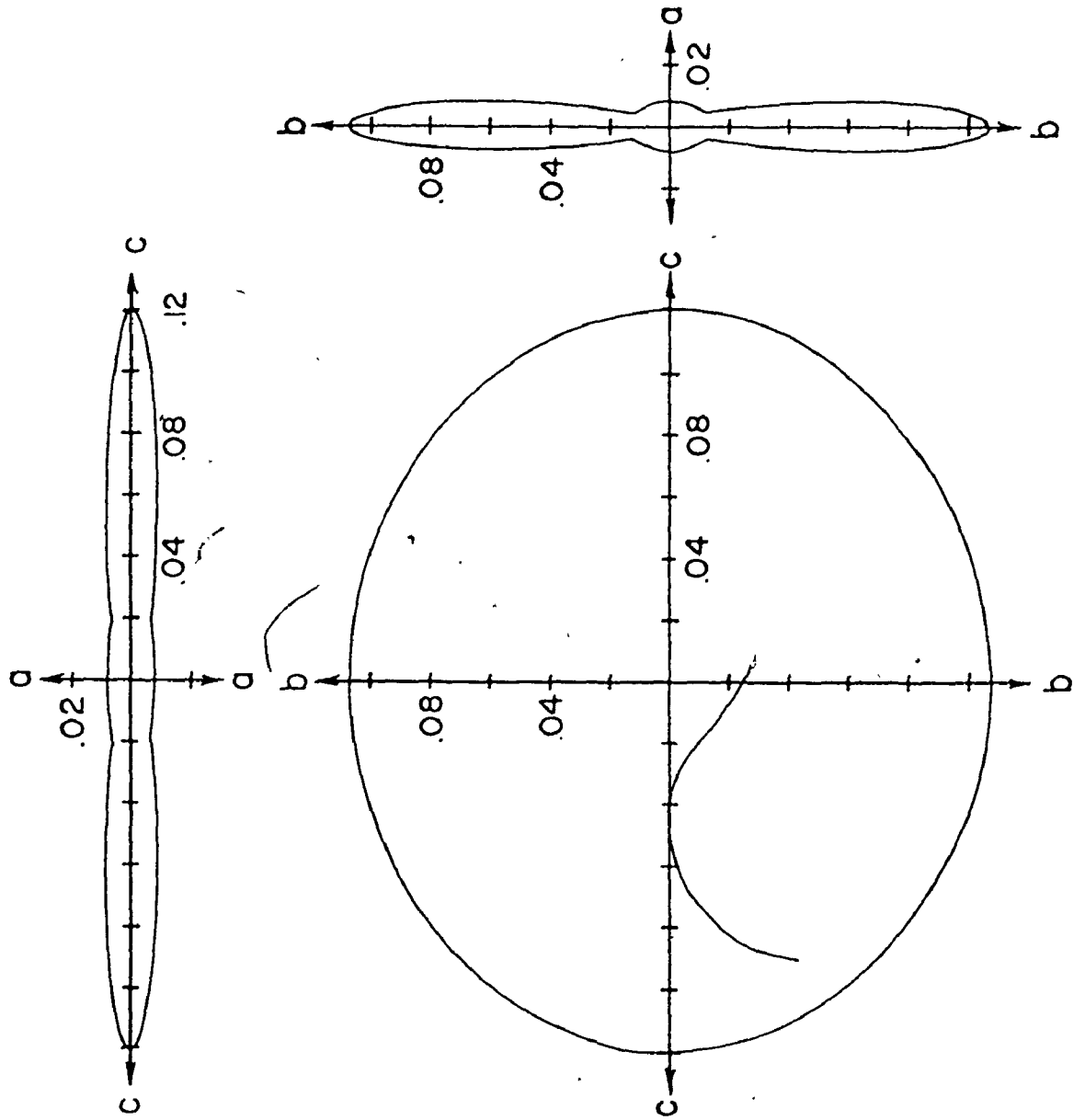


Figure 16. Cross-sectional areas of $7e$ between arms in the three principle planes of gallium, as calculated for Figure 15. The scale is in \AA^{-1} .



more limited angular range and their resolution was not sufficient to distinguish more than two branches at any one position. They were not able to distinguish between B2 and B3 or between A2 and A3 for magnetic fields more than about 35° from \hat{c} , and a careful analysis of their data corresponding to A1 and A2 (their sheet IIIB) will reveal that they observed A1 for fields more than 15° from \hat{c} and they observed A2 for fields less than 15° from \hat{c} , mistakenly taking these as the same branch due to lack of resolution. This explains their statement that near \hat{c} their frequencies may be slightly in error due to the presence of a weak third signal which they could see but could not measure. A similar analysis explains their high values for data corresponding to B1 and B2 near \hat{c} . They made no claim as to the origin of these frequencies. Goy, et al, also observed these frequencies and encountered the same resolution problem, with the same result. Griessen, et al, were the first to accurately distinguish all three branches at one position, but they did not observe B2, and observed A2 only for a limited range centred approximately 20° from \hat{c} . They then attributed A2 to magnetic breakdown between A1 and A3, and assigned the latter two branches to fifth- and sixth-band hole ellipsoids at X in Reed's model. This is almost correct except for the fact that Reed's model does not support a sixth-band hole ellipsoid at X, and in view of the continuous nature of the present data, an explanation requiring magnetic breakdown is not very

likely.

A more reasonable explanation is obtainable as follows. The $1/f^2$ plots for the six branches A1-3 and B1-3 are shown in Figures 17 and 18. Notice that A3 and B3 when plotted in this manner form almost perfect straight lines, within experimental error. Also, the data extends from \hat{c} nearly 80° toward \hat{a} and \hat{b} , where the signal finally faded. If one extrapolates the data the last 10° , using these two figures, one arrives at nearly the same frequency. It is therefore reasonable to suppose that A3 and B3 arise from a small nearly ellipsoidal piece of Fermi surface with two nearly equal axes in the \hat{a} and \hat{b} directions and one longer axis in the \hat{c} direction. Only one piece of Reed's model fits this description, and that is the fifth-band hole ellipsoidal surface at X, as surmised by Griessen, et al. But only A3 and B3, not the other four branches, are assigned to this piece. Since X has the proper symmetry properties, the inversion algorithm was applied to this data. Due to a complete lack of data in the third plane, it was possible to fit only three terms in the spherical harmonic expansion, with an additional three (up to order $\ell = 4$) for reducing the rms error. The fitting parameters are shown in Table 2, and the fit is shown in Figure 10. This shows that the dHvA frequencies for the field along \hat{a} , \hat{b} , and \hat{c} are expected to be 0.849MG, 0.885MG, and 0.223MG respectively. The radii

Figure 17. $1/f^2$ plot for B1, B2, and B3. The first two branches are attributed to the monster arms, and the last branch is attributed to the fifth-band hole surface at X.

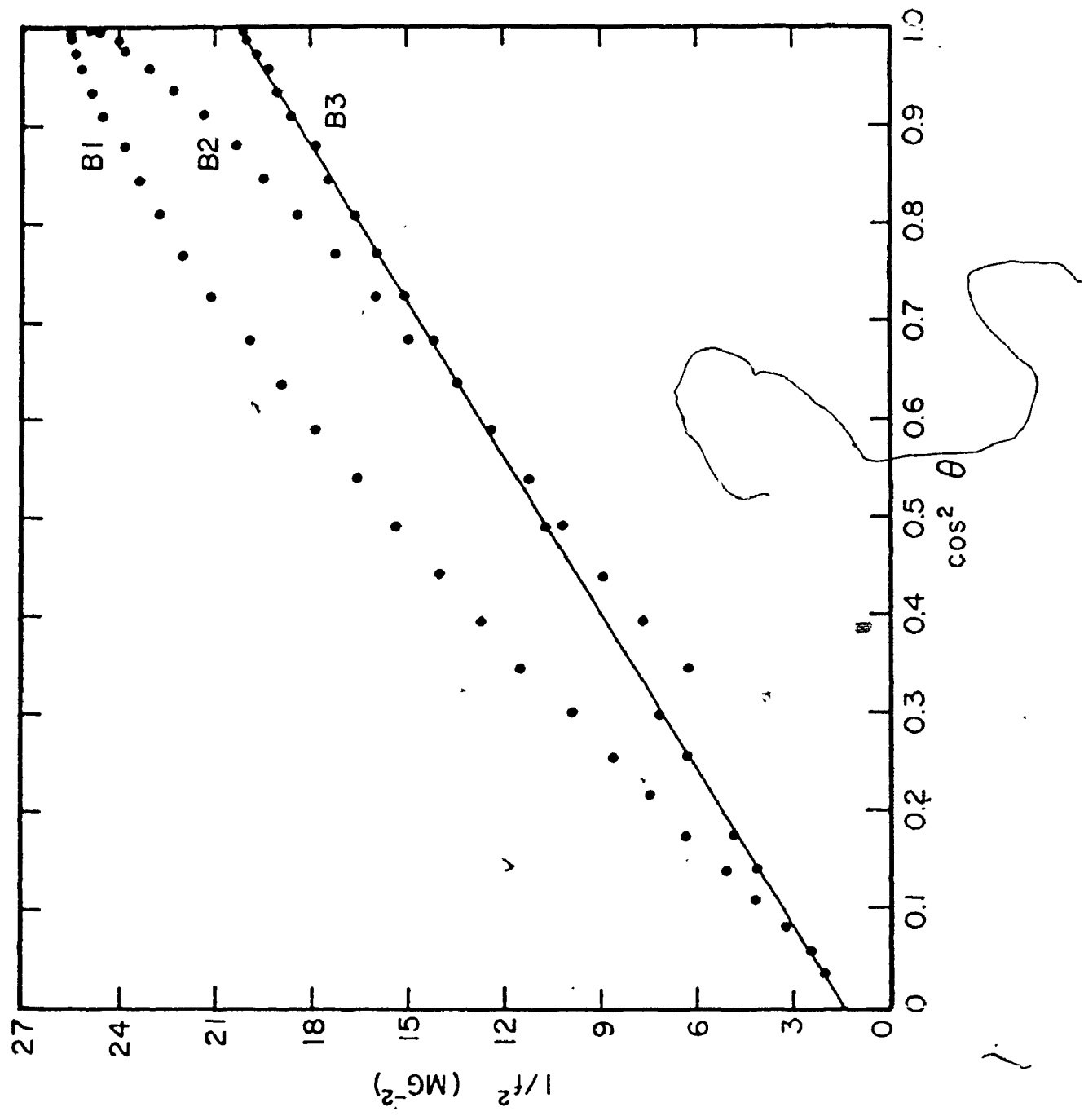
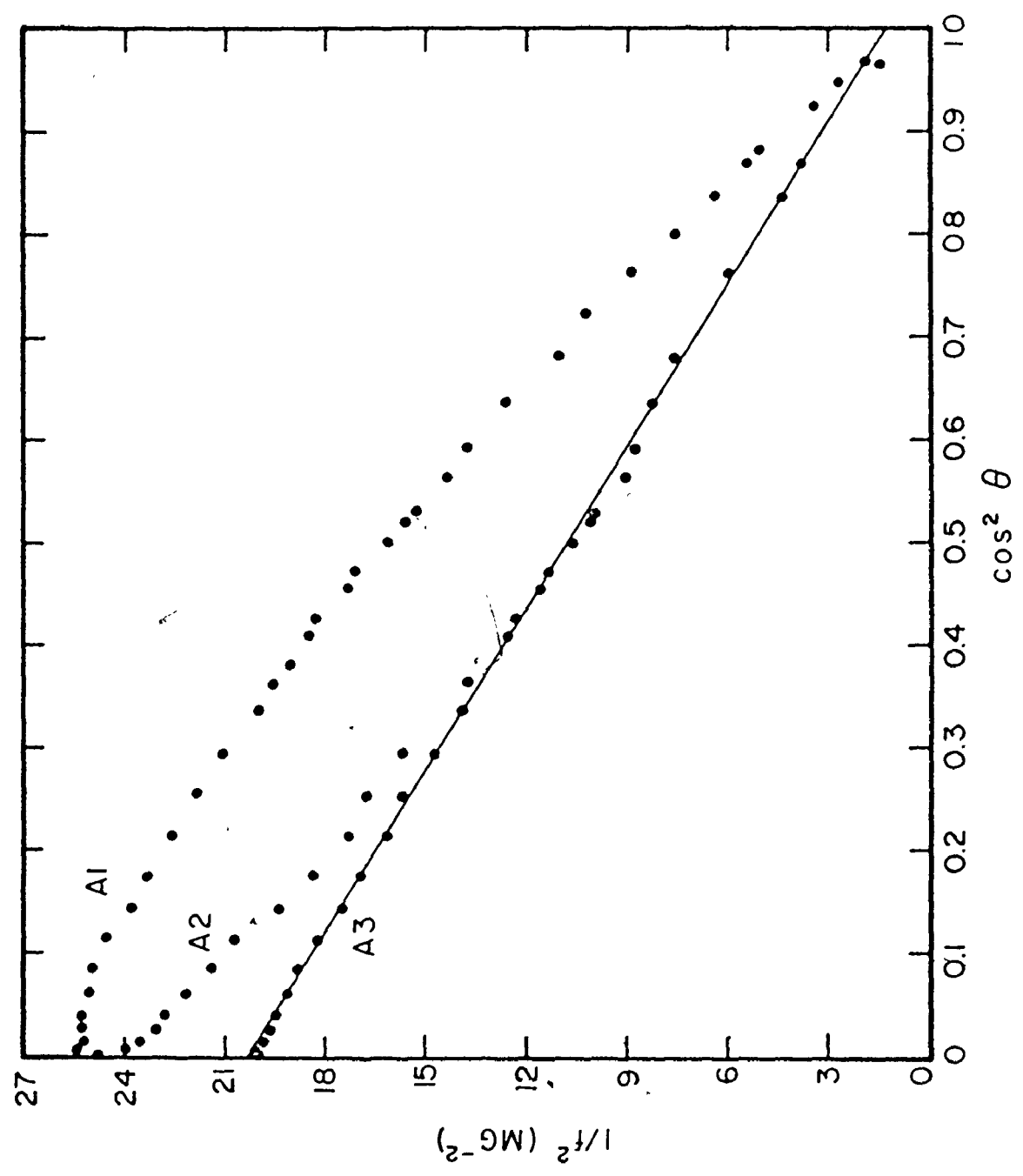


Figure 18. $1/f^2$ plot for A1, A2, and A3. The first two branches are attributed to the monster arms, and the last branch is attributed to the fifth-band hole surface at X.



and ellipsoidal deviation are shown in Figures 19 and 20. The right-hand scale of Figure 19 is extremely expanded, so that this piece is more ellipsoidal than would appear from Figure 19, as shown in Figure 20. It is roughly circular in the ab plane, with a radius of 0.026\AA^{-1} , and has a radius in the \hat{c} direction of 0.10\AA^{-1} , whereas Reed's model predicts 0.07\AA^{-1} for the latter. This 30% error is probably due to the fact that early very limited data by Condon appeared to show an extremely small frequency which was thought to be generated by this piece of surface, so that this ellipsoid in Reed's model was thought to be an order of magnitude too large if it was in error at all. It now appears that this piece is, in fact, larger than calculated.

It is also reasonable that no data was observed for this piece in the ab plane, since all extremal orbits measured for this piece in this plane must intersect the c axis of this piece, which is the crystallographic line XRL. If spin-orbit splitting were added to Reed's model, the degeneracies existing on the hexagonal face would not be lifted along this line (Koster, 1962). Therefore, if an electron were traversing one of these extremal orbits, then upon reaching the line XRL it would be very likely to cross over to the monster, which must decrease the signal, since only complete traversals of the orbit are measured.



Figure 19. Radius and ellipsoidal deviation for
5h at X in the three principle planes
of gallium.



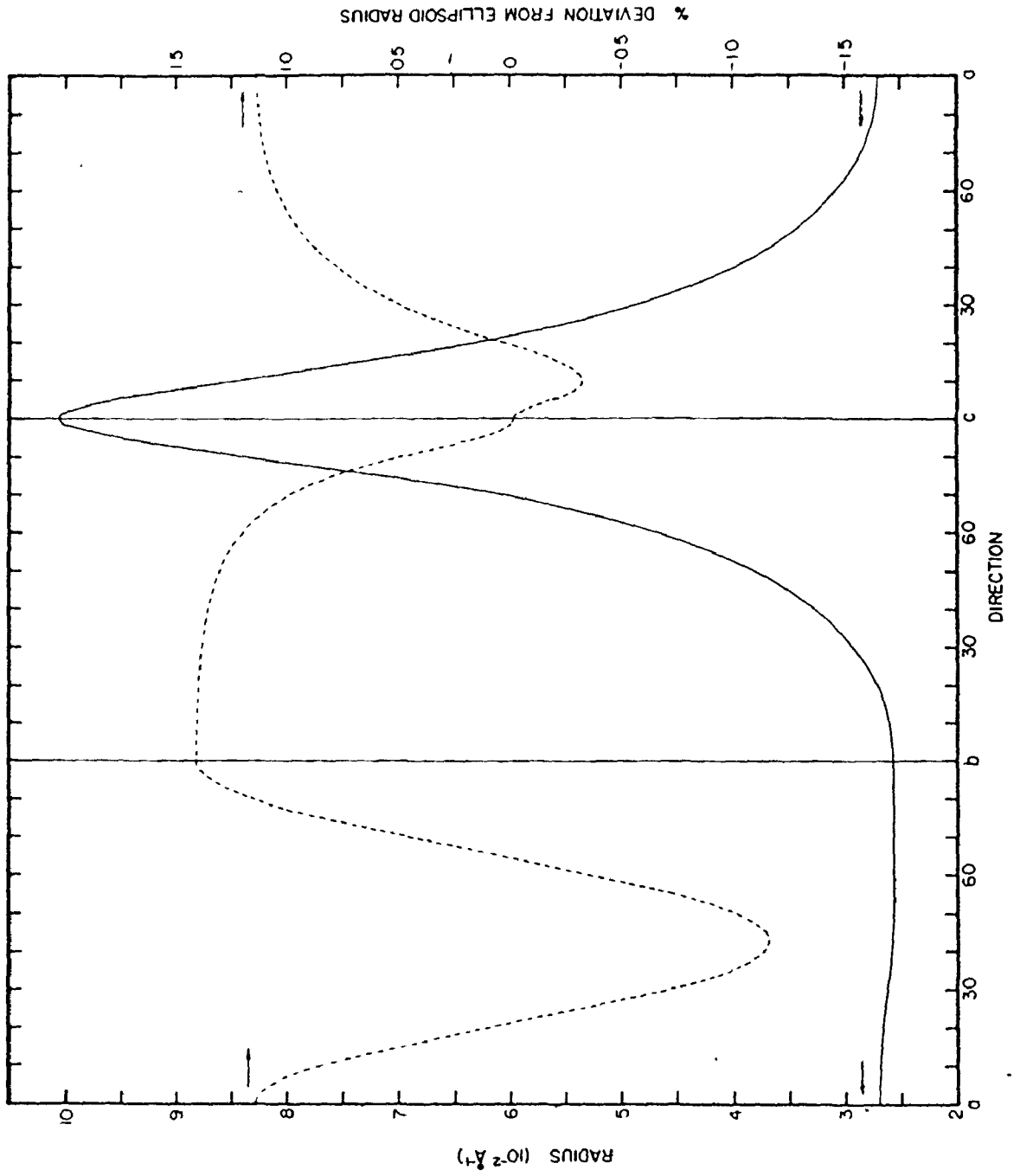
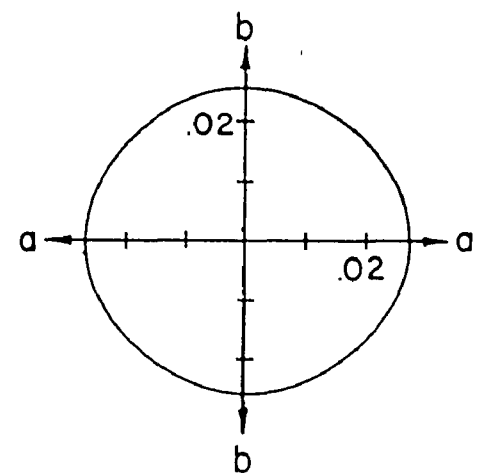
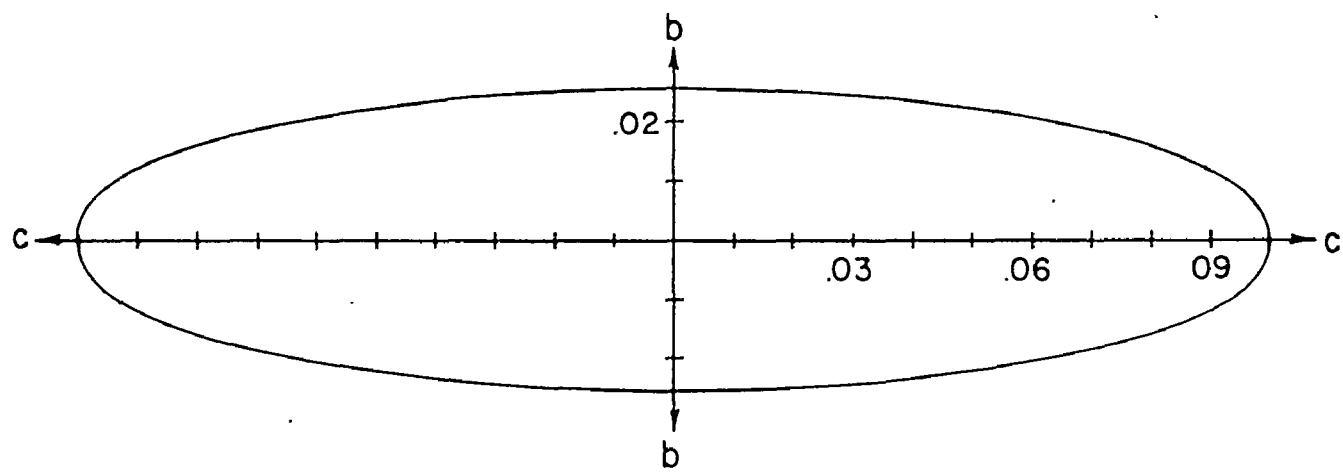
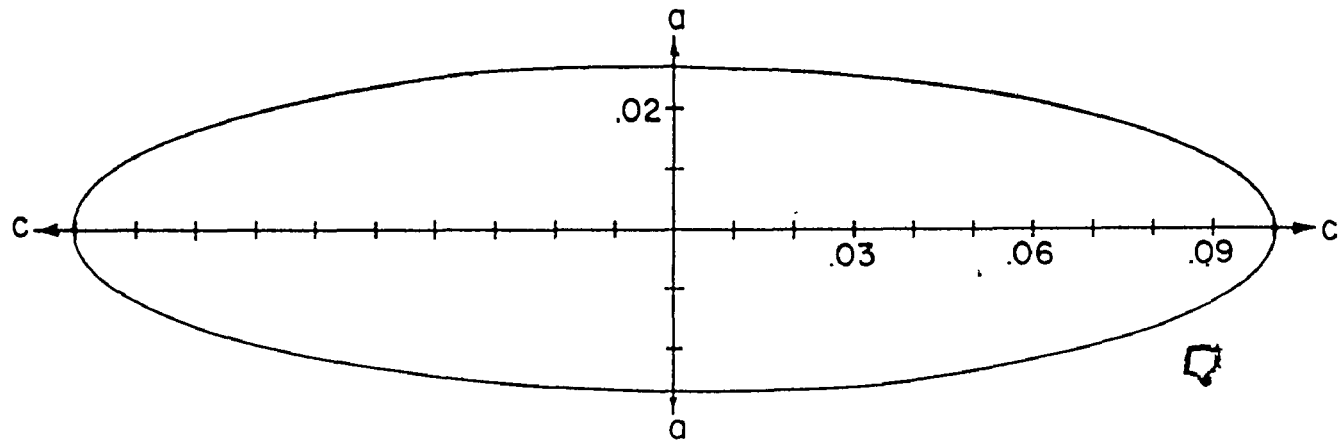


Figure 20. Cross-sectional areas of $5h$ at X in the three principle planes of gallium, as calculated for Figure 19. The scale is in \AA^{-1} .



D. Discontinuous Low Frequencies

There still remains the problem of the origin of A1, A2, B1, and B2. Figures 17 and 18 clearly show that these are not due to ellipsoids. The only other known parts of the Fermi surface with approximately the same cross-sectional area as $5h$ at X for $\bar{\Pi}|\hat{c}$, and for which the cross-section should increase if the field were rotated away from the \hat{c} axis, are the monster arms. Figures 21 and 22 show two detailed views of this region, the first being a view from the \hat{b} direction, and the second from the \hat{a} direction. In Figure 21, if the magnetic field is rotated away from \hat{c} (horizontal) toward \hat{a} (vertical), then the extremal cross-sections of the two arms in the plane normal to the field will not be the same because these arms are no longer equivalent. The cross-section α of the upper arm (suitably adjusted for an extremum) will be greater than the cross-section β of the lower arm, which implies a higher dHVA frequency for α as compared to β . If the field is rotated farther in the same direction, then the resulting cross-section α will eventually not be possible due to the interference of the rest of the monster, whereas the cross-section β will still exist. It is estimated that the limiting angles for α and β are approximately 55° and 80° respectively. Similarly, Figure 22 shows that if the field is rotated from \hat{c} (horizontal) toward \hat{b} (vertical) the two arms are again non-equivalent, resulting in the cross-section γ of the lower

Figure 21. View of the gallium Fermi surface
from the \hat{b} direction. The small,
surfaces at N and T have been
deleted for clarity.

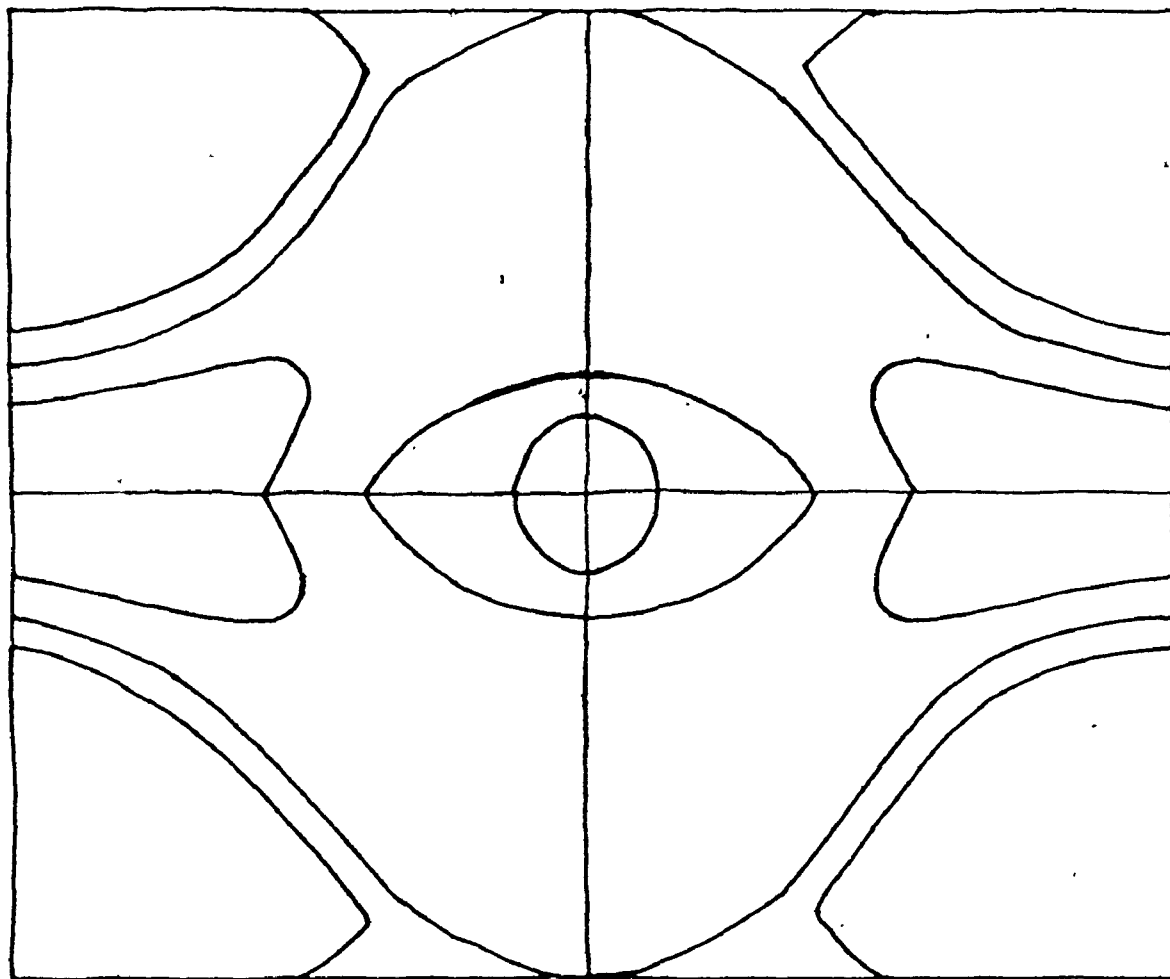
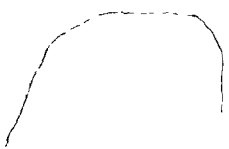
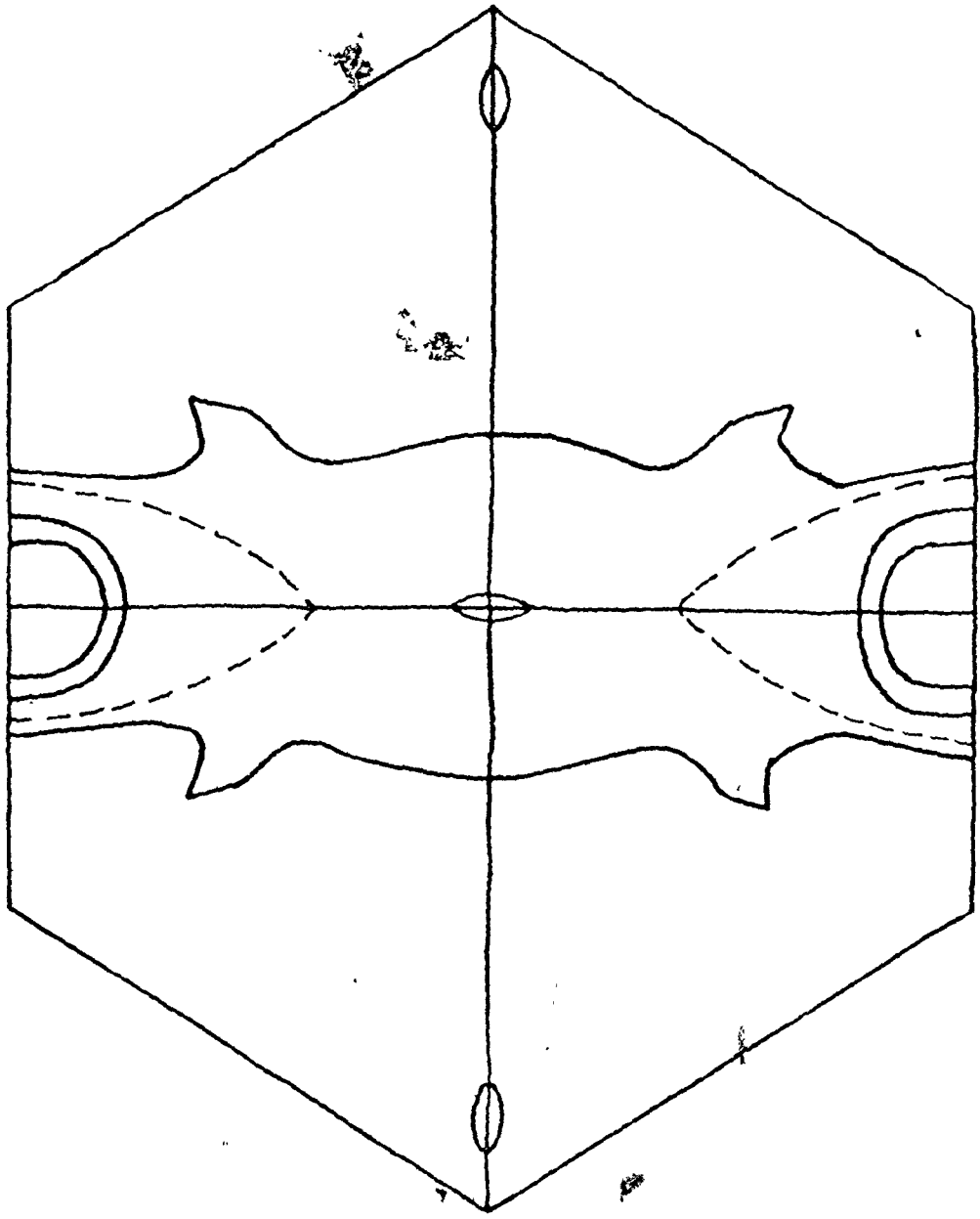


Figure 22. View of the gallium Fermi surface from the \hat{a} direction. The small surfaces at N have been deleted for clarity.



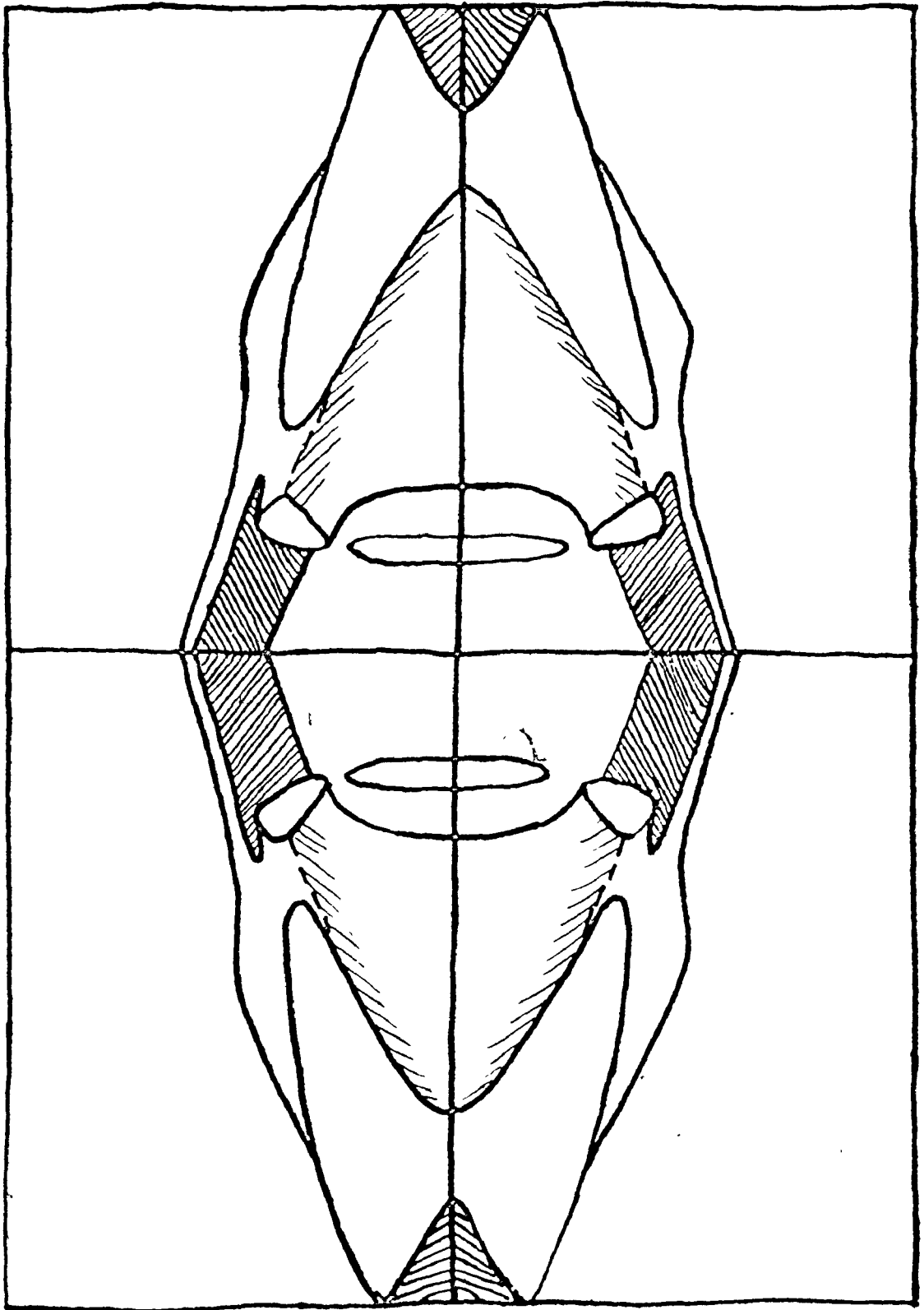
arm being larger than the cross-section δ of the upper arm, with γ disappearing at approximately 55° from \hat{c} , whereas δ persists to approximately 75° from \hat{c} . Figure 17 shows that B2 disappears at approximately 54° from \hat{c} toward \hat{a} and B1 disappears approximately 77° from \hat{c} toward \hat{a} . Figure 18 shows that A1 disappears at approximately 79° from \hat{c} toward \hat{a} and A2 exists only up to approximately 50° from \hat{c} toward \hat{b} . Thus A1, A2, B1, and B2 behave almost exactly as one would expect if these branches originated in the monster arms. Only one point detracts from this assignment, and that is that Reed's model predicts a frequency of 0.37MG for the monster arms with $\bar{H}|\hat{c}$, which is considerably larger than observed.

We consider now branches C6 and B10, which are branches having minima for the field along the \hat{a} direction, increasing as the field rotates away from \hat{a} , and eventually disappearing. Griessen, et al, suggested that these branches might be assigned to orbits around the monster legs in the plane $k_x = 0$, but rejected the idea on the basis of the sensitivity of these parts to the Fermi energy, preferring instead to assign these orbits to the frequency branches C1 and B7, which are also quite sensitive. Since this study did not observe C1 and B7 over a sufficient angular range, no claim is made as to their origin. However, this study does support Griessen's original hypothesis of assigning C6 and B10 to the monster leg orbits for the following reasons. First, it has been

shown that the seventh-band electron surface between the monster arms is slightly smaller than Reed's expectations, which implies that the Fermi level is, if anything, slightly lower than calculated. If this is true, then the hole surfaces should be slightly larger, making it more likely that the monster leg is larger than calculated, if it is to be greatly different at all, than that the leg is a factor of 4 smaller than calculated, as Griessen's second hypothesis would require. Actually, Reed's model predicts a frequency of 0.45MG for an orbit around the leg in the plane $k_x = 0$, whereas C6 and B10 give a frequency of 0.419MG for $\vec{H} \parallel \hat{a}$. This alone is almost sufficient reason to confirm the assignment. However, the second reason for supporting the assignment concerns the angular range of the data, which shows that C6 disappears for the field more than 36° from \hat{a} toward \hat{b} , and B10 disappears for the field more than 16° from \hat{a} toward \hat{c} . On Figure 21, if one draws a line from the centre of the figure to a point near the top of the monster leg, the angle between this line and the c axis is approximately 18° . If one draws a similar line on Figure 23, a view of the Fermi surface from the \hat{c} direction, one obtains an angle of approximately 40° . These are close enough to the data to confirm the assignment.

The final set of low frequencies to be discussed are C2-5, B8, and B9. The latter two have been observed by Goy, et al, and Griessen, et al, have observed this entire set

Figure 23. View of the gallium Fermi surface from the \hat{c} direction. The small surfaces at N and T, and the seventh-band electron surface near Γ , have been deleted for clarity.



of branches. It should be noted here that C2 and C3, and also C4 and C5, would be identical if the orientation error described in section IV had not occurred. For that reason Griessen, et al, observed only two branches here. Therefore, the fact of the orientation error in the present study now becomes a useful feature rather than a hinderance, for it shows the sensitivity of the pieces generating these branches to small orientation errors, and it proves that there is actually a degeneracy for the field in this plane. These branches have been attributed to the seventh-band electron butterfly surface at N for which Reed predicts a frequency of 0.22MG for the field in the \hat{a} direction. He also predicts the same frequency at this orientation for the eighth-band electron ellipsoid inside the butterfly at N. This ellipsoid-butterfly combination is not oriented with symmetry axes parallel to the crystal axes, so that extremal frequencies are not expected for the field along symmetry directions. This is clearly shown in Figure 7, but it is not obvious whether the branches shown belong to the butterfly or the ellipsoid. Figures 24 and 25 show $1/f^2$ plots for these branches. B9, C4, and C5 were reflected across \hat{a} before plotting, and all angles were shifted by an angle θ_0 , which is the angle at which the appropriate curve shows a minimum. These angles θ_0 were least-square fitted for each curve. As can be seen, when plotted this way the data form a nearly perfect straight line in all cases,

Figure 24. $1/f^2$ plot for B8 and B9, attributed to the electron pieces at N. The shift angle was $\theta_0 = 58.6^\circ$.

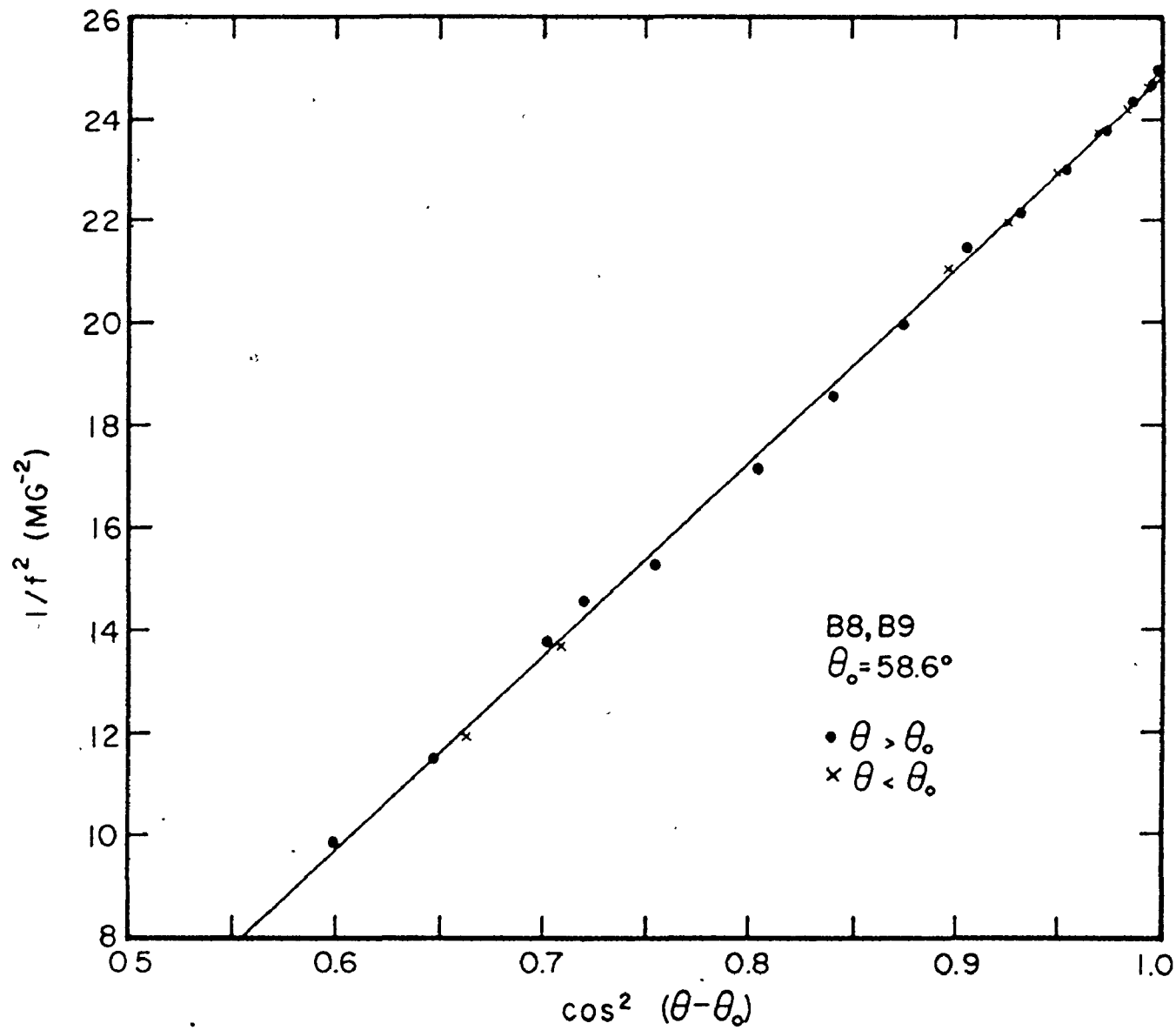
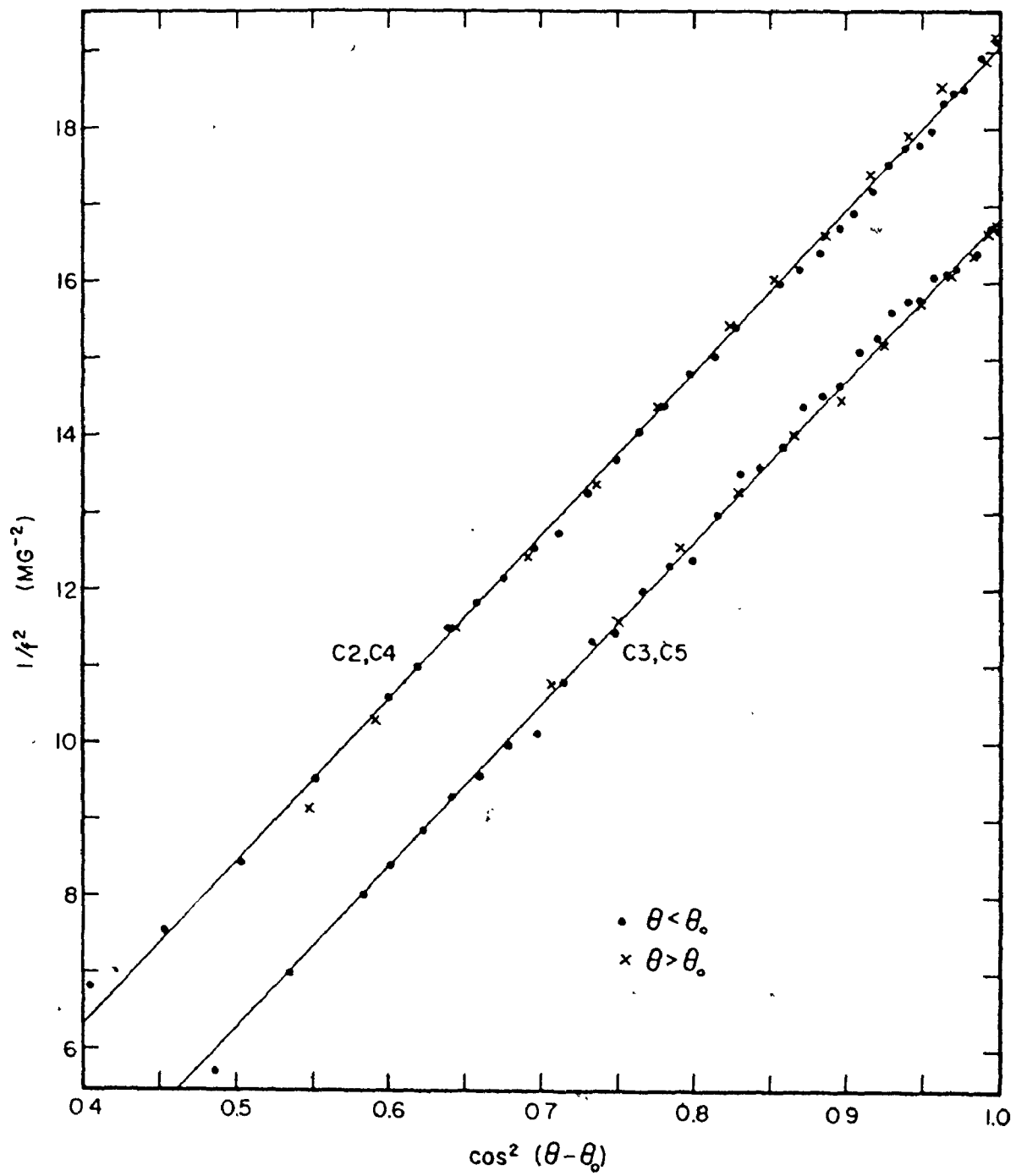


Figure 25. $1/f^2$ plots for C2-5, attributed to the electron pieces at N. The shift angle was $\theta_0 = 23.9^\circ$ for C2 and C4, and $\theta_0 = 24.9^\circ$ for C3 and C5.



within experimental error. This suggests that the piece is oriented approximately 31° from \hat{a} toward \hat{c} and 24° or 25° from \hat{a} toward \hat{b} , and that the piece is ellipsoidal in shape. However, it does not prove the latter hypothesis since it will be seen that even a butterfly piece could produce such straight lines over a small angular range in a $1/f^2$ plot. In fact, there is evidence that the piece is not ellipsoidal, since if Figures 24 and 25 are extrapolated to $\theta = 0^\circ$ for Figure 24 and $\theta = 90^\circ$ for Figure 25, the extrapolated value of $1/f^2$ is -2.739 for B8 and B9, 1.291 for C2 and C4, and -0.554 for C3 and C5. The two negative values are, of course, physically impossible. One may argue that due to the misalignment only the average of the two lines shown in Figure 25 should be used, which would give a value of $1/f^2 = 0.737$ for the C2-5 complex, but that does not explain the negative value for B8 and B9. More experimental data will be needed before these branches can be satisfactorily explained.

E. High Frequencies: Predictions

We turn now to a consideration of the high frequencies shown in Figure 8. Few of these have been seen before, and many of those were seen with insufficient angular resolution, making identification impossible. Only C12, A9-11, and B12-15 can be said to have been seen previously with any degree of accuracy, and that was done by Goldstein and Foner. However, a comparison of data between their results and the

present study, in terms of both angular extent and frequencies observed, is in most cases meaningless due to the far greater scope of the present data.

It is immediately obvious from Figure 8 that these high frequencies are extremely complex. Reed's high frequency predictions are therefore presented first before considering the data. It will be instructive to refer to Figure 4, a drawing of the gallium Fermi surface, throughout this section. These high frequencies are due primarily to the ellipsoid-butterfly combination at L, but some are also due to the monster surface. Beginning with the field in the \hat{a} direction, the model predicts that the ellipsoid should have a maximum cross-sectional area in the hexagonal face of the Brillouin zone corresponding to a frequency of 12.2MG. The orbit causing this frequency will also be a minimal orbit for the butterfly, since the two pieces are degenerate in this face of the zone (without spin orbit interaction). If the field is rotated away from the \hat{a} direction, this degeneracy in orbits is lifted, and the frequency should split into two branches. The maximum area of the butterfly for $\vec{H} \parallel \hat{a}$ occurs for a non-central orbit near the plane $k_x = \frac{1}{2}k_a$ and corresponds to a frequency of 22.2MG. There is also the possibility of extremal orbits encircling the monster just above the monster arms and below the bulge in the sides of the monster. No frequency is given for these orbits, but if they exist, they would be several times larger than this

non-central orbit.

For $\bar{H} \parallel \hat{b}$ the model predicts several frequencies. First, it predicts a central maximum orbit for the ellipsoid with a frequency of 20.9MG. It also predicts a central minimum orbit for the butterfly with a frequency of 35.9MG, and a central orbit composed of half of each of the above orbits with a frequency of 28.4MG. This orbit is due to magnetic breakdown between the seventh- and eighth-band pieces in the hexagonal face of the zone. There is also a non-central maximum orbit on the butterfly near $k_y = \frac{1}{2} k_b$ with a frequency of 42.6MG. Since the ellipsoid should have a radius of slightly more than $\frac{1}{2} k_b$ in the \hat{b} direction, there is also the possibility of magnetic breakdown from this non-central orbit on the butterfly to a non-extremal orbit on the ellipsoid, resulting in a frequency of 21.5MG. However, this magnetic breakdown orbit in itself is neither a maximum nor a minimum orbit, since the maximum orbit is a central orbit with the frequency given above as 28.4MG, and this two-winged butterfly, as it is called (see section H of this chapter), does not support a minimum orbit normal to \hat{b} . This orbit generates a dHvA frequency solely because most of it is due to a maximum orbit which has been broken into two pieces due to magnetic breakdown.

On the monster, there are two belly orbits possible in the plane $k_y = 0$ for $\bar{H} \parallel \hat{b}$. The first encompasses two back-to-back monsters joined at X and has a frequency of

52MG. The second is due to magnetic breakdown between the monster and the 5h at X piece on the hexagonal face of the zone and has a frequency of 26.4MG. This orbit encompasses one monster and the small ellipsoid at X. Neither of these two belly orbits will exist if the field is not within a small angle of \hat{b} since both depend upon the existence of the small junction between the monsters at X, and both orbits must traverse the backbone of the monster.

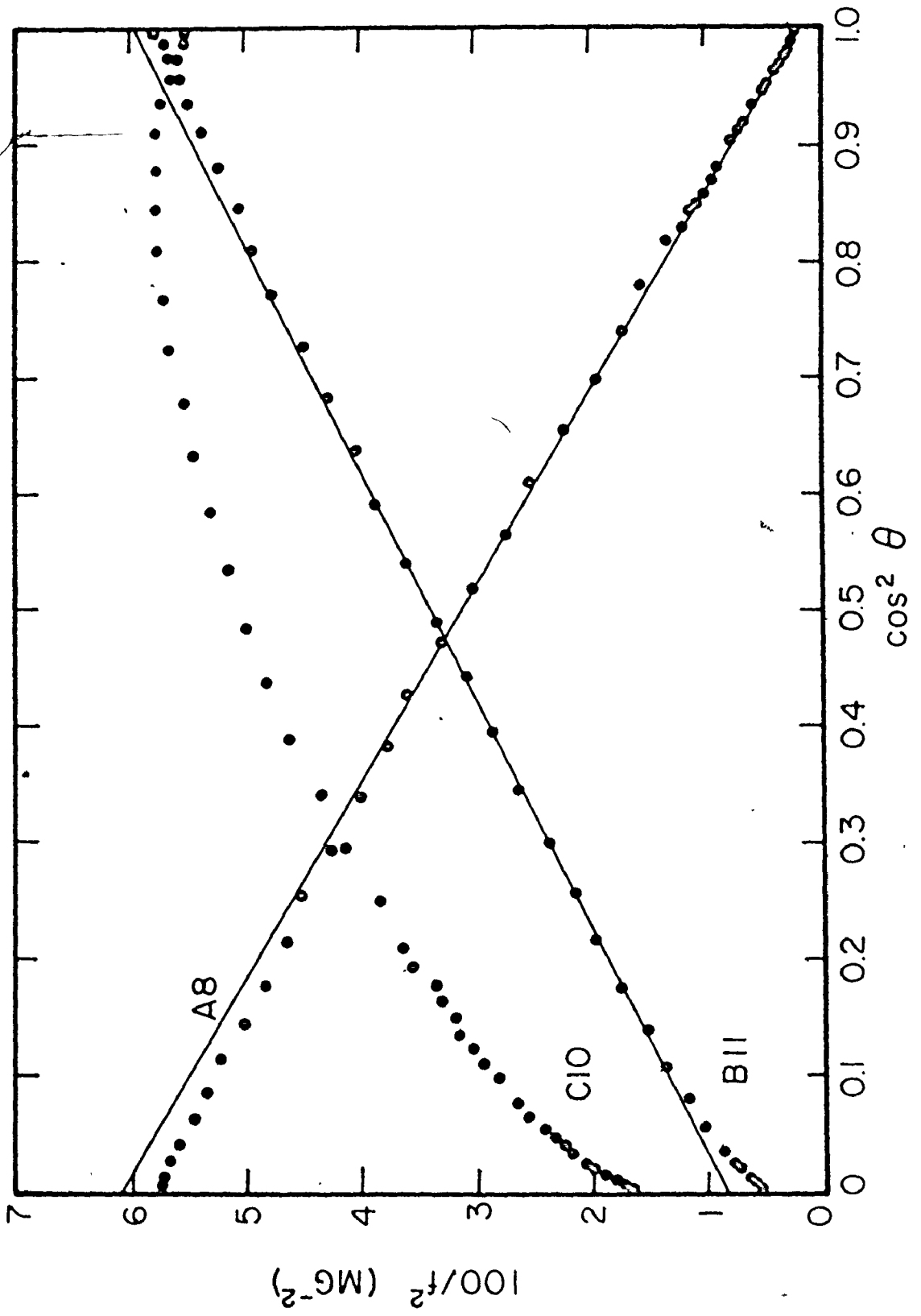
For $\bar{H} \parallel \hat{c}$ the model predicts frequencies of 3.94MG for the ellipsoid, 21.8MG due to a four-winged butterfly orbit on the seventh-band electron surface, and 12.7MG for a two-winged butterfly orbit composed of half of each of the above orbits and due to magnetic breakdown at the hexagonal face of the zone. There is also one non-central maximum monster orbit near $k_z = \pm \frac{1}{4} k_c$ having a frequency of 11.2MG, a central monster orbit at $k_z = 0$ due to magnetic breakdown between the monster and the 5h at X ellipsoid with a frequency of 10.9MG, and a central double monster orbit at $k_z = 0$ encompassing two back-to-back monsters with a frequency of 21.8MG. This last orbit is expected to have the same frequency as the four-winged butterfly orbit. Reed also mentions the fact that there may be magnetic breakdown between the monster and the 7e near Γ pieces which gives open orbits in the k_x direction in the plane $k_z = 0$. This open orbit traverses the outside of a pair of back-to-back monsters and the inside of the electron pieces. If this is true, then the same magnetic

breakdown could give a maximum central closed orbit inside the monster surface and outside the electron pieces. From drawings supplied by Reed, we calculate that the frequency due to this orbit should be approximately the same as that due to the double monster orbit, or 21.8MG.

F. High Frequencies- 8e at L

Returning to the data of Figure 8, there are only two frequency branches, besides C8-A5-B5 previously discussed with the low frequencies, which can be traced through all three planes. These are C10-A8-B11 and C12-A10-B14. The latter has been seen before in its entirety, but the former is new. Figure 26 shows the $1/f^2$ plots for these new branches. The scale for this figure has been expanded by a factor of 10 for C10. In two planes this piece can be fitted to an ellipsoid quite well, although A8 shows deviations for the field near the c axis and B11 shows deviations for \bar{H} near both \hat{a} and \hat{c} . The ab plane (C10) definitely does not fit an ellipsoid prediction. The frequencies for this piece for the field in the \hat{a} , \hat{b} , and \hat{c} directions are 14.4MG, 24.5 MG, and 4.16MG respectively, which are larger than the frequencies of 12.2MG, 20.9MG, and 3.94MG predicted for the 8e at L ellipsoid. However, the 14.4MG frequency splits into two branches if the field is rotated away from \hat{a} . If the field is rotated more than approximately 9° from \hat{a} toward \hat{c} , then B17 disappears. On Figure 21 the angle

Figure 26. $1/f^2$ plot for A8-B11-C10, attributed to 8e at L. The scale for C10 has been expanded by a factor of 10 to read $1000/f^2$.



between the plane $k_x = \frac{1}{2}k_a$ (the top line) and a line joining the corner of the figure (the point L) to the tip of the butterfly is approximately $8\frac{1}{2}^\circ$. This splitting and the disappearance of B17 at the proper angle, when added to the fact of the proximity of the numbers, is enough to confirm the assignment.

Since L has the proper symmetry, the inversion algorithm was applied to the data. As for the 6h at T piece, it was possible to fit only six terms of the spherical harmonic expansion before encountering instabilities, with an additional 15 terms to reduce the rms error before again encountering instabilities. The resulting coefficients are shown in Table 2, and the fitting is shown in Figure 27.. This figure takes into account the fact of the orientation error at the \hat{a} direction in the ab plane. The fit is good everywhere except within 2° of the \hat{a} direction in the ac plane, and except for part of the ab plane. However, the rms error for this piece was approximately 0.1MG, with most of that error coming from the data in the ab plane, so the fit is not unreasonable. The results of the inversion are shown in Figures 28 and 29. Again, the small details of the inversion, such as the ellipsoid deviation near \hat{c} and the large depression in the cross-section in the ab plane, are believed to be caused by the lack of data in the non-symmetry directions and are therefore doubtful. However, the extremal dimensions in the \hat{a} , \hat{b} , and \hat{c} directions of 0.170\AA^{-1}

Figure 27. Spherical harmonic expansion of the data for $8e$ at L . Points shown are the data points of Figure 8 and Appendix C, and the line shown is the least-square spherical harmonic expansion fit to the data using the parameters shown in Table 2.

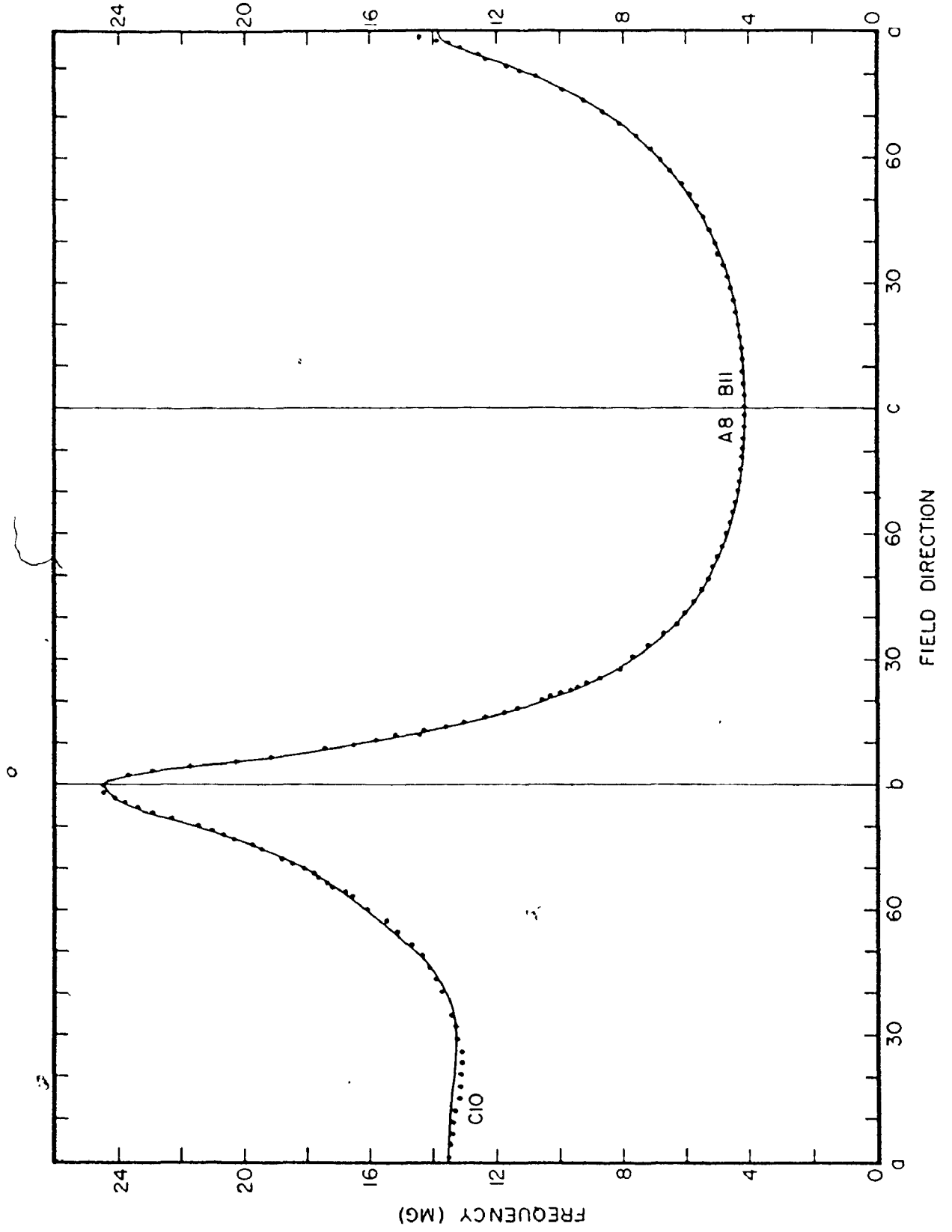


Figure 28. Radius and ellipsoid deviation for
8e at L in the three principle planes
of gallium.

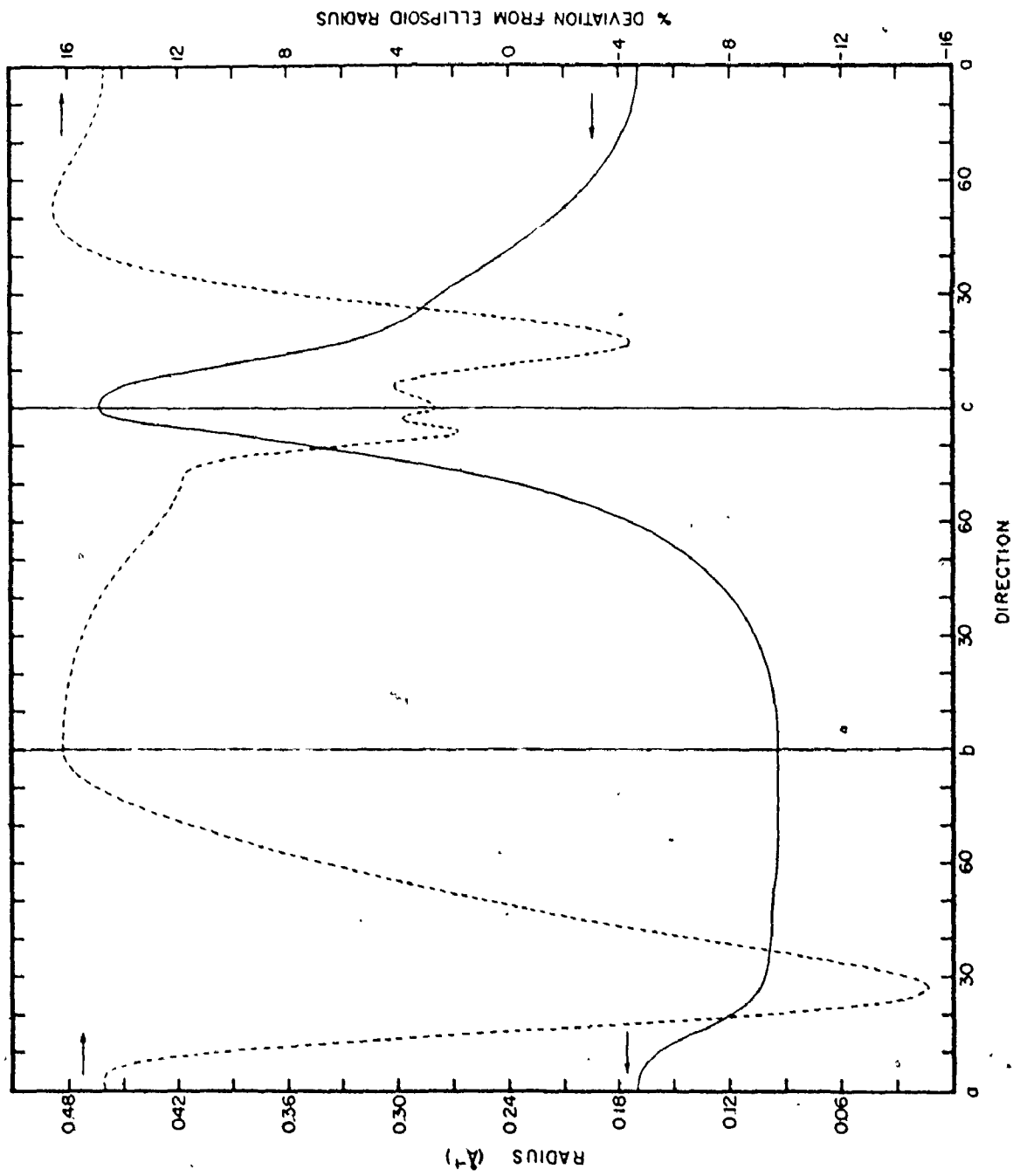
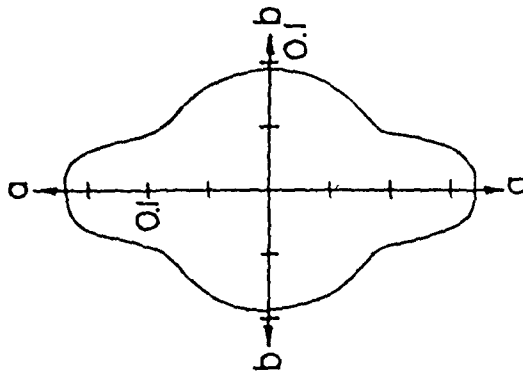
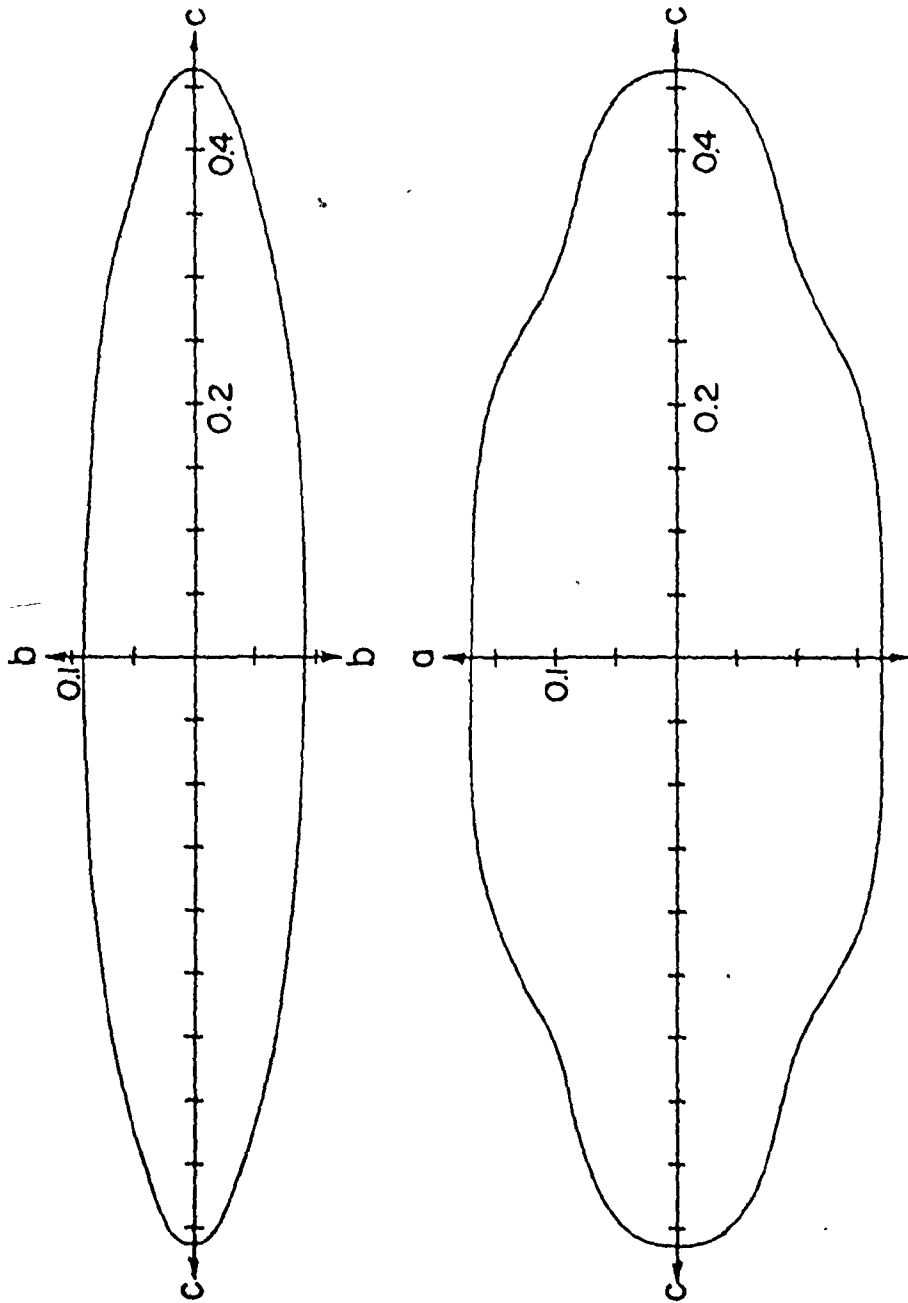


Figure 29. Cross-sectional areas of $8e$ at L in the three principle planes of gallium, as calculated for Figure 28. The scale is in \AA^{-1} .



0.093\AA^{-1} , and 0.462\AA^{-1} respectively compare reasonably well with the expected dimensions of 0.16\AA^{-1} , 0.095\AA^{-1} , and 0.43\AA^{-1} .

G. High Frequencies for $\bar{H}|\hat{a}$

As noted before, C12, A10, and B14 have been seen before, and have been assigned to the butterfly by Reed. But not all parts of these are due to central orbits. As noted when discussing the data for 8e at L, the 14.4MG frequency for the field in the a direction splits into two branches if the field is rotated away from \hat{a} . C11 and B17 are therefore due to central orbits on the butterfly, with minimal cross-sectional area. The maximum orbit for the field in the \hat{a} direction gives a frequency of 23.8 MG, which is larger than the 22.2MG expected. This is reasonable since the ellipsoid inside the butterfly is also larger than expected. C12 and B14 near \hat{a} are therefore due to non-central maximum orbits of the butterfly.

The origin of B18 at 28.9MG for $\bar{H}|\hat{a}$ remains unknown at this point. It was at first thought to be a harmonic of B11, but this was later discounted because B18 does not decrease fast enough with increased rotation from \hat{a} toward \hat{c} . A frequency in the ab plane corresponding to B18 was not observed, possibly because of the misorientation. A 28.9MG frequency was observed here, but this was determined to be due at least in part to the sum of C10 and C11. No higher frequencies were observed for $\bar{H}|\hat{a}$ for fields up to

56kG.

H. High Frequencies for $\bar{H} \parallel \hat{c}$

For the field in the \hat{c} direction, one finds high frequencies of 4.16MG, 8.56MG, 12.5 MG, 13.1 MG, 20.8 MG, and 22.4 MG. The 8.56MG frequency is degenerate and splits into two branches in the ac plane. The lowest of these six frequencies has been previously assigned to the 8e at L ellipsoid. The model predicts that a frequency of approximately 12.7MG, which could in fact be either of the two middle frequencies listed, should be observable due to a two-winged butterfly orbit of maximum cross-section caused by magnetic breakdown. Therefore, one must imagine in Figure 4 that the four parts of the ellipsoid-butterfly complex have been reassembled together about the point L, and that the butterfly on one side of the hexagonal face has been sheared away, leaving only the ellipsoid. It is easily seen then that if the field is rotated from \hat{c} to \hat{a} , this expected maximum magnetic breakdown orbit for $\bar{H} \parallel \hat{c}$ transforms continuously into the non-central maximum orbit for $\bar{H} \parallel \hat{a}$. There is magnetic breakdown required on the hexagonal face at all orientations of the field between \hat{c} and \hat{a} except for those fields within approximately 4° of \hat{a} , at which angles the extremal orbit of maximum area (a maximum orbit) is contained entirely on the butterfly on one side of the hexagonal face of the zone. Since B14 has been

identified as being due to the non-central maximum orbit for the field near \hat{a} , it must also be due to the two-winged butterfly orbit caused by magnetic breakdown for the field near \hat{c} . This also identifies A10 near \hat{c} since both have a frequency of 13.1 MG for $\bar{H} \parallel \hat{c}$. The frequency due to the four-winged butterfly orbit for $\bar{H} \parallel \hat{c}$ is then expected to be approximately twice the two-winged butterfly frequency less the ellipsoid frequency, or 22.1 MG. This is close to the 22.4 MG frequency actually observed for A11' and B15'.

For the remaining three frequencies in this direction there are at least two different explanations, neither of which is completely satisfactory. For the first explanation, one notes that if the field is rotated from \hat{c} toward \hat{a} , the non-central monster orbits expected near $k_z' = \pm k_c$ are no longer equivalent, whereas a rotation from \hat{c} toward \hat{b} does not disturb this degeneracy. Therefore one assigns A9, B12, and B13, all of which have a frequency of 8.56MG for $\bar{H} \parallel \hat{c}$, to the non-central monster orbits. This leaves only A10' and B14' at 12.5 MG for $\bar{H} \parallel \hat{c}$ as the central magnetic breakdown orbit between the monster and 5h at X, and leaves A11 and B15 at 20.8 MG for one of the central double monster orbits at $k_z = 0$. If the latter pair of frequency branches were due to the back-to-back double monster orbits, then this theory would explain Goldstein and Foner's observation that their branches XI and XVI (which are A10 and B14 here) near the c axis were reduced in amplitude whenever their sheets

XV and XVII (here A11 and B15) were present. Their resolution was not sufficient to distinguish A10' and B14' from A10 and B14, and it was observed in this study that the former pair were the stronger frequencies. Therefore, under this supposition, their observation of their sheets XI and XVI (A10' and B14') due to magnetic breakdown between the monster and 5h at X reduces the probability of an observation of their sheets XV and XVII (A11 and B15) due to the double monster orbit with no magnetic breakdown, and vice-versa.

There are two major problems with this explanation. The first is that this identifies the double monster orbit as having a frequency of 20.8 MG, and it identifies the monster-5h at X breakdown orbit as having a frequency of 12.5 MG. It therefore forces one to conclude that 5h at X should have a frequency of approximately 4.2 MG at this orientation. This is more than an order of magnitude too large. The second problem is that if the fields is rotated from \hat{c} toward \hat{a} , one of the non-central monster orbits B12 or B13 is expected to die quickly due to the interference of the monster leg with the plane of the orbit. This is not seen. The first problem could be relieved by removing the assumption that the 20.8 MG frequency was due to the double monster orbit, but that makes the explanation of Goldstein and Foner's observation unsatisfactory, and it does not remove the far more serious second problem.

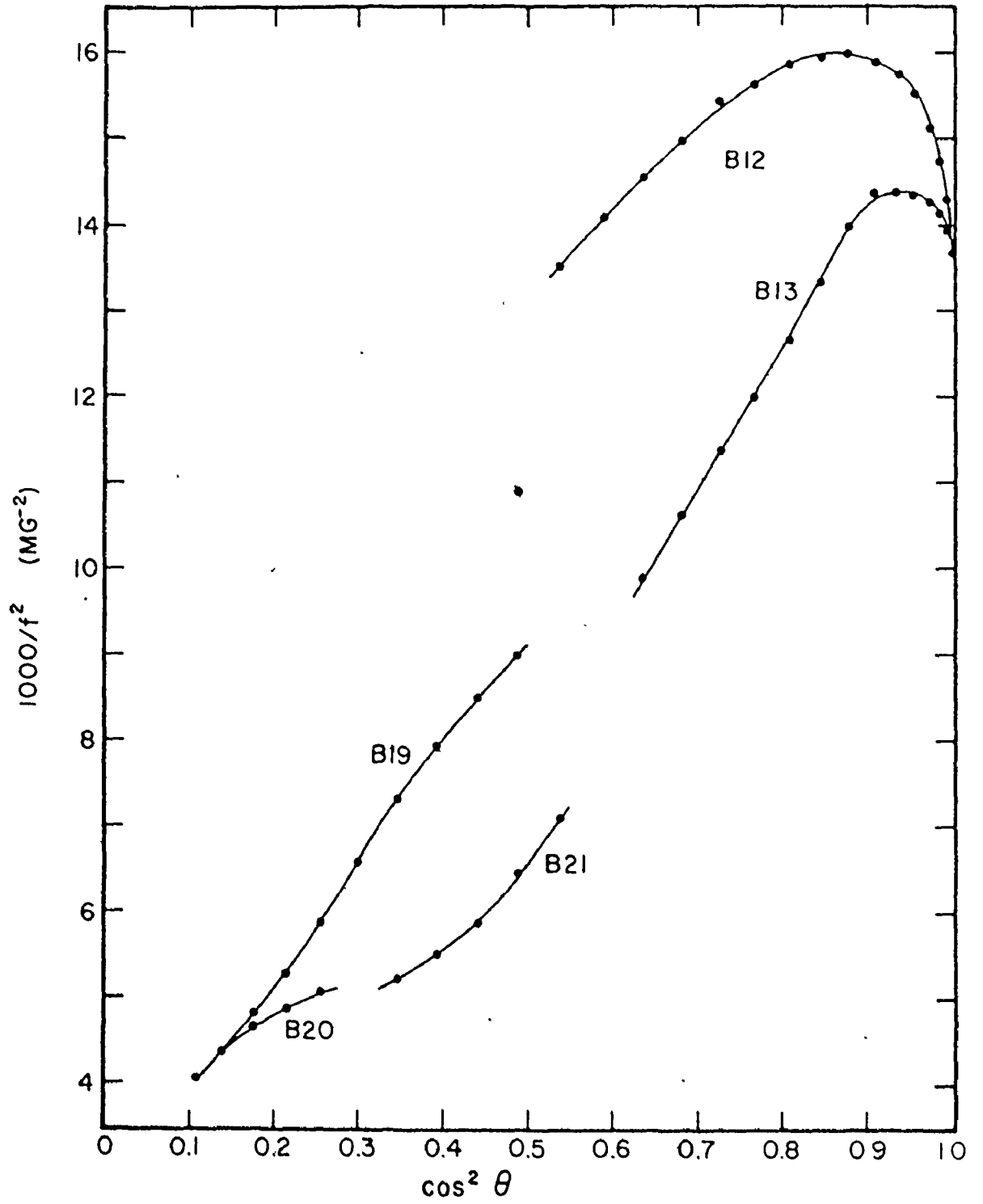
The other method of explaining the frequencies for $\bar{H} \parallel \hat{c}$ is to assign the 8.56MG frequency to the central monster breakdown orbit, as Reed suggests, leaving the 12.5 MG frequency for the non-central monster orbits, and the 20.8 MG frequency for one of the central double monster orbits, either with or without magnetic breakdown. Reed justifies the assignment with a series of convincing arguments involving open orbits with magnetic breakdown. The problem with this explanation is that since the 8.56MG frequency is now assigned to a central orbit, there is no possibility of its splitting into two frequencies if the field is rotated toward \hat{a} , and it provides no explanation of Goldstein and Foner's observations concerning the higher frequency amplitudes. Also, the 8.56MG frequency is better observed at intermediate fields, rather than high fields, which means that magnetic breakdown is more likely to destroy this orbit than create it. The resolution of this problem will have to await either a better calculation which finds the cross-section of the model at all angles, or more extensive data combined with a good imagination.

For the field between \hat{a} and \hat{c} , several frequency branches were observed, but the calculations concerned themselves only with cross-sections in symmetry planes and thus could not predict these branches. It would appear from Figure 8 that B20 and B21 might be continuations of B13 for which certain angular ranges of the field, for reasons

unknown, do not support extremal orbits. However, if one applies the distorting influence of a $1/f^2$ plot, as shown in Figure 30, this does not appear to be likely. B13 shows a definite linear region on this plot which does not extrapolate to meet B21. It is likely that B20 and B21 are due to the same surface, but there is definitely no connecting data since B20 definitely showed sharp cutoffs at both ends of its range, as shown in Appendix C. It is quite likely that most of these branches would be due to orbits on the monster, but an exact assignment cannot be made at this time. Possibilities for simple extremal orbits for the field between \hat{a} and \hat{c} are 1) an orbit encompassing both arms above the point at which they join the rest of the monster, 2) an orbit encompassing two arms and two legs similarly, 3) an orbit encompassing two arms and four legs for the field near \hat{a} . These last two types of orbits would have strong U shapes since the monster is hollow, and this makes frequency estimation difficult. For higher fields one might also have magnetic breakdown between the various pieces causing field dependent orbits. This may occur between the butterfly and the monster arms throughout most of the length of either, between the monster arms and the electron piece between them, or between the monster and the electron piece near Γ .

Figure 30. $1/f^2$ plots for B12-13 and B19-21.

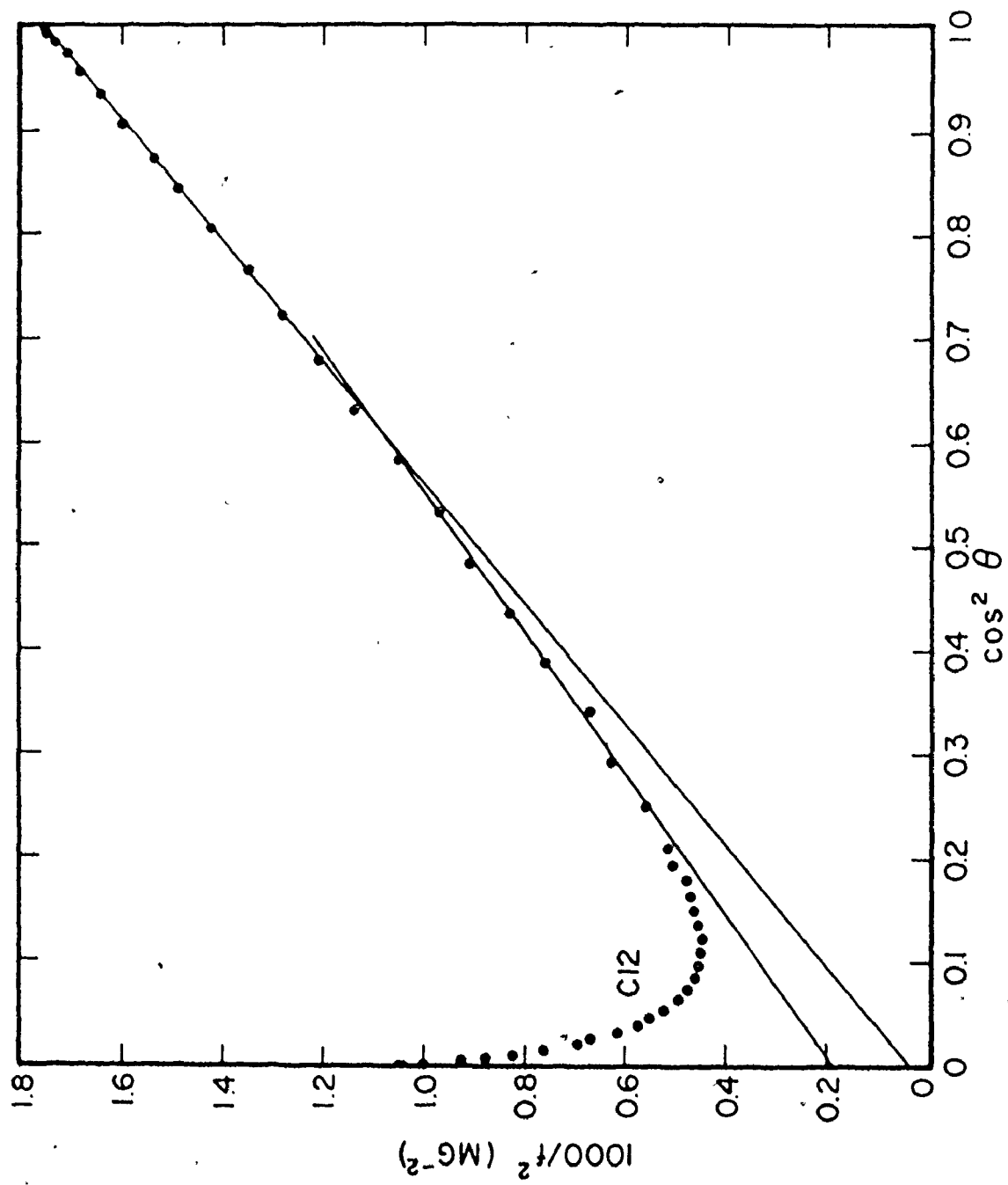
The former are probably attributable to monster orbits, but the origins of the latter are unknown.



I. High Frequencies for $\bar{H} \parallel \hat{b}$

We turn now to a consideration of those high frequencies found for the field near \hat{b} . This is the most complicated region as there are fully a dozen high frequencies either at or near \hat{b} to be explained, only a couple of which have been observed before. C8 and A5 have been included in the low frequencies, and C10 and A8 have been assigned to the eighth-band electron ellipsoid at L. It was mentioned that C12 and A10 are due to the butterfly, but the exact orbit has not yet been established for $\bar{H} \parallel \hat{b}$. To do this, consider again the reassembled butterfly with half of it sheared away, leaving half a butterfly and half an ellipsoid. Starting with a central cross-section normal to \hat{c} , if the field is rotated to \hat{b} one sees that this maximum cross-section due to magnetic breakdown transforms continuously into the central breakdown orbit for $\bar{H} \parallel \hat{b}$. Similarly, if one starts with the non-central maximum orbit in the plane normal to \hat{a} , this also transforms into the central breakdown orbit for $\bar{H} \parallel \hat{b}$, with the largest orbit occurring when the field is normal to the wing at approximately 70° from \hat{a} toward \hat{b} . Between \hat{a} and \hat{b} , therefore, C12 must change its character from non-central to central. An estimate of where this occurs can be obtained from the $1/f^2$ plot for C12 in Figure 31. It is seen that the data fits two straight lines, depending upon the range of angles considered, even though this piece is clearly not ellipsoidal in shape. The angle

Figure 31. $1/f^2$ plot for Cl2, attributed to the butterfly at L.



common to both lines occurs at $\cos^2\theta = 0.6$ or $\theta = 39^\circ$. This is approximately the angle at which the minimum central orbit C11 disappears. Therefore, it would appear that for $\theta_{ab} < 39^\circ$, C12 is a non-central orbit, and for $\theta_{ab} > 39^\circ$, C12 is a central orbit. It remains a maximum orbit throughout, so that the central orbit changes character from minimum to maximum as the field is rotated.

Since the ellipsoid has a maximum central orbit for $\vec{H} \parallel \hat{b}$ with a frequency of 24.5 MG, and the butterfly and ellipsoid have a central breakdown orbit for $\vec{H} \parallel \hat{b}$ with a frequency of 30.9 MG, the central minimum orbit of the butterfly is expected to have a frequency of approximately 37.2 MG. C17 has a frequency of 37.1 MG, so C17 and A18 are assigned to the central minimum orbit of the butterfly. If the field is rotated from \hat{b} toward \hat{a} , this central minimum is expected to increase sharply, as is seen in C17. If the field is rotated from \hat{b} toward \hat{c} , there will be two competing effects. First, the central orbit will be intersecting the wings, which results in a higher frequency, as is seen in A18. But then the orbit must eventually decrease in area since if the field is rotated far enough, this orbit becomes the four-winged butterfly orbit, which has a lower frequency. This is also seen in A18.

Of the highest frequencies for $\vec{H} \parallel \hat{b}$, C20 and A20 at approximately 58MG are matched with the double monster orbit which was expected to have a frequency of 52MG. This

association is done primarily on the fact that these branches exist only over a very narrow angular range, 3° toward \hat{a} and $4\frac{1}{2}^\circ$ toward \hat{c} . For the latter orientation, the plane of the orbit has already slipped off the backbone of the monster, so it is reasonable that the frequency should decrease. However, no further evidence is available to support this assignment.

C19 and A19 are assigned to the non-central maximum butterfly orbit for $\bar{H} \parallel \hat{b}$. These have a frequency at \hat{b} of approximately 48MG, whereas 42.6MG was expected, which is considerably lower. However, the angular variation is basically correct. If the field is rotated toward \hat{c} , this non-central orbit will eventually become the four-winged butterfly orbit for $\bar{H} \parallel \hat{c}$, so A19 must decrease sharply to join A18. If the field is rotated toward \hat{a} , the orbit will encompass a greater portion of one wing, which will cause the frequency to increase, and a lesser portion of the other, causing a decrease. The result is nearly indeterminate with the increase slightly predominating. This is precisely the behaviour observed.

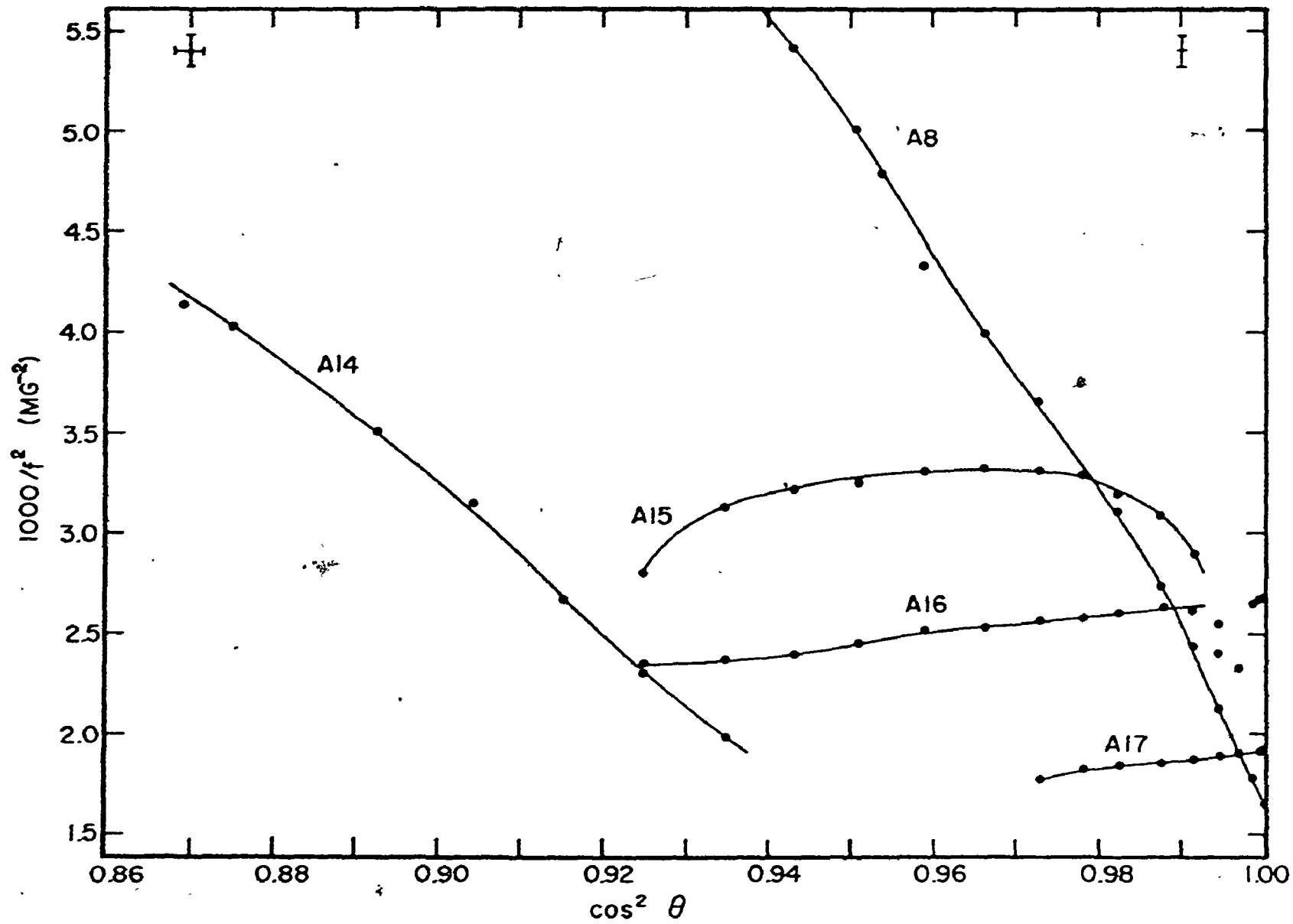
This leaves C18 yet to be explained, but no further large extremal orbits were predicted for this orientation. Figure 23 shows that the bulge in the side of the monster extends beyond the point at which the monster legs are joined to the body. It also shows that one can find a plane normal to \hat{b} which is between this point and the plane

$k_y = 0$, yet also intersects the monster at a point where the two legs join without also intersecting the monster arms. Also, Figure 22 shows that this plane could in addition be adjusted so as not to intersect the two contractions in the monster's side near where the legs join. Therefore, it may be possible for an orbit to traverse the outside of the side of a monster, the inside of his legs (crossing to the inside very near the point at which they are connected to the monster body), cross to the adjoining monster on the inside of the legs, and continue to the outside of that monster's side. The orbit is then closed in an identical manner. An extremely rough estimate of the size of this orbit, considered to be roughly elliptical with the lengths of the axes determined by the distance of the bulge from the plane $k_x = 0$ and the distance from the plane $k_z = 0$ to the inside corner of the legs in the plane $k_x = 0$, gives a frequency of 47MG. This is of the correct order of magnitude to explain C18, although the exact value is subject to gross errors. If this is the correct extremal orbit, and it is the contention of this study that it is, then one would expect that if the field is rotated from \hat{b} toward \hat{a} , the orbit would climb higher on the back of one monster, but would change very little on the other monster, resulting in a sharply increasing frequency. This is exactly the behaviour seen in C18. Also, if the field were rotated from \hat{b} toward \hat{c} , then this orbit is expected to disappear quickly,

since the fortuitous alignment described in Figure 23 and in Figure 22 would be destroyed. Since the latter figure shows a much more restrictive condition, it is estimated from Figure 22 that a rotation of not more than 1° would be sufficient to destroy the orbit. Since the angular mesh in the bc plane near \hat{b} was 1.1° , it is unlikely that this frequency could have been seen, especially since C18 is of weak amplitude near \hat{b} , except by extreme good luck, since a maximum of two observations could be expected, and these may not be correlated. It is therefore reasonable that a frequency due to this orbit was not observed in the bc plane. Also, the fact that this orbit was observed in the ac plane shows that this crystal was accurately aligned near \hat{b} in this plane, even if there was an error near \hat{a} .

We consider now those remaining high frequencies below a frequency of 25MG. The first problem for this region is to identify the various branches. To this end, the distorting influence of a $1/f^2$ plot was used, as shown in Figure 32. Since this is a highly enlarged plot, error limits of $\pm 0.2^\circ$ in angle and ± 0.1 MG in frequency are indicated in the upper left and right corners. As can be seen, this type of plot does identify which points belong to which branches except for those few points near A15 and A16 for θ_{bc} near 0° . It has already been shown that frequencies near \hat{b} are extremely sensitive to exact orientation, and it appears that here is another example

Figure 32. $1/f^2$ plots for A8 and A14-17. The first and last are attributed to orbits in the ellipsoid-butterfly complex at L, but the origin of the other three branches is unknown. Error limits of $\pm 0.2^\circ$ in angle and $\pm 0.1MG$ in frequency are shown in the upper left and right corners.



of that sensitivity. More data will be needed for this region before this data can be adequately described. The frequency listings for this region in Appendix C are therefore quite arbitrary.

Of the remaining data, C16 and A17 have been assigned by Reed to the non-central magnetic breakdown orbit between $8e$ at L and the butterfly. The frequency at \hat{b} of 22.9MG is less than half the frequency of approximately 48MG associated with the non-central maximum butterfly orbit for $\bar{H}|\hat{b}$. It would appear, therefore, that the breakdown orbit is shifted toward the $k_y = 0$ plane from the orbit forming the maximum on the butterfly. Except for this minor discrepancy there is no reason to doubt this assignment. For C14 and C15 there are two possible ways of examining the data. The first is to assume that C15 is the continuation of C14 in the same manner that B17 is the continuation of B11. A15 and A16 would then correspond to C10 and C11. In other words, one would look for two nested surfaces of the right size which appear to be like the ellipsoid-butterfly complex near the hexagonal face of the zone, but with the exception that the orientation is normal to \hat{b} rather than \hat{a} . This does not lead to fruitful results using Reed's model. The other way is to analyze C14 and C15 in the same manner as C2-5 and B8-9 were analyzed. A shifting angle of 48.4° leads to a nearly straight line except for those data points near the ends of the line. The deviation here is outside experimental

error so that this also fails to give satisfactory results. It should be noted, however, that C14 does have an extremely sharp cutoff at $\theta_{ab} = 62^\circ$, which indicates a change in connectivity of the piece forming this orbit at that angle. Finally, C13 was observed at only a single orientation, and although A13 was observed over a 7° range, it was also one of the weakest signals observed. A13 did not vary sufficiently to claim it to be half the frequency of A17, and no other assignment was possible.

For the field between \hat{b} and \hat{c} , only one additional frequency (A12) was observed. This was observed without comment by Goldstein and Foner, and neither was it identified by Reed. This study presents better data for this branch, but will have to leave it unidentified except for the fact that it is more likely to be on the monster than on the butterfly whose orbits are reasonably well known. This tentative placement is also supported by the fact that if A12 is extrapolated toward both the \hat{b} and \hat{c} directions in a $1/f^2$ plot, the extrapolation nearly coincides with A9, and intersects the b axis at a frequency of 40.8MG, which is nearly the frequency of C18 at that direction. C18 was associated with an orbit along the monster legs and side, and A9 was associated, however unsatisfactorily, with either a central or non-central monster orbit.

J. Additional Topics

Since this study was concerned primarily with a frequency analysis of the dHVA data, using Reed's model as a basis for the analysis, little more can be said. The data analysis program was designed to yield a rough estimate of magnetic breakdown threshold fields (i.e. magnetic field strengths at which magnetic breakdown effects become appreciable), but little evidence was seen favouring magnetic breakdown using this analysis. This is probably due to this part of the program being too crude.

Effective masses are usually extractable from dHVA data by investigating the temperature dependence of the amplitude of a given frequency at a given field. It can be shown from the analysis of section II that if one plots $\ln(A/T)$ vs. T , where A is the frequency amplitude at constant field, then one should observe a nearly linear relation, the slope being proportional to the effective mass. One then uses an iteration procedure to obtain a more accurate value, using the effective mass at one stage of the analysis as a correction for the next stage. Since the temperature dependence was not investigated, this analysis could not be done. However, effective masses could also be extracted from a harmonic content analysis under certain circumstances. These circumstances are that one or more of the harmonics must be observed to be missing, and a higher harmonic observed to be

present. In that case, the effective mass term $\cos(r\pi g^*/2m)$ in equation (19) must be zero for the missing harmonic. Only one case of this occurring was observed in this study, and that was the case of A4, A7, C9, and C9' for \bar{H} near \hat{b} , but the supporting data here is somewhat tenuous. The data showed a dominant 0.335MG frequency listed as due to 6h at T, and a weak signal at 0.713MG listed as the second harmonic of a frequency due to 7e between arms. But it also showed a strong frequency at 0.344MG, and a region of relatively high noise centred approximately at 0.358MG. The 0.344MG frequency was found to be due to the Bessel function, which simulated what the Fourier transform algorithm considered to be a beat frequency. The noise region is approximately half the 0.713MG frequency, which would lead one to believe that the fundamental frequency might be present, although extremely weak. In any case, one can say that the effective mass cosine term in (19) is near 0 for the fundamental, and near 1 for the second harmonic, especially since the other factors in (19) attenuate the second harmonic signal far more than the fundamental, yet the second harmonic was observed and the fundamental was not observed. Therefore, one has $g^*/m = 1 + 2n$, where n is an integer, for this orbit of the 7e between arms piece. Further determination of either g or m^* must now await more data since it is nearly impossible to correlate effective masses found in cyclotron resonance experiments with dHVA frequencies without an estimate of the

effective masses expected from each Fermi surface piece.

TABLE 3

Observed Frequency Assignments in Reed's Model

A1 Monster Arm: $k_y > 0$	B1 Monster Arm: $k_x < 0$	C1
2 " " : $k_y > 0$	2 " " : $k_x < 0$	2 7e/8e at N
3 5h at X	3 5h at X	3 "
4 7e between Arms	4 7e between Arms	4 "
5 7e near Γ	5 7e near Γ	5 "
6 6h at T	6 6h at T	6 Monster leg
7 7e between Arms (2 nd harmonic)	7	7 6h at T
8 8e at L	8 7e/8e at N	8 7e near Γ
9 Monster*	9 "	9 7e between Arms (2 nd harmonic)
10 8e at L/2-wing Butterfly (MB, central)	10 Monster leg	9' 7e between Arms
10' Monster/5h at X (MB)	11 8e at L	10 8e at L
11 double Monster	12 Monster*	11 Butterfly (central)
11' 4-wing Butterfly	13 " *	12 Butterfly (a: non-central b: central, MB to 8e at L)
12 Monster	14 Butterfly (a: non-central, c: central, 2-wing MB to 8e at L)	13
13	14' Monster/5h at X (MB)	14
14	15 double Monster*	15
15	15' 4-wing Butterfly	16 Butterfly/8e at L (MB, non-central)
16	16	17 Butterfly (central)
16	17 Butterfly (central)	17 Butterfly (central)

TABLE 3(cont.)

A17 Butterfly/8c at L (MB, noncentral)	B18	C18 Monster side (non-central)
18 Butterfly (central)	19	19 Butterfly (non-central)
19 Butterfly (non-central)	20	20 double Monster
20 double Monster	21	* 21
	22	

* uncertain assignment

MB = magnetic breakdown orbit

CHAPTER VI
CONCLUSIONS

This study has two purposes. The first is to accurately measure the dHvA frequencies of gallium, since previous experiments have been unable to do so. The second purpose is to determine how close Reed's model comes to explaining reality. To that end, we now summarize the evidence obtained here both for and against each piece of Reed's model, as well as evidence for which Reed's model provides no explanation.

The sixth-band hole surface at T (6h at T) appears to be well confirmed. This piece was manufactured phenomenologically in Reed's calculations, but all evidence to date supports its existence. The measured extremal cross-sections and the radii calculated from them differ from those values expected from Reed's model by at most 8%, which is not unreasonable.

The seventh-band electron surface near Γ (7e near Γ) is also well documented. The model does not give the correct size, its cross-sections normal to \hat{a} , \hat{b} , and \hat{c} being 21% low, 4% low, and 7% high respectively, so that this piece is considerably longer in the \hat{c} direction than predicted. But it does predict the fact, experimentally observed here for the first time, that this piece is curved toward the \hat{b} direction at both of its $\pm\hat{c}$ direction extremities. The

same curvature is not shown at its \hat{a} extremities.

The seventh-band electron surface between the monster arms (7e between arms) has for the first time been seen throughout one principle plane, most of a second, and part of the third, and now has been identified. The predictions of Reed's model concerning the size of this piece are considerably too high, but this is attributable to the extreme sensitivity of this piece to the Fermi energy. However, the model does predict this piece to be very flat and thin in the bc plane, and these features are observed.

Frequencies attributable to Reed's seventh-band and eighth-band electron pieces at N (7e and 8e at N) have been observed, and the frequency in the \hat{a} direction agrees with the predictions of the model. A degeneracy in the frequency due to these pieces for the field in the ab plane was observed due to a slight crystal misorientation, which shows that useful data could be obtained for these pieces for field rotations in a non-symmetry plane. Until such data is available, no further comparison between the data and these pieces of the model can be made.

Frequencies due to the fifth-band hole ellipsoid at X have been observed for the field in the bc and ac plane, but not for the field in the ab plane. This limited data appears to show that Reed's calculations give too small a surface for this piece. The absence of data in the third plane is explainable by considering the degeneracy of the point of

intersection of the orbits for this plane with the hexagonal face of the zone.

Low frequencies attributed to the monster arms and legs have also been observed. The primary supporting arguments for these assignments are the angular variation and angular extent of these frequencies. The six frequency branches observed (four from the arms and two from the legs) die at various field rotation angles from \hat{c} (for the arms) or \hat{a} (for the legs), all of which can be accurately correlated with Reed's model. Reed's calculations for Π along symmetry directions give frequencies 7% high for the legs, and 85% high for the arms. The former is reasonable, but the latter is not.

One extremely low frequency for $\Pi||\hat{a}$ remains yet to be explained. The data for this is not extensive enough to make any assignment possible, but if it is believable, Reed's model cannot explain it since there are no more small Fermi surface pieces left to be assigned.

The eighth-band electron surface at L (8e at L) has been observed for the first time, and the extremal dimensions predicted by the model for this piece are at worst 7% different from those observed, which is not unreasonable. However, the shape of this piece, as calculated from this study, shows significant deviations from the ellipsoidal shape expected from Reed's model.

A multitude of frequencies have been observed which are

attributable to the butterfly or the ellipsoid-butterfly complex at L. Most of these are either new, or, if previously observed, have been correctly identified for the first time. All frequencies expected for this complex from Reed's model, whether central or non-central, with or without magnetic breakdown, have been observed, and all frequencies were close enough to the model's expectations, in both magnitude and angular variation, and to some degree in angular extent, to conclude that this part of the model has basically the right size and shape. Exact numerical comparisons, however, between this piece and the data must await a model calculation which yields all cross-sections normal to the field for all field directions.

An interesting point brought out by this study is that for $\hat{H}||b$ a frequency attributable to a maximum non-central orbit of the butterfly, and also a frequency which appears to be attributable to a non-central orbit due to magnetic breakdown between the butterfly and the ellipsoid at L, were observed. However, the latter orbit in itself is neither a maximum nor a minimum orbit, and is detected solely due to the existence of the former orbit as an extremal orbit, and the fact that the two orbits are related by magnetic breakdown. This does not violate the fact that the dHvA effect is sensitive only to extremal orbits since a prior condition on these orbits is that they be contained on a single piece of Fermi surface. This is therefore the first reasonably

certain evidence that the dHVA effect can be used to measure non-extremal magnetic breakdown orbits.

Data for the large orbits encompassing the monster surface are the least satisfactory, and this is not unexpected, for this surface changes radically between the various models mentioned here, and it has exceedingly few extremal orbits for its size and shape. For $\bar{H} \parallel \hat{a}$ no high frequencies were observed for the monster, and not more than one was expected. For $\bar{H} \parallel \hat{b}$ a central double-monster orbit was observed, and a new non-central monster orbit along the monster's side and legs was observed and identified for the first time. For $\bar{H} \parallel \hat{c}$ no monster orbits were unequivocally identified, although some frequency branches were attributed to a choice of monster orbits. This still leaves many observed high frequency branches, primarily for \bar{H} near \hat{b} , for which no explanation was found within Reed's model. This includes one frequency branch (C14) for \bar{H} in the ab plane which was the dominant observed frequency throughout most of its approximately 30° range of existence. This is a serious failure of the model.

Table 4 summarizes the data observed at symmetry directions. Entries in columns marked E are experimental frequencies measured in this study, and columns marked T contain those corresponding frequencies expected from Reed's model. Most frequencies expected have been observed, although the expectations have not always been in good agree-

ment with the data. Also, there are some frequencies at symmetry directions which Reed's model apparently does not explain.

In conclusion, Reed's model of the Fermi surface of gallium is a far superior model than has previously been calculated. It does have the proper connectivity, and it does have pieces of approximately the correct size, shape, and placement. Some of these surfaces or parts of surfaces are more easily verifiable experimentally than others, and these easily verifiable parts fit the data reasonably well. Reed's model can be used to explain fully 75% of the frequency branches observed in this study, including most major branches. However, there is still much unexplained data. The explanation for this data may lie in a thorough theoretical numerical analysis of Reed's model, an analysis which would calculate all cross-sections normal to the field for all field directions. But it is more likely that the solution of this problem lies in using Reed's model as the basis for a slightly better calculation.

TABLE 4

dHVA Frequencies at Symmetry Directions

Piece	Frequencies (MG)					
	\hat{a}		\hat{b}		\hat{c}	
	E	T	E	T	E	T
7e Butterfly (L) (central)	14.5	12.2	37.1	35.9	22.4	21.8
7e Butterfly (L) (non-central)	23.8	22.2	48.1	42.6		
7e Butterfly/8e at L (central, MB)			30.9	28.4	13.1	12.7
7e Butterfly/8e at L (non-central, MB)			22.9	21.5		
8e at L	14.5	12.2	24.5	20.9	4.16	3.94
7e near I'	.891	.704	6.94	6.65	.790	.843
6h at T	.508	.52	.335	.346	1.36	1.26
7e between Arms		5	.356	.705	.287	.468
7e at N	.263	.22		.42		.55
8e at N	.263	.22		.14		.26
5h at X		.37			.223	
6h Monster legs ($k_x=0$)	.419	.45				
6h Monster Arms ($k_x=k_y=k_z$)					.201	.37
6h double Monster (central)			57.7	52	20.8*	21.8
6h Monster/5h at X (central, MB)				26.4	12.5*	10.9

TABLE 4 (cont.)

Piece	Frequencies (MG)					
	$H \parallel \hat{a}$		$H \parallel \hat{b}$		$H \parallel \hat{c}$	
	E	T	E	T	E	T
6h Monster (non-central)			41.1		8.55*	11.2
unassigned	28.9		19.4			
unassigned			11.4			

* uncertain assignment

MB = magnetic breakdown orbit

APPENDIX

A. Field Modulation Effects

From (19) one writes the magnetization as

$$(A.1) \quad \vec{M}(\vec{H}_t) = \sum_r \vec{K}_r(\vec{H}_t) \sin[2\pi \left(\frac{F_r(\hat{H}_t)}{H_t} - \gamma_r \right) \mp \frac{\pi}{4}]$$

where $\vec{K}_r(\vec{H}_t)$ is a slowly varying vector amplitude of the r^{th} frequency component of \vec{M} , and the sum over r includes all fundamental frequencies, their harmonics, and combinations. The total field \vec{H}_t is given by

$$\vec{H}_t = \vec{H} + \vec{h} \sin \omega t \quad (h \ll H)$$

Defining the argument of the sine function in (A.1) as β_r and expanding, one has

$$(A.2) \quad \beta_r = 2\pi \left(\frac{F_r(\hat{H}_t)}{|\vec{H} + \vec{h} \sin \omega t|} - \gamma_r \right) \mp \frac{\pi}{4}$$

Expanding to lowest order in h/H :

$$\begin{aligned} |\vec{H} + \vec{h} \sin \omega t|^{-1} &= [(\vec{H} + \vec{h} \sin \omega t) \cdot (\vec{H} + \vec{h} \sin \omega t)]^{-1/2} \\ &= \frac{1}{H} [1 + 2 \frac{\vec{H} \cdot \vec{h}}{H \cdot H} \sin \omega t + \frac{\vec{h} \cdot \vec{h}}{H \cdot H} \sin^2 \omega t]^{-1/2} \\ (A.3) \quad &\approx \frac{1}{H} - \frac{\vec{H} \cdot \vec{h}}{H^2} \sin \omega t \end{aligned}$$

$$(A.4) \quad \hat{H}_t = \frac{\vec{H} + \vec{h} \sin \omega t}{|\vec{H} + \vec{h} \sin \omega t|} \approx \hat{H} + \frac{1}{H} \vec{h} \sin \omega t$$

where \bar{H}' is the component of \bar{H} normal to \hat{H} :

$$\begin{aligned} \bar{H}' &= \bar{H} - (\bar{H} \cdot \hat{H}) \hat{H} \\ (A.5) \quad &= \hat{H} \times (\bar{H} \times \hat{H}) \end{aligned}$$

Upon inserting (A.3) - (A.5) in (A.2) and defining the quantities

$$\begin{aligned} \phi_r &= 2\pi \left(\frac{F_r(\hat{H})}{H} - \gamma_r \right) + \frac{\pi}{4} \\ \lambda_r &= 2\pi F_r(\hat{H}) \frac{h}{H^2} (\hat{h} \cdot \hat{H}) \\ &\quad - \frac{1}{F_r(\hat{H})} \hat{H} \times (\hat{h} \times \hat{H}) \cdot \nabla_{\theta\phi} F_r(\hat{H}) \end{aligned}$$

where $\nabla_{\theta\phi} F_r(\hat{H})$ is the gradient of F in the plane normal to \bar{H} , one has

$$(A.6) \quad \beta_r = \phi_r - \lambda_r \sin \omega t$$

Inserting (A.6) in (A.1) and expanding:

$$\bar{N}(\bar{H}) = \sum_r \bar{K}_r(\bar{H}) [\sin \phi_r \cos(\lambda_r \sin \omega t) - \cos \phi_r \sin(\lambda_r \sin \omega t)]$$

Expanding the second factor of each term in a Fourier series:

$$\exp(i\mu \sin y) = \sum_{n=-\infty}^{\infty} J_n(\mu) e^{iny}$$

where $J_n(\mu) = (-1)^n J_{-n}(\mu)$ is the n^{th} order Bessel function of the first kind. Continuing,

$$\bar{M}(\bar{H}) = \sum_r \bar{A}_r(\bar{H}) \sum_{n=-\infty}^{\infty} J_n(\lambda_r) [\sin\phi_r \cos n\omega t - \cos\phi_r \sin n\omega t]$$

The signal one detects in the pickup is now the time derivative of \bar{M} . If one ensures that $|\frac{\delta H}{\delta t}| \ll |\frac{\delta h}{\delta t}|$, then

$$\begin{aligned} \frac{\delta \bar{M}(\bar{H})}{\delta t} &= -\sum_r \bar{A}_r(\bar{H}) \sum_{n=-\infty}^{\infty} n\omega J_n(\lambda_r) [\sin\phi_r \sin n\omega t \\ &\quad - \cos\phi_r \cos n\omega t] \\ &= -\sum_r \bar{A}_r(\bar{H}) \sum_{n=1}^{\infty} n\omega J_n(\lambda_r) [(1 + (-1)^n) \sin\phi_r \sin n\omega t \\ &\quad + (1 - (-1)^n) \cos\phi_r \cos n\omega t] \\ &= -\sum_r \bar{A}_r(\bar{H}) \sum_{n=1}^{\infty} 2n\omega J_n(\lambda_r) [\sin\phi_r \sin n\omega t \cos^2 n \frac{\pi}{2} \\ &\quad + \cos\phi_r \cos n\omega t \sin^2 n \frac{\pi}{2}] \\ (A.7) \quad &= -\sum_r \bar{A}_r(\bar{H}) \sum_{n=1}^{\infty} 2n\omega J_n(\lambda_r) \sin(\phi_r + n \frac{\pi}{2}) \\ &\quad \times \sin(n\omega t + n \frac{\pi}{2}) \end{aligned}$$

Finally, if $\bar{H} \parallel \bar{H}$, then $\lambda_r = \frac{2\pi r h}{H^2}$, and (A.7) reduces to (21).

B. Ellipsoidal Fermi Surfaces

Suppose a piece of fermi surface is in the shape of an ellipsoid with principle axes aligned in the direction of the coordinate axes:

$$(A.8) \quad \frac{x^2}{a^2} + \frac{y^2}{b^2} + \frac{z^2}{c^2} = 1$$

Let the crystal be non-aligned in the yz plane by an angle

θ_1 :

$$\begin{aligned}
 (A.9) \quad x &= x_1 \\
 y &= y_1 \cos \theta_1 - z_1 \sin \theta_1 \\
 z &= z_1 \cos \theta_1 + y_1 \sin \theta_1
 \end{aligned}$$

Define the following three quantities:

$$\begin{aligned}
 (A.10) \quad 1/b_1^2 &= \cos^2 \theta_1 / b^2 + \sin^2 \theta_1 / c^2 \\
 1/c_1^2 &= \sin^2 \theta_1 / b^2 + \cos^2 \theta_1 / c^2 \\
 1/d_1^2 &= \sin \theta_1 \cos \theta_1 (1/c^2 - 1/b^2)
 \end{aligned}$$

Expanding (A.8) with (A.9) and inserting (A.10) yields

$$(A.11) \quad \frac{x_1^2}{a^2} + \frac{y_1^2}{b_1^2} + \frac{z_1^2}{c_1^2} + 2 \frac{z_1 y_1}{d_1^2} = 1$$

Let the crystal be further non-aligned in the $x_1 z_1$ plane by an angle θ_2 :

$$\begin{aligned}
 (A.12) \quad x_1 &= x_2 \cos \theta_2 - z_2 \sin \theta_2 \\
 y_1 &= y_2 \\
 z_1 &= z_2 \cos \theta_2 + x_2 \sin \theta_2
 \end{aligned}$$

Define the following six quantities:

$$\begin{aligned}
 (A.13) \quad 1/a_2^2 &= \cos^2 \theta_2 / a^2 + \sin^2 \theta_2 / c_1^2 \\
 1/b_2^2 &= 1/b_1^2 \\
 1/c_2^2 &= \sin^2 \theta_2 / a^2 + \cos^2 \theta_2 / c_1^2 \\
 1/d_2^2 &= \sin \theta_2 / d_1^2 \\
 1/e_2^2 &= \sin \theta_2 \cos \theta_2 (1/c_1^2 - 1/a^2)
 \end{aligned}$$

$$(A.13, \text{ con.}) \quad 1/f_2^2 = \cos^2 \theta_2 / d_1^2$$

Expanding (A.11) with (A.12) and inserting (A.13) yields

$$(A.14) \quad \frac{x_2^2}{a_2^2} + \frac{y_2^2}{b_2^2} + \frac{z_2^2}{c_2^2} + 2 \frac{x_2 y_2}{d_2^2} + 2 \frac{x_2 z_2}{o_2^2} + 2 \frac{y_2 z_2}{f_2^2} = 1$$

In performing the dHVA experiment, rotate the crystal about the z_2 axis by an angle ϕ :

$$(A.15) \quad \begin{aligned} x_2 &= x_1 \cos \phi + y_1 \sin \phi \\ y_2 &= y_1 \cos \phi - x_1 \sin \phi \\ z_2 &= z_1 \end{aligned}$$

Define the following six quantities:

$$(A.16) \quad \begin{aligned} 1/\alpha^2 &= \cos^2 \phi / a_2^2 + \sin^2 \phi / b_2^2 - \sin 2\phi / d_2^2 \\ 1/\beta^2 &= \sin^2 \phi / a_2^2 + \cos^2 \phi / b_2^2 + \sin 2\phi / d_2^2 \\ 1/\gamma^2 &= 1/c_2^2 \\ 1/\delta^2 &= \sin \phi \cos \phi (1/b_2^2 - 1/a_2^2) - \cos 2\phi / d_2^2 \\ 1/\epsilon^2 &= \sin \phi / f_2^2 - \cos \phi / o_2^2 \\ 1/\eta^2 &= \sin \phi / o_2^2 + \cos \phi / f_2^2 \end{aligned}$$

Expanding (A.14) with (A.15) and inserting (A.16) yields

$$(A.17) \quad \frac{x_1^2}{\alpha^2} + \frac{y_1^2}{\beta^2} + \frac{z_1^2}{\gamma^2} - 2 \frac{x_1 y_1}{\delta^2} - 2 \frac{x_1 z_1}{\epsilon^2} + 2 \frac{y_1 z_1}{\eta^2} = 1$$

The magnetic field \vec{H} is assumed to be in the \hat{x}_1 direction. Therefore, for a given value of x_1 , one finds the cross-section of the ellipse defined by (A.17) by finding the

major and minor radii m_1 and m_2 of the ellipse. The area is then $\pi m_1 m_2$. To do this, one conceptually rotates the crystal in the y, z , plane by an angle λ , and then adjusts λ to eliminate the $y_4 z_4$ cross-term:

$$(A.18) \quad \begin{aligned} x_4 &= x_4 \\ y_4 &= y_4 \cos \lambda + z_4 \sin \lambda \\ z_4 &= z_4 \cos \lambda - y_4 \sin \lambda \end{aligned}$$

Inserting (A.18) in (A.17) one finds that the coefficient of $y_4 z_4$ is

$$2 \sin \lambda \cos \lambda \left(\frac{1}{\beta^2} - \frac{1}{\alpha^2} \right) + \frac{2}{\eta^2} (\cos^2 \lambda - \sin^2 \lambda) = 0$$

Therefore,

$$(A.19) \quad \tan 2\lambda = \frac{2/\eta^2}{1/\gamma^2 - 1/\beta^2}$$

From this one may find $\sin^2 2\lambda$ and $\cos^2 2\lambda$; λ itself will not be needed here. Define the following four quantities:

$$(A.20) \quad \begin{aligned} 1/r^2 &= \cos^2 \lambda / \beta^2 + \sin^2 \lambda / \gamma^2 - 2/\eta^2 \sin \lambda \cos \lambda \\ 1/s^2 &= \sin^2 \lambda / \beta^2 + \cos^2 \lambda / \gamma^2 + 2/\eta^2 \sin \lambda \cos \lambda \\ 1/t^2 &= \cos \lambda / \delta^2 - \sin \lambda / \epsilon^2 \\ 1/w^2 &= \sin \lambda / \delta^2 + \cos \lambda / \epsilon^2 \end{aligned}$$

Expanding (A.17) with (A.18) and inserting (A.20), allowing for the fact that there will be no term in $y_4 z_4$, yields

$$y_4^2/r^2 + z_4^2/s^2 - 2x_4 y_4/t^2 - 2x_4 z_4/w^2 = 1 - x_4^2/\alpha^2$$

i.e.

$$\frac{1}{r^2} (y_0 - x_0 r^2 / t^2)^2 + \frac{1}{b^2} (z_0 - x_0 b^2 / w^2)^2 =$$

$$1 - x_0^2 (1/a^2 - r^2/t^4 - b^2/w^4) \quad (2)$$

The major and minor radii are now rc and bc , and the cross-sectional area for this value of x_0 is

$$A = \pi r b c^2 = \pi r b [1 - x_0^2 (1/a^2 - r^2/t^4 - b^2/w^4)]$$

Clearly, the maximum cross-section occurs for $x_0 = 0$.

Inserting (A.20) and (A.19) as appropriate, and using some trigonometric identities to eliminate $\sin \lambda$ and $\cos \lambda$ in favour of $\sin^2 2\lambda$ and $\cos^2 2\lambda$, one finds

$$\pi^2 / \Lambda_{\max}^2 = 1/\beta^2 \gamma^2 - 1/\eta^4$$

Inserting (A.16), (A.13), and (A.10), as appropriate, one finds

$$(A.21) \quad \pi^2 / \Lambda_{\max}^2 = \frac{1}{a^2 c_1^2} + \left(\left(\frac{1}{b^2 c_1^2} - \frac{1}{a^2 c_1^2} \right) + \left(\frac{1}{b^2 c_1^2} + \frac{1}{a^2 b^2} \right) \sin^2 \theta_2 \right)$$

$$\times \cos^2 \phi + \frac{2}{a^2 d_1^2} \sin \phi \cos \phi \sin \theta_2$$

If θ_2 is small, then this becomes

$$(A.22) \quad \pi^2 / \Lambda_{\max}^2 \approx \frac{1}{a^2 c_1^2} + \left(\frac{1}{b^2 c_1^2} - \frac{1}{a^2 c_1^2} \right) \cos^2 \phi$$

Since the dHVA frequencies are proportional to the extremal cross-sectional areas, a plot of inverse frequency squared vs. $\cos^2 \phi$ (ϕ being the dHVA rotation angle) will

always yield a straight line for a true ellipsoid provided the plane of the diVA rotation contains at least one of the ellipsoid axes.

C. Frequency Table

On the following pages in Table 5 is presented all the data taken during the course of this study. This is a table of frequencies observed and an approximate measure of their amplitudes as a function of branch number and magnetic field orientation in the three principle planes of gallium. A full description of this table is given in Chapter IV of the text. All angles are in degrees, and frequencies are in MG.

θ_{bc}	A1	A2	A3	A4	A6	A7
± 0.2	$\pm .0008$	$\pm .0008$	$\pm .0008$	$\pm .002$	$\pm .0008$	$\pm .002$
0.0					D .3404	
2.6					D .3418	
5.3					D .3439	W .720
7.9					D .3444	W .719
10.6	W .8232		W .7201		D .3483	W .720
13.2	W .6158				D .3498	W .713
15.9	W .5430				D .3546	
20.1	W .4456			W .343	D .3634	W .683
21.2	W .4303		W .5149	W .343	D .3645	
23.8	W .3976		W .4771	W .342	D .3703	W .680
26.5	M .3644			W .336	D .3775	W .669
29.1	M .3362		W .4090		D .3866	W .664
31.8	M .3126			W .324	D .3980	W .642
34.4	M .3003		W .3630	M .324	D .4046	
37.1	S .2851		W .3486	M .320	D .4176	W .635
39.7	S .2693	W .3374		M .314	D .4333	W .626
41.3	S .2637	M .3318		M .317	D .4391	W .634
43.4	S .2556	M .3161		W .309	D .4529	W .617
43.9	S .2532	S .3146			D .4557	
45.0	S .2487	S .3064			D .4644	
46.6	S .2419	D .2970	D .2970	M .310	S .4779	W .609
47.6	S .2402	D .2929	D .2929	M .304	S .4847	W .607
49.2	S .2339	D .2848	D .2848	W .306		W .608
50.3	S .2326	D .2825	D .2825	W .301	M .5048	W .604
51.9	M .2291	D .2765	D .2765	W .304	M .5177	W .608
52.9	S .2259	D .2701	D .2701	W .299	M .5371	W .597
54.5	S .2236	D .2684	D .2684	W .302	M .5392	W .600
57.2	S .2179	S .2526	D .2601	W .299	M .5880	W .592
59.8	S .2130	S .2445	D .2527	W .296	M .6188	W .590
62.5	S .2105	S .2405	D .2486	W .294	M .6399	W .587
65.2	S .2069	S .2331	D .2430	W .295	M .6956	W .585
67.8	S .2051	S .2273	D .2390	W .292	M .7496	W .582
70.4	S .2021	S .2200	D .2340	M .292	W .8091	W .582
73.1	S .2003	S .2164	D .2308	M .291	W .9053	W .578
75.7	S .1999	S .2128	D .2289	M .290	W .9870	W .585
78.4	S .1989	S .2094	D .2268	M .289		W .582
80.5	S .1991	S .2081	D .2257	M .289	W 1.1665	W .577
83.1	S .1994	S .2066	D .2247	M .289	W 1.2794	W .575
85.8	M .1989	S .2042	D .2240	M .288	W 1.3332	
88.4		S .2011	D .2236	M .289	M 1.3626	W .571

θ bc	A5	A8	A10	A12	A13	A14
± 0.2	$\pm 0.06, .0008$	$\pm 0.1, .06$	± 0.1	± 0.1	± 0.1	± 0.1
0.0	W 6.94	W 24.6	D 31.0		W 11.5	
1.1	W 6.93		S 30.9		W 11.4	
2.1	W 6.92	W 23.7	S 30.7		W 11.5	
3.2	W 6.87	D 22.9	S 30.5		W 11.5	
4.2	W 6.84	W 21.7	M 30.2		W 11.5	
5.3	W 6.76	M 20.3	D 29.8		W 11.6	
6.4	W 6.76	W 19.1	D 29.5		W 11.6	
7.6	W 6.56	W 18.0	D 29.0			
8.5		M 17.4	D 28.7			
9.5	W 6.26	W 16.5	D 28.4			
10.6		W 15.8	D 28.0			
11.7		W 15.2	D 27.6			
12.4	W 5.52	M 14.5				
12.8		W 14.1	D 26.9			
13.8		W 13.5	D 26.6			
14.8	W 4.90	W 13.1	D 26.1			M 22.4
15.9		W 12.4	D 25.6			M 20.8
16.9		W 11.8	D 25.1			M 19.4
18.0		W 11.4	D 24.7			W 17.8
19.1			D 24.3			W 16.9
20.1	M 3.10	M 10.6				
20.7			D 23.8			W 15.7
21.2		W 10.3	D 23.6			W 15.5
22.2		W 9.99	D 23.2			
22.8	M 2.54	M 9.67	D 22.9			
23.3		W 9.46	D 22.6			
24.4		W 9.17	D 22.3			
25.4	M 2.05	M 8.69	D 21.8	W 18.2		
26.5			D 21.5			
28.1	M 1.80	M 8.06	D 20.7	W 16.8		
30.7	M 1.66	M 7.65	D 20.1	M 15.9		
33.4	M 1.53	M 7.18	D 19.3	M 14.9		
36.0	M 1.40	M 6.70	D 18.5	M 13.9		
38.7	S 1.26	W 6.27	D 17.8	M 13.1		
41.3	M 1.2186	W 6.04	D 17.3	M 12.5		
43.9	M 1.1492	W 5.75	D 16.8	M 12.0		
46.6	M 1.0822	W 5.49	D 16.2			
49.2	M 1.0325	W 5.27	D 15.7			
51.9	M 1.0044	W 5.15	D 15.4			
54.5	M .9731	M 5.00	D 15.1			
57.2	M .9345	M 4.84	D 14.7			
59.8	M .9068	M 4.70	D 14.4			
62.5	M .8896	M 4.63	D 14.3			
65.2	M .8694	M 4.54	D 14.0			

0 bc	A5	A8	A9	A10	A10'	A11	A11'
±0.2	±.0008	±0.06	±0.06	±0.1	±0.1	±0.1	±0.1
67.8 S	.8519	M 4.46	W 9.41	D 13.8			
70.4 S	.8341	M 4.37	W 9.15	D 13.6		W 21.7	
73.1 S	.8225	M 4.32		D 13.5		M 21.5	
75.7 S	.8137	M 4.28	W 8.82	D 13.4		M 21.3	
77.8			S 8.73			M 21.2	
78.4 S	.8052	W 4.23	D 8.69	D 13.3		S 21.1	
80.5 S	.8016	M 4.19	D 8.64	D 13.2	W 12.6	S 21.0	
83.1 S	.7960	W 4.18	S 8.57	S 13.2	M 12.5	D 20.9	
85.8 S	.7915	M 4.16	S 8.56	S 13.2	M 12.5	D 20.9	
88.4 S	.7906	M 4.17	S 8.55	S 13.1	S 12.5	D 20.8	M 22.4
34.4 W	1.4463						
37.1 M	1.3429						
39.7 M	1.2401						
43.4 M	1.1546						
45.0 M	1.1161						
47.6 S	1.0646						

θ_{bc}	A15	A16	A17	A18	A19	A20
± 0.2	± 0.1	± 0.1	± 0.1	± 0.1	± 0.1	± 0.1
0.0		M 19.3	S 22.8		M 48.4	M 58.8
1.1		S 19.4	D 22.9		M 48.3	M 58.3
2.1		W 19.4	D 22.9	W 37.6	M 47.9	W 57.1
3.2	W 20.7		D 22.9	W 38.3	W 47.4	W 56.0
4.2	M 19.8	S 20.4	D 23.0	M 38.9	M 46.9	
5.3	M 18.6	M 19.6	S 23.1	S 39.3	M 46.2	
6.4	M 18.0	M 19.5	M 23.2	M 39.7	W 45.2	
7.6	M 17.7	M 19.6	M 23.3	M 40.0	W 44.1	
8.5	M 17.4	M 19.7	M 23.4	M 40.1		
9.5	M 17.4	M 19.8	W 23.7	M 40.1		
10.6	M 17.3	M 19.9		M 40.1		
11.7	M 17.4	M 19.9		M 40.0		
12.8	M 17.6	W 20.2		M 39.8		
13.8	W 17.6	W 20.4		M 39.5		
14.8	W 17.9	W 20.6		M 39.3		
15.9	W 18.9	W 20.6		W 38.9		
16.9				W 38.4		
18.0				W 38.0		
19.1				W 37.6		
20.7				W 37.0		
21.2				W 36.9		
22.2				W 36.5		

θ_{ca}	B1	B2	B3	B4	B5	B6
± 0.2	$\pm .0008$	$\pm .0008$	$\pm .0008$	$\pm .0008$	$\pm .0008$	$\pm .0008$
0.6	S .2005	S .2005	D .2228	M .2867	S .7904	W 1.363
3.4	S .1980	S .2016	D .2230	M .2872	S .7911	W 1.352
6.2	M .1980	S .2041	D .2235	M .2877	S .7891	W 1.306
9.0	S .1985	S .2050	D .2248	M .2894	S .7874	W 1.255
11.8	S .1995	S .2085	D .2273	M .2944	S .7866	
14.6	S .2005	S .2119	D .2287	M .3004	S .7842	
17.4	S .2021	S .2164	D .2316	M .3040	S .7843	W 1.075
20.3	S .2049	S .2217	D .2366	M .3101	S .7842	W 1.015
23.1	S .2070	S .2268	D .2394	M .3141	D .7847	W .9566
25.9	S .2097	S .2329	D .2446	M .3216	D .7857	W .9138
28.7	S .2131	S .2408	S .2507	M .3303	D .7887	W .8684
31.5	S .2174	S .2499	S .2570	M .3382	D .7927	W .8234
34.3	S .2239	S .2589	S .2659	M .3499	D .7986	
37.1	S .2296	D .2732	D .2732	M .3619	S .8042	W .7550
39.9	S .2363	D .2841	D .2841	M .3763	S .8107	M .7259
42.8	S .2454	D .2983		M .3902	D .8176	M .6937
45.6	S .2549	S .3142	W .3054	M .4098	D .8245	M .6676
48.4	S .2671	M .3355		M .4354	D .8350	M .6439
51.2	D .2800	W .3615		M .4584	S .8423	S .6262
54.0	D .2944	W .3991		M .4894	M .8510	S .6095
56.8	D .3177		W .3737	M .5339	D .8581	S .5912
59.6	S .3401		W .3989	S .5766	D .8648	S .5766
62.4	S .3652			W .6286	D .8696	S .5643
65.3	S .3960		W .4559	W .6976	D .8749	S .5549
68.1	M .4437		W .4900		D .8793	S .5434
70.9	M .4923				D .8841	S .5350
73.7	M .5572				D .8863	S .5270
76.5	W .6432		W .6432		D .8879	S .5222
79.3			W .7012		D .8900	S .5165
82.1					D .8912	S .5135
84.9					D .8923	S .5124
88.3					D .8921	S .5098
90.6					D .8901	S .5073

0 _{ca}	B7	B8	B9	B10	B11	B12
±0.2	±.0008	±.0008	±.0008	±.0008	±.06,0.1	±.06
0.6					M 4.16	D 8.56
3.4					M 4.16	S 8.37
6.2					M 4.19	S 8.24
9.0					M 4.20	D 8.13
11.8					M 4.24	D 8.04
14.6					M 4.26	D 7.97
17.4					M 4.31	D 7.94
20.3					M 4.37	D 7.91
23.1		W .2898			M 4.45	M 7.92
25.9		W .2706			M 4.50	M 7.94
28.7					M 4.58	M 8.00
31.5					M 4.72	M 8.05
34.3					M 4.83	W 8.17
37.1					M 4.97	W 8.29
39.9		M .2178			M 5.08	W 8.43
42.8		M .2133			M 5.26	W 8.60
45.6		M .2088			M 5.46	W 9.58
48.4		S .2052			M 5.68	
51.2		S .2032			M 5.91	
54.0		S .2015			M 6.16	
56.8		S .2005			M 6.51	
59.6		S .2001			M 6.83	
62.4		S .2013			M 7.13	
65.3		S .2026			M 7.59	
68.1		M .2051			W 8.15	
70.9		M .2085			M 8.64	
73.7		M .2124		M .4563	W 9.27	
76.5		M .2157		M .4420	W 9.92	
79.3		M .2238		M .4315	W 10.8	
82.1		M .2323	W .3192	M .4266	M 11.7	
84.9		M .2416	M .2954	M .4221	W 12.6	
87.8					W 13.5	
88.3	W .1053	M .2563	M .2701	M .4197	W 13.9	
90.6	W .1053	M .2625	M .2625	M .4184	W 14.7	
93.4					W 15.9	
96.2					W 16.8	
99.0					W 18.1	

0 ca	B13	B14	B14'	B15	B15'	B16
±0.2	±.06	±0.1	±0.1	±0.1	±0.1	±.06
0.6	D 8.56	S 13.1	S 12.5	D 20.8	S 22.4	
3.4	D 8.47	S 13.1	S 12.5	D 20.8	S 22.4	
6.2	D 8.41	S 13.2	M 12.5	D 20.9	S 22.5	
9.0	S 8.37	D 13.2	M 12.6	S 20.8	M 22.7	
11.8	S 8.35	D 13.3	W 12.6	S 21.0	M 23.0	
14.6	S 8.34	D 13.3		M 21.1	M 23.5	
17.4	S 8.34	D 13.4			W 23.8	
20.3	M 8.46	D 13.6				
23.1	M 8.66	D 13.7				
25.9	M 8.89	D 13.9				
28.7	M 9.13	D 14.1				
31.5	M 9.38	D 14.3				
34.3	W 9.71	D 14.5				
37.1	W 10.06	D 14.8				
39.9		D 15.0				
42.8		D 15.4				
45.6		D 15.7				
48.4		D 16.2				
51.2		D 16.5				
54.0		D 17.0				
56.8		D 17.5				
59.6		D 18.1				W 8.84
62.4		D 18.6				W 7.47
65.3		D 19.1				M 5.81
68.1		D 19.9				M 4.42
70.9		D 20.5				W 3.19
73.7		D 21.2				W 2.31
76.5		D 21.8				
79.3		D 22.6				
82.1		D 23.3				
84.9		D 23.6				
87.8		D 23.8				
88.3		D 23.8				
90.6		D 23.8				

θ_{Ca}	B17	B18	B19	B20	B21	B22
± 0.2	± 0.1	± 0.1	± 0.1	± 0.1	± 0.1	± 0.1
42.8					W 11.9	
45.6			W 10.6		W 12.5	M 16.5
48.4			W 10.9		W 13.0	M 17.3
51.2			W 11.2		W 13.5	M 18.5
54.0			W 11.7		W 13.8	M 20.2
56.8			W 12.3			M 22.7
59.6			M 13.1	M 14.0		W 25.4
62.4			M 13.8	M 14.3		W 25.7
65.3			M 14.4	M 14.6		W 24.9
68.1			S 15.1	S 15.1		
70.9			W 15.7	W 15.7		
79.3		M 28.0				
82.1	W 17.6	M 28.6				
84.9		W 28.9				
87.8		W 28.9				
88.3	W 14.9					
90.6	W 14.4	W 28.9				
93.4	W 13.2					
96.2	W 12.4					
99.0	M 11.3					

θ_{ab}		C1	C2	C3	C4	C5	C6
± 0.2		$\pm .0008$	$\pm .0008$	$\pm .0008$	$\pm .0008$	$\pm .0008$	$\pm .0008$
0.6	M	.1069	M .2546	M .2722	M .2546	M .2778	M .4214
1.7	W	.1063	M .2502	M .2712	M .2578	M .2801	M .4207
2.8	M	.1066	M .2487	M .2687	M .2598	M .2853	M .4214
4.0	W	.1074	M .2469	M .2635	M .2635	M .2889	M .4220
5.1	W	.1078	M .2444	M .2622	M .2667	M .2956	M .4224
6.2	W	.1070	M .2432	M .2612	M .2702	M .2973	M .4230
7.4			M .2411	M .2575	M .2746	M .3045	M .4242
8.5			M .2387	M .2559	M .2804	M .3145	M .4268
9.5			M .2375	M .2530	M .2826	M .3166	M .4282
10.8			M .2370	M .2519	M .2868	M .3232	M .4292
11.9			M .2359	M .2519	M .2908	W .3283	M .4300
13.0			M .2336	M .2496	M .2947	W .3358	M .4323
14.2			M .2326	M .2492	M .3016	W .3451	M .4340
15.3			M .2323	M .2486	M .3071	W .3528	M .4387
16.4							M .4413
17.6							M .4447
18.1			M .2298	M .2470	M .3243	W .3780	
18.7							M .4488
20.9			M .2296	M .2447	W .3442	W .4179	
21.5							M .4579
23.8			M .2285	M .2448	W .3639		
24.3							M .4674
26.6			M .2282	M .2445	W .3825		
27.2							M .4845
29.4			M .2302	M .2453			
30.0							M .5035
32.3			M .2304	M .2474			
32.8							W .5193
35.1			M .2322	M .2494			
35.7							W .5495
37.9			M .2362	M .2523			
40.8			M .2396	M .2566			
43.6			M .2453	M .2629			
46.4			M .2497	M .2670			
48.7			M .2545	M .2745			
52.1			M .2636	M .2823			
54.9			M .2735	M .2941			
57.7			W .2836	W .3047			
60.6			W .2953				
63.4			W .3119	W .3349			
66.2			W .3309				

θ_{ab}	C7	C8	C9	C9'	C10	C11
± 0.2	$\pm .0008$	$\pm .0008, .06$	$\pm .002$	$\pm .002$	± 0.1	± 0.1
0.6 S	.5037	D .8917			M 13.6	W 15.4
1.7 S	.5037	D .8922				
2.8 S	.5041	D .8938				
4.0 S	.5059	D .8945			M 13.5	M 15.5
5.1 S	.5078	D .8967				
6.2 S	.5090	D .8974			M 13.4	M 15.7
7.4 S	.5112	D .8996				
8.5 S	.5130	D .9033				
9.1					M 13.4	M 16.1
9.6 S	.5141	D .9057				
10.8 S	.5171	D .9090				
11.9 S	.5173	D .9113			M 13.3	M 16.5
13.0 S	.5177	D .9146				
14.2 S	.5185	D .9199				
14.7					S 13.2	M 17.1
15.3 S	.5188	D .9247				
16.4 S	.5178					
17.6 S	.5174				S 13.2	M 17.8
18.1 S	.5175	D .9396				
18.7 S	.5158					
20.9 S	.5136	D .9554			S 13.2	M 18.6
21.5 S	.5127					
23.2					S 13.2	M 19.4
23.8 S	.5068	D .9725				
24.3 S	.5057					
26.0					S 13.2	M 20.4
26.6 S	.4977	D .9943				
27.2 S	.4965					
28.9					S 13.2	M 21.7
29.4 S	.4850	D 1.02				
30.0 S	.4836					
31.7					S 13.3	M 22.9
32.3 S	.4721	D 1.06				
32.8 S	.4717					
34.5					S 13.4	W 24.5
35.1 S	.4607	D 1.09				
37.4					S 13.5	M 26.1
37.9 D	.4442	D 1.13				
40.2					M 13.7	
40.8 D	.4337	D 1.17				
43.0					W 13.9	
43.6 D	.4207	S 1.23				
45.9				W .489	W 14.1	
46.4 D	.4109	S 1.28				
48.7 D	.4008	S 1.35		W .469	M 14.4	
51.5			W .904	W .454	M 14.7	
52.1 D	.3923	M 1.43				

θ_{ab}	C7	C8	C9	C10
± 0.2	$\pm .0008$	$\pm .06$	$\pm .002$	± 0.1
54.3				M 15.2
54.9	D .3826	D 1.54		
57.2				M 15.5
57.7	D .3766	D 1.63		
60.0				M 16.1
60.6	D .3676	D 1.77		
62.8			W .803	M 16.6
63.4	D .3610	S 1.94		
64.0		M 1.96		M 16.8
65.1		M 2.05		W 17.3
66.2	D .3554	M 2.12		W 17.4
67.4		W 2.16		W 17.7
68.5		M 2.24	W .767	W 17.8
69.1	D .3512			
69.6		W 2.40		W 18.1
70.8		M 2.51		W 18.5
71.3			W .751	
71.9	D .3471	W 2.63		W 18.8
74.2		W 2.88	W .741	W 19.5
74.7	D .3437			
75.3		W 3.03		W 19.8
76.6				W 20.4
77.0			W .730	
77.6	D .3409			M 20.7
78.7				M 21.1
79.8		W 3.79	W .728	M 21.5
80.4	D .3398			
80.9		W 4.23		M 22.0
81.8		M 4.41		M 22.3
82.6			W .722	
83.2	D .3375	M 4.82		M 22.9
84.3		M 5.34		M 23.4
85.5		M 5.76	W .715	M 23.8
86.0	D .3361			
86.6		M 6.11		W 24.1
87.7		W 6.69		W 24.5
88.3			W .713	
88.9	D .3352	W 6.89		
90.0				W 24.5
73.0		W 2.72		

θ_{ab}	C12	C13	C14	C15	C16	C17
± 0.2	± 0.1	± 0.1	± 0.1	± 0.1	± 0.1	± 0.1
0.6	D 23.8					
4.0	D 23.9					
6.2	D 24.0					
9.1	D 24.2					
11.9	D 24.4					
14.7	D 24.7					
17.6	D 25.0					
20.9	D 25.5					
23.2	D 25.9					
26.0	D 26.5					
28.9	D 27.2					
31.7	D 28.0					
34.5	D 28.7					
37.4	D 29.7					
40.2	D 30.9					
43.0	D 32.1					
45.9	D 33.2					
48.7	D 34.7					
51.5	D 36.3					
54.3	D 38.6					
57.2	D 39.9					
60.0	D 42.3					
62.8	D 43.9		M 13.8			
64.0	D 44.5		M 14.0			
65.1	S 45.7		D 14.3			
66.2	S 46.0		D 14.4			
67.4	S 46.4		D 14.6			
68.5	S 46.8		D 14.7			
69.6	S 47.1		D 14.8			
70.8	M 47.1		D 15.1			
71.9	S 46.8		D 15.2			
73.0	S 46.5		D 15.4			
74.2	S 45.8		D 15.5			
75.3	M 45.0		D 15.7			
76.6	M 43.6		D 16.0			
77.6	S 42.5		D 16.2			
78.7	M 41.6		D 16.4			
79.8	S 40.2		D 16.6			
80.9	S 38.6		D 16.9		M 23.8	
81.8	S 37.9		D 17.1		M 23.7	
83.2	D 36.2		S 17.5	W 22.6	M 23.4	M 41.3
84.3	D 34.9		S 17.8	W 22.1	S 23.2	M 39.9
85.5	D 33.7		M 18.1	W 21.3	S 23.1	M 38.8
86.6	S 32.9		M 18.4	W 20.7	D 23.0	M 38.1
87.7	M 31.7		M 18.9	M 20.0	D 22.9	M 37.3
88.9	M 31.1	W 11.4	M 19.2	M 19.6	D 22.9	W 37.1
90.0	S 30.9		M 19.4	M 19.4	D 22.9	W 37.1

θ_{ab}	C18	C19	C20	C21
± 0.2	± 0.1	± 0.1	± 0.1	± 0.1
51.1				W 48.5
54.3				W 51.9
57.2				W 54.0
77.6		M 49.5		
78.7		M 49.3		
79.8	W 50.0	M 49.1		
80.9	M 47.8	M 48.8		
81.8	M 46.8	M 48.7		
83.2	S 44.9	M 48.5		
84.3	S 43.5	M 48.4		
85.5	S 42.5	M 48.4	W 57.4	
86.6	S 41.9	M 48.3	M 57.6	
87.7	M 41.2	M 48.2	M 57.7	
88.9	W 41.1	M 48.1	M 57.8	
90.0		M 48.1	M 57.7	

BIBLIOGRAPHY

- Alekseevskii, N. E. & Gaidukov, Yu. P., 1959, J. Exptl. Theor. Phys. (U.S.S.R.) 36, 447-450
 Engl. Trans.: Soviet Physics - JETP 9, 311 (1959)
- Alekseevskii, N. E. & Gaidukov, Yu. P., 1959, J. Exptl. Theor. Phys. (U.S.S.R.) 37, 672-677
 Engl. Trans.: Soviet Physics - JETP 10, 481 (1960)
- Alquié, C. & Lewiner, J., 1972, Phys. Rev. B6, 4490-4501
- Aurbach, R. L.; Ketterson, J.B.; Mueller, F. M.; Windmiller, L. R., 1970, Argonne National Laboratory Report #ANL-7659, 5-7
- Barrett, C. S., 1961, Advances in X-ray Analysis 5, 33-47
- Bezugli, P. A.; Galkin, A. A.; Zhevago, S. E., 1964, J. Exptl. Theor. Phys. (U.S.S.R.) 47, 825-835
 Engl. Trans.: Soviet Physics - JETP 20, 552 (1965)
- Bradley, A.J., 1935, Z. Krist 91, 302-316
- Chambers, R. G., 1966a, Proc. Phys. Soc. 88, 701-715
- Chambers, R. G., 1966b, Proc. Phys. Soc. 89, 695-710
- Condon, J. H., 1964, Bull. Am. Phys. Soc. 9, 239
- Cook, J. R. & Datars, W. R., 1970a, Phys. Rev. B1 1415-1424
- Cook, J. R. & Datars, W. R., 1970b, Can. J. Physics 48, 3021-3028
- Dingle, R. B., 1952, Proc. Roy. Soc. A211, 500-516, 517-525
- Fukumoto, A. & Strandberg, M. W. P., 1967, Phys. Rev. 155,

685-693

Gabel, D. E. & Cochran, J. F., 1972, Can. J. Phys. 50,

863-869

Gold, A. V., 1968, Solid State Physics, the Simon Fraser Univ. Lectures, Vol. 1, Electrons in Metals, ed: Cochran,

J. F. & Haering, R. R. : Gordon & Breach, 39-126

Goldstein, A. & Foner, S., 1966, Phys. Rev. 146, 442-454

Goy, P.; Goldstein, A.; Langenberg, D. N.; Picard, J. C., 1967,

Phys. Lett. 25A, 324

Griessen, R.; Krugmann, H.; & Ott, H. R., 1974, Phys. Rev.

B10, 1160-1172

Gurevich, V. L.; Skobov, V. G.; Firsov, Yu. A., 1961, J. Exptl.

Theor. Phys. (U.S.S.R.) 40, 786-791

Engl. Trans.: Soviet Physics - JETP 13, 552 (1961)

Haberland, P. H.; Cochran, J. F.; & Shiffman, C. A., 1969,

Phys. Rev. 184, 655-663

Harrison, W. A., 1960, Phys. Rev. 118, 1190

Ketterson, J. B. & Windmiller, L. R., 1970, Phys. Rev.

B1, 463-470

Kimball, J. C. & Stark, T. W., 1971, Phys. Rev. B4, 1786-1794

Koster, G. F., 1962, Phys. Rev. 127, 2044

Lewiner, J., 1967, Phys. Rev. Lett. 19, 1037

Lifshitz, I. M. & Kosevich, A. M., 1955, J. Exptl. Theor.

Phys. (U.S.S.R.) 29, 730

Engl. Trans.: Soviet Physics - JETP 2, 636 (1956)

- Moore, T. W., 1966, Phys. Rev. Lett. 16, 581
- Moore, T. W., 1967, Phys. Rev. Lett. 18, 310
- Moore, T. W., 1968, Phys. Rev. 165, 864-869
- Mueller, F. M., 1966, Phys. Rev. 148, 636-637
- Munarin, J. A.; Marcus, J. A.; & Bloomfield, P. E., 1968,
Phys. Rev. 172, 718-736
- Munarin, J., 1968, Phys. Rev. 172, 737-746
- Reed, W. A. & Marcus, J. A., 1962, Phys. Rev. 126, 1298-1307
- Reed, W. A. & Marcus, J. A., 1963, Phys. Rev. 130, 957
- Reed, W. A., 1969, Phys. Rev. 188, 1184-1192
- Reed, W. A., private communication
- Roberts, B. W., 1961, Phys. Rev. Lett. 6, 453
- Shapira, Y., 1964, Bull. Am. Phys. Soc. 9, 239
- Shapira, Y. & Lax, B., 1965, Phys. Rev. 138, A1191
- Shoenberg, D., 1949, Nature 164, 225-226
- Shoenberg, D., 1952, Phil. Trans. Roy. Soc. London A245, 1
- Shoenberg, D., 1957, Prog. Low. Temp. Phys. 2, 226-265
- Slater, J. C.; Koster, G. F.; Wood, J. H., 1962, Phys. Rev.
126, 1307-1317
- Wood, J. H., 1966, Phys. Rev. 146, 432-441
- Yaqub, M. & Cochran, J. F., 1965, Phys. Rev. 137, A1182-
A1200